

86P

550765

NASA TN D-1352

NASA TN D-1352



TECHNICAL NOTE

D-1352

EFFECT OF JET PLUMING ON THE STATIC STABILITY OF
CONE-CYLINDER-FLARE CONFIGURATIONS

AT A MACH NUMBER OF 9.65

By William F. Hinson and Ralph A. Falanga

Langley Research Center
Langley Station, Hampton, Va.

**CASE FILE
COPY**

NATIONAL AERONAUTICS AND SPACE ADMINISTRATION
WASHINGTON

September 1962

NATIONAL AERONAUTICS AND SPACE ADMINISTRATION

TECHNICAL NOTE D-1352

EFFECT OF JET PLUMING ON THE STATIC STABILITY OF
CONE-CYLINDER-FLARE CONFIGURATIONS

AT A MACH NUMBER OF 9.65

By William F. Hinson and Ralph A. Falanga

SUMMARY

The effects of jet pluming on normal force and pitching moment of 14 cone-cylinder-flare configurations have been measured at a free-stream Mach number of 9.65 with Reynolds numbers based on model length of 500,000 to 600,000. Geometric variables included nose bluntness, flare half-angle, and nozzle geometry and exit displacement. Two test nozzles with design Mach numbers of 3.74 and 4.60 were operated with compressed air to simulate the initial jet-boundary shape of a particular solid-propellant rocket motor operating between altitudes of 165,000 and 215,000 feet. The ratio of the jet pressure to free-stream static pressure varied from a jet-off condition to approximately 1,300 for the nozzle with design Mach number of 3.74, and from a jet-off condition to approximately 280 for the nozzle with design Mach number of 4.60. The angle-of-attack range was from 0° to approximately 6° .

The results indicate that as the jet-pressure ratio was increased the size of the jet plume increased, and as a result the model static stability was decreased. Increasing the angle of attack resulted in a reduction in static instability during the jet-on condition. Increasing nose bluntness resulted in a more forward movement of the center of pressure when jet-plume interference was not present and a rearward movement in the center of pressure when jet interference was present. Increasing the nozzle-area expansion ratio and displacing the nozzle exit downstream of the flare base resulted in a more rearward location of the center of pressure.

INTRODUCTION

When the ratio of jet exit pressure to ambient static pressure of a rocket-powered vehicle becomes sufficiently large, the exhausting jet will expand to form a large plume at the vehicle base. The presence of these gaseous plumes, which are very likely to exist on rocket vehicles

operating at high altitudes, can, through the interference with the external stream, cause extensive boundary-layer separation on the vehicle surfaces forward of the nozzle exit. This condition was first demonstrated experimentally in references 1 and 2 and was later confirmed by the observations in reference 3. The effects of the presence and extent of flow separation on vehicle stability are important since aerodynamic stabilizing surfaces such as fins or flares are commonly located in the regions of possible flow separation. When these regions of flow separation, characterized by reduced dynamic pressure, completely or even partly envelop the stabilizing surfaces of the vehicle, the vehicle stability may be seriously affected.

Investigations of this phenomenon, however, are scarce, and although many investigations of jet-exhaust effects are available in the literature, most of these have been limited to low ratios of jet exit pressure to ambient static pressure, and only small to negligible jet effects on stability were noted. (See, for example, ref. 4.) The investigation reported in reference 1 treated jet-exhaust effects at ratios of jet exit pressure to ambient static pressure that would be encountered by a rocket-powered research aircraft by simulating the jet at zero degrees angle of attack with a solid plume. The results indicated a loss in stability; however, this technique was limited to low angles of attack, since the solid plumes did not account for the effects of angle of attack on the actual jet-boundary shape.

Thus, because of the need for more information, the present investigation was undertaken to study the jet-exhaust effects on static stability of cone-cylinder-flare bodies. Furthermore, because of the uncertainties associated with the solid-plume technique, it was decided to provide a two-component balance-nozzle combination that would allow angle-of-attack effects to be determined in the presence of a gaseous jet boundary. Also investigated were the effects of nose bluntness and the combined effect of nozzle geometry and nozzle location on the static stability of these missile-type bodies. The two-component balance measured normal force and pitching moment of each configuration. Two jet nozzles were used with compressed air; the nozzles were designed to simulate the initial shape of the jet boundary of a particular solid-propellant rocket motor operating at altitudes between 165,000 and 215,000 feet.

The tests were performed in the Langley 11-inch hypersonic tunnel at a Mach number of 9.65; the free-stream Reynolds number based on model length varied from approximately 500,000 to 600,000. The ratio of the jet pressure to free-stream static pressure ranged from a jet-off condition to about 1,300. The model angle of attack was varied from approximately 0° to 6° .

SYMBOLS

A	cross-sectional area of cylinder, sq in.
d	diameter of cylinder, in.
C_N	normal-force coefficient, $\frac{F_N}{q_\infty A}$
C_m	pitching-moment coefficient, $\frac{M_y}{q_\infty A d}$
F_N	normal force along Z-axis, positive direction upward, lb
M_y	moment about Y-axis, in-lb
M_∞	free-stream Mach number
p_j/p_∞	jet-pressure ratio (ratio of jet exit to free-stream static pressure)
q_∞	free-stream dynamic pressure, lb/sq in.
r	radius of nose, in.
R	radius of cylinder, in.
x_{cp}	center of pressure measured from nose tip, positive rearward (except in fig. 26), in.
α	angle of attack, deg
α_m	mean values of angle of attack used in schlieren photographs, deg

APPARATUS

Models

A total of 14 cone-cylinder-flare models, constructed of Inconel, were used in this study; a photograph of each model, accompanied by its designation can be seen in figure 1. A drawing with detailed dimensions of the model components, including the identification of the parts by letters and numerical subscripts is shown in figure 2. Model noses C1

and C_2 were 9° half-angle cones with bluntness ratios r/R of 0.094 and 0.569, respectively. The flared skirts F_7 , F_{13} , and F_{16} were conical frustums with half-angles of 7° , 13° , and 16° , respectively. The flared skirt F_{13-31} was a biconic afterbody that consisted of a frustum of 13° half-angle followed by one of 31° half-angles. All flared skirts were 1.32 body diameters long. The cylindrical center body and flared afterbody sections were shells, 0.030 inch thick. Model jet nozzles N_1 and N_2 were conical, convergent-divergent supersonic nozzles. Detailed dimensions of these nozzles are shown in figure 3. When nozzle N_2 was used, the exit was displaced 0.95 inch (or 1.35 body diameters) beyond the flare base of the model. A two-component strain-gage balance, the nozzles with their settling chambers, and a portion of the center support sting were located in the models. Photographs of the strain-gage balance rigidly fixed to the center support sting and with nozzles N_1 and N_2 assembled to the support sting are shown in figure 4. The center support sting, a hollowed steel tube, allowed the compressed air from the supply tank to be emptied into the settling chamber of the jet nozzles. The louvers through which the compressed air entered the settling chamber can be seen in figure 4(a). Shown in figure 5 is an exploded view of the relationship of the unassembled model parts and the order of assembly. Figure 6 shows a cutaway view of model $C_1BF_{13}N_1$ assembled to the balance and support sting and also shows the installation in the Langley 11-inch hypersonic tunnel. The installation of the 13 remaining models was similar.

L
2
0
3
9

Jet Simulation

Nozzles N_1 and N_2 were designed to have exit Mach numbers of 3.74 and 4.60, respectively, and to use compressed air to simulate the jet initial inclination angle of a particular rocket operating over an altitude range from approximately 165,000 feet to 215,000 feet. Details of the design technique and simulation are described in reference 3. Allowance was made in the design of the test nozzles N_1 and N_2 for the presence of the center support sting.

Instrumentation

A two-component electrical strain-gage balance of high sensitivity, designed and built specifically for these models, measured the aerodynamic normal force and pitching moment. The settling-chamber pressure was measured with a Bourdon pressure gage, which was visually monitored during the tests. Three calibrated gages were used, each with a different range. However, one gage was selected (depending upon the magnitude of pressure

required) to measure the chamber pressure during a given run. The pressure gages were connected to the model by a steel tube with an inside diameter of 0.040 inch. The tube terminated in the surface of the center support sting at approximately the maximum diameter of the plenum chamber.

Wind Tunnel

The investigation was conducted in the Mach number 9.65 test section of the Langley 11-inch hypersonic tunnel. Details of this facility are discussed in references 5, 6, and 7.

METHOD OF ANALYSIS

The normal-force and pitching-moment measurements are referred to the body-axis system. (See fig. 7.) Locations of center of pressure x_{cp} have been obtained from a ratio of the pitching-moment and normal-force measurements, and these locations have been measured from the model nose-cone tip, except as noted. For example, the equation used

$$\text{is } x_{cp} - x_{\text{moment reference}} = - \frac{M_Y}{F_N}.$$

The moment center, located 1.247 inches behind nose-cylinder juncture on all models (fig. 2), was chosen as a reference about which to discuss the static stability status of the models; any comments on stability made herein are relative only to this reference location. Due to nose and flare modifications the moment-center location varied from 58 to 65 percent of the model length. However, this reference location is not unrealistic for rocket-powered missile vehicles since, for a majority of vehicles, the center-of-gravity location might be anywhere from 45 to 65 percent of the body length.

The models were considered to be statically stable if the center-of-pressure location was rearward of the moment reference location. If, however, the center-of-pressure location coincided with the moment reference or was forward of this reference, then, with respect to these conditions, the models were considered to be neutrally stable or statically unstable.

Figure 8 is a sketch of the flow field about model $C_{1BF16N1}$, and the nomenclature of the flow-field characteristics is indicated on the sketch. The nomenclature used is typical for all models.

TESTS

Table I summarizes test conditions for each model of this investigation. The models were tested at a Mach number of 9.65; free-stream Reynolds number based on model length varied from approximately 500,000 to 600,000. When the models contained nozzle N_1 , the jet-pressure ratio p_j/p_∞ ranged from a jet-off condition to about 1,300; for nozzle N_2 the range was from a jet-off condition to about 280. The angle of attack ranged from 0° to approximately 6° . Schlieren photographs of the flow patterns were made for each configuration.

ACCURACY OF DATA

All jet-pressure ratios p_j/p_∞ quoted herein are estimated to be accurate within ± 3 percent. Mach number variation in the region of the test model was within ± 0.02 . Angle-of-attack values presented with the aerodynamic coefficient curves are estimated to be accurate within $\pm 0.25^\circ$. Maximum error in the aerodynamic coefficients, based on inherent balance error, and data reduction are estimated to be ± 0.01 for C_N and C_m .

For some conditions, the x_{cp} location was at or forward of the nose tip. This occurred, usually, at low angles of attack and during the jet-on condition when a large portion of the flow about the model was separated. In most of these cases, the magnitude of the normal force used to compute x_{cp} was less than the quoted accuracy of the balance. Therefore these data points should be interpreted only as a qualitative measure of model instability.

RESULTS AND DISCUSSION

Variations of normal-force coefficient, pitching-moment coefficient, and center-of-pressure location for all models are plotted against angle of attack for various jet-pressure ratios and are shown in figures 9 to 22.

Also included with the measured data of each model are selected schlieren photographs of the flow field at various jet-pressure ratios and angles of attack. As is shown in table I for a given model the angles of attack were not exactly duplicated for different values of jet-pressure ratios. Therefore, the angle of attack listed for each

group of schlieren photographs in figures 9 through 22 is a mean value; each schlieren photograph is within $\pm 0.5^\circ$ of this mean value.

Effect of Jet-Pressure Ratio and Angle of Attack

Jet-off condition.- A review of the results in figures 9 to 22 indicates that during the jet-off condition, ten of the models were statically stable, one model ($C_2BF_{13}N_1$, fig. 14) was marginal, and three models ($C_1BF_7N_1$, $C_2BF_7N_1$, and $C_2BF_{13}N_2$) were statically unstable. (See figs. 9, 13, and 20.) The instability or marginal stability of the models was a result of an insufficient amount of stabilizing surface, a loss of dynamic pressure in the flare region due to increasing nose bluntness, or a combination of both. Increasing the angle of attack caused small to negligible changes in the stability level of these models or of the statically stable models.

An examination of the flow pictures for the range of angles of attack obtained (with the exclusion of $\alpha = 0^\circ$) showed that the flow was attached to most of the windward side of all models. For some models isolated regions of separated flow were present, but the flow was reattached to the model surface upstream of the flare base.

Jet-on condition.- As the jet-pressure ratio p_j/p_∞ was increased, the size of the jet plume and the extent of the separated flow at $\alpha = 0^\circ$ increased. Somewhere between p_j/p_∞ values of 100 and 500 the separation point moved forward to the cone-cylinder juncture, and the stabilizing flares were completely immersed in separated flow. Further increases in p_j/p_∞ did not move the separation point farther forward nor was the cone of separated flow increased appreciably.

At angles of attack slightly above zero, the submersion of the flare in separated flow caused the stability of the models to decrease with increasing p_j/p_∞ . Somewhere between p_j/p_∞ values of 100 and 500, all models displayed unstable characteristics. Further increases in p_j/p_∞ , however, had little effect on changing the stability level. This result is interpreted to indicate that at the extreme values of p_j/p_∞ where the flares are completely submerged in separated flow, the resulting pitching moments are provided mainly by the nose-cone contribution.

At higher angles of attack, the jet plume becomes distorted in such manner that the plume is compressed on the windward side and expanded on the leeward side. Because of this phenomenon, as the angle of attack is increased, the windward side of the flare approaches the separated flow

boundary, and eventually penetrates the boundary, so that flow reattachment occurs. As the stabilizing flare approaches the separated boundary, a decrease in instability results. Although the tests were not extended to angles of attack high enough to show the x_{cp} at the moment reference location, this fact can be inferred from some of the data. However, the flared models with the lowest half-angles ($C_1BF_7N_1$ and $C_2BF_7N_1$) indicated an opposite trend in stability level as p_j/p_∞ was increased above 100. That is, as p_j/p_∞ was increased above 100, there was a small reduction of instability; however, at present the cause of this trend can not be explained.

Effect of Flare Geometries

Figure 23 shows a comparison at $\alpha = 3^\circ$ of the variation of x_{cp} with p_j/p_∞ for configurations with constant nose shape and nozzle. For most values of p_j/p_∞ the effect of increasing flare angle was to move the x_{cp} rearward. This was opposite to the effect of increasing p_j/p_∞ which was to move the x_{cp} forward. The models with the biconic flared skirts had the most rearward x_{cp} location. However, at the high values of p_j/p_∞ , when the separated flow moved up to the nose-cylinder juncture, there existed a general tendency for the x_{cp} of the models being compared to approach the centroid of area of the nose cone. The rate at which the x_{cp} moves forward as p_j/p_∞ was increased above the value to cause the flow to separate over the flare can also be observed from these plots. As soon as the flow separates from the flared skirts, the models rapidly become unstable.

Effect of Nozzle Geometry and Exit Location

The effect of nozzle geometry on the x_{cp} location could not be isolated since nozzle geometry and location of the nozzle exit were changed simultaneously. Thus, the combined effect of these variables on the x_{cp} location is presented in figure 24. Since the nozzles were not attached to the model shell (fig. 6), any forces on the nozzle N_2 extension could not be transmitted to the balance. However, in the present tests any forces that existed on nozzle N_2 should have been small since the flow around this nozzle was separated (see flow photographs). All the data presented are for models duplicating the initial

L
2
0
3
9

angle of the jet boundary for a particular rocket motor with a fixed combustion-chamber pressure and operating at an altitude of 206,000 feet. Thus, in order to duplicate this condition according to reference 3, models using nozzle N_1 were required to operate at p_j/p_∞ of approximately 1,200 and those using nozzle N_2 at p_j/p_∞ of approximately 135. However, the test values of p_j/p_∞ obtained were not exactly at the required magnitude, but the ratios used are close enough to lend validity to this comparison. The models are compared according to the flare angles and nose bluntness. The 7° flare models were not included since these models were not tested with nozzle N_2 .

In all cases the x_{cp} location was farther rearward for models with nozzle N_2 than for those with nozzle N_1 , but not necessarily behind the moment reference. In fact, with the exception of models $C_1BF_{13-31}N_2$ and $C_2BF_{13-31}N_2$ all x_{cp} locations were forward of the moment reference. The x_{cp} difference between any given set of models being compared increased as the model flare angles were increased. However, as the bluntness was increased these differences were not so large. The maximum difference which was approximately 3.5 body diameters occurred with the biconic flared-skirt models with nose C_1 .

Effect of Free-Stream Mach Number

The variation of C_N , C_m , and x_{cp} for model $C_2BF_{13-31}N_1$ with p_j/p_∞ at $\alpha = 2.4^\circ$ is shown in figure 25 for free-stream Mach numbers of 9.65 and 17.3. The free-stream Reynolds number based on model length at $M_\infty = 17.3$ was approximately 450,000 as compared with approximately 500,000 for $M_\infty = 9.65$. The $M_\infty = 17.3$ data were obtained from Chance Vought Corporation (a division of Ling-Temco-Vought, Inc.). Model $C_2BF_{13-31}N_1$ was the only configuration common to the Chance Vought and NASA study. At $M_\infty = 17.3$ and $\alpha = 2.4^\circ$, the x_{cp} location remained rearward of the moment reference location throughout the p_j/p_∞ range. For the jet-off condition and values of p_j/p_∞ up to approximately 100 the model was more stable at $M_\infty = 9.65$ than at $M_\infty = 17.3$; however, for values of p_j/p_∞ above 100 the model was more stable at $M_\infty = 17.3$ than at $M_\infty = 9.65$. The large difference in x_{cp} location between $M_\infty = 9.65$ and $M_\infty = 17.3$ for values of p_j/p_∞ above 100 appeared to be a direct result of the more compressed jet plume on the windward side for the higher Mach number case. It is shown in reference 1 that

increasing the free-stream Mach number reduces the interference of jet plume on the flow over cone-cylinder-flared bodies; hence, the extent of flow separation was decreased.

Effect of Nose Bluntness

The effect of nose bluntness on the x_{cp} location for various values of angle of attack and pressure ratios is shown in figure 26. Data presented are for the biconic flare arrangement with nozzle N_1 . These results are typical of those obtained for the other model combinations. As the nose bluntness was increased from 0.094 to 0.569, a forward movement of x_{cp} of $3/4$ of a body diameter was realized at pressure ratios at a jet-off condition and 100. From a study of the schlieren photographs at the previously mentioned pressure ratios, there was no evidence that flow separation caused these x_{cp} differences between the models; see figures 13 to 16. This forward movement of x_{cp} was apparently due to the increase of entropy caused by the bow shock of the more blunt nose. As a result, the local dynamic pressure in the flare region was reduced from the free-stream value. An increase in the reduction of local dynamic pressure with increasing nose bluntness has been shown by several investigators (see, for example, ref. 8).

At $p_j/p_\infty = 975$, a rearward movement of x_{cp} of approximately $1/2$ of a body diameter was realized when the nose bluntness was increased from 0.094 to 0.569. Since for both nose geometries extensive flow separation did occur as a result of jet pluming, the rearward movement of x_{cp} was interpreted to mean that the more blunt nose C_2 provided smaller pitching moments either due to a reduction in local dynamic pressure (entropy loss) on the forebody and/or reduced lift due to the lower fineness ratio nose cone.

CONCLUDING REMARKS

The effect of jet pluming on the normal force and pitching moment of 14 cone-cylinder-flare configurations has been measured at a free-stream Mach number of 9.65 and Reynolds numbers based on model length of 500,000 to 600,000. The range of jet-pressure ratios varied from a jet-off condition to approximately 1,300 for the nozzle with an exit Mach number of 3.74 and from a jet-off condition to approximately 280 for the nozzle with an exit Mach number of 4.60. The angle-of-attack range was from 0° to approximately 6° . The results indicated the following trends:

L
2
0
3
9

1. Increasing the jet-pressure ratio caused the jet plume to grow larger and decreased the static stability.

2. Increasing the angle of attack reduced instability exhibited by the models at all pressure ratios.

3. For a jet-off condition and small values of jet-pressure ratio, increasing the nose bluntness moved the center of pressure forward. For larger values of jet-pressure ratio, increasing the nose bluntness moved the center of pressure rearward.

4. Displacing the exit plane of a supersonic nozzle downstream of the flare base and increasing the area expansion ratio of the nozzle resulted in increased stability.

5. On the basis of a single test at an angle of attack of 2.4° increasing the free-stream Mach number from 9.65 to 17.3 resulted in a more compressed jet plume on the windward side and a more rearward location of center of pressure.

Langley Research Center,
National Aeronautics and Space Administration,
Langley Station, Hampton, Va., March 19, 1962.

REFERENCES

1. Fetterman, David E., Jr.: Effects of Simulated Rocket-Jet Exhaust on Stability and Control of a Research-Type Airplane Configuration at a Mach Number of 6.86. NASA TM X-127, 1959.
2. Salmi, Reino J.: Effects of Jet Billowing on Stability of Missile-Type Bodies at Mach 3.85. NASA TN D-284, 1960.
3. Falanga, Ralph A., Hinson, William F., and Crawford, Davis H.: Exploratory Tests of the Effects of Jet Plumes on the Flow Over Cone-Cylinder-Flare Bodies. NASA TN D-1000, 1962.
4. Love, Eugene S.: Aerodynamic Investigation of a Parabolic Body of Revolution at Mach Number of 1.92 and Some Effects of an Annular Supersonic Jet Exhausting From the Base. NACA TN 3709, 1956. (Supersedes NACA RM L9K09.)
5. McLellan, Charles H., Williams, Thomas W., and Bertram, Mitchel H.: Investigation of a Two-Step Nozzle in the Langley 11-Inch Hypersonic Tunnel. NACA TN 2171, 1950.
6. McLellan, Charles H., Williams, Thomas W., and Beckwith, Ivan E.: Investigation of the Flow Through a Single-Stage Two-Dimensional Nozzle in the Langley 11-Inch Hypersonic Tunnel. NACA TN 2223, 1950.
7. Bertram, Mitchel H.: Boundary-Layer Displacement Effects in Air at Mach Numbers of 6.8 and 9.6. NASA TR R-22, 1959. (Supersedes NACA TN 4133.)
8. Seiff, Alvin: Secondary Flow Fields Embedded in Hypersonic Shock Layers. NASA TN D-1304, 1962.

L
2
0
3
9

TABLE I.- PRESENTATION OF TEST CONDITIONS

Figure	P_j/P_∞	α , deg				
Model $C_1BF_7N_1$						
9	Jet off	0	2.78	4.83		
	100	0	1.03	2.57	4.70	
	510	0	1.30	3.00	5.34	
	940	0	3.10	5.79		
	1175	0	1.44	3.03	5.94	
Model $C_1BF_{13}N_1$						
10	Jet off	0	1.72	3.14		
	100	0	1.92	3.86		
	490	0	2.80	5.05		
	950	0	2.67	2.96	5.00	5.35
	1260	0	1.26	2.87	5.19	
Model $C_1BF_{16}N_1$						
11	Jet off	0	1.40	2.70		
	100	0	1.43	2.77		
	490	0	2.56	4.76		
	940	0	2.42	4.54		
	1195	0	1.32	2.82	4.63	
Model $C_1BF_{13-31}N_1$						
12	Jet off	0	0.78			
	100	0	.55			
	510	0	1.68	3.86		
	975	0	2.87	4.43		
	1255	0	1.53	3.28	4.04	
Model $C_2BF_7N_1$						
13	Jet Off	0	1.25	2.50	4.95	
	100	0	1.52	2.87	4.78	
	510	0	1.60	2.60	5.05	
	975	0	1.30	2.30	4.72	
	1175	0	1.32	2.40	4.50	
Model $C_2BF_{13}N_1$						
14	Jet off	0	1.80	3.94		
	100	0	2.15	4.05		
	490	0	2.36	4.50		
	950	0	2.20	4.65		
	1290	0	1.35	2.55	4.62	
Model $C_2BF_{16}N_1$						
15	Jet off	0	1.95	3.70		
	100	0	1.90	4.25		
	510	0	2.53	4.25		
	975	0	2.40	4.43		
	1190	0	1.08	2.96	4.50	

TABLE I.- PRESENTATION OF TEST CONDITIONS - Concluded

Figure	P_j/P_∞	α , deg				
Model $C_2BF_{13-31}N_1$						
16	Jet off	0	1.15	2.85		
	100	0	1.36	3.00		
	560	0	1.80	3.48		
	975	0	1.60	3.70		
	1312	0	1.70	2.42	4.67	
Model $C_1BF_{13}N_2$						
17	Jet off	0	0.55	1.20	3.11	
	27	0	1.70	4.15		
	133	0	1.04	2.46	4.65	
	280	0	.91	2.51	5.24	
Model $C_1BF_{16}N_2$						
18	Jet off	0	0.45	1.29	2.67	
	27	0	.60	1.20	2.45	
	131	0	1.35	2.35	3.75	
	262	0	1.19	2.42	4.68	
Model $C_1BF_{13-31}N_2$						
19	Jet off	0	0.44	0.94		
	27	0	.50	1.12	1.73	
	131	0	.75	1.21	3.33	
	269	0	2.21	4.80		
Model $C_2BF_{13}N_2$						
20	Jet off	0	0.90	1.75	4.12	
	27	0	.94	2.05	4.40	
	136	0	.82	2.06	4.65	
	245	0	.82	2.23		
Model $C_2BF_{16}N_2$						
21	Jet off	0	0.83	1.72	3.42	
	27	0	1.15	2.00	3.75	
	135	0	.72	2.10	4.00	
	266	0	.70	2.03	4.46	
Model $C_2BF_{13-31}N_2$						
22	Jet off	0	0.72	1.35	2.80	
	27	0	.80	1.05	1.63	2.75
	131	0	1.03	2.38	3.83	
	269	0	2.37	4.37		

L
2
0
3
9

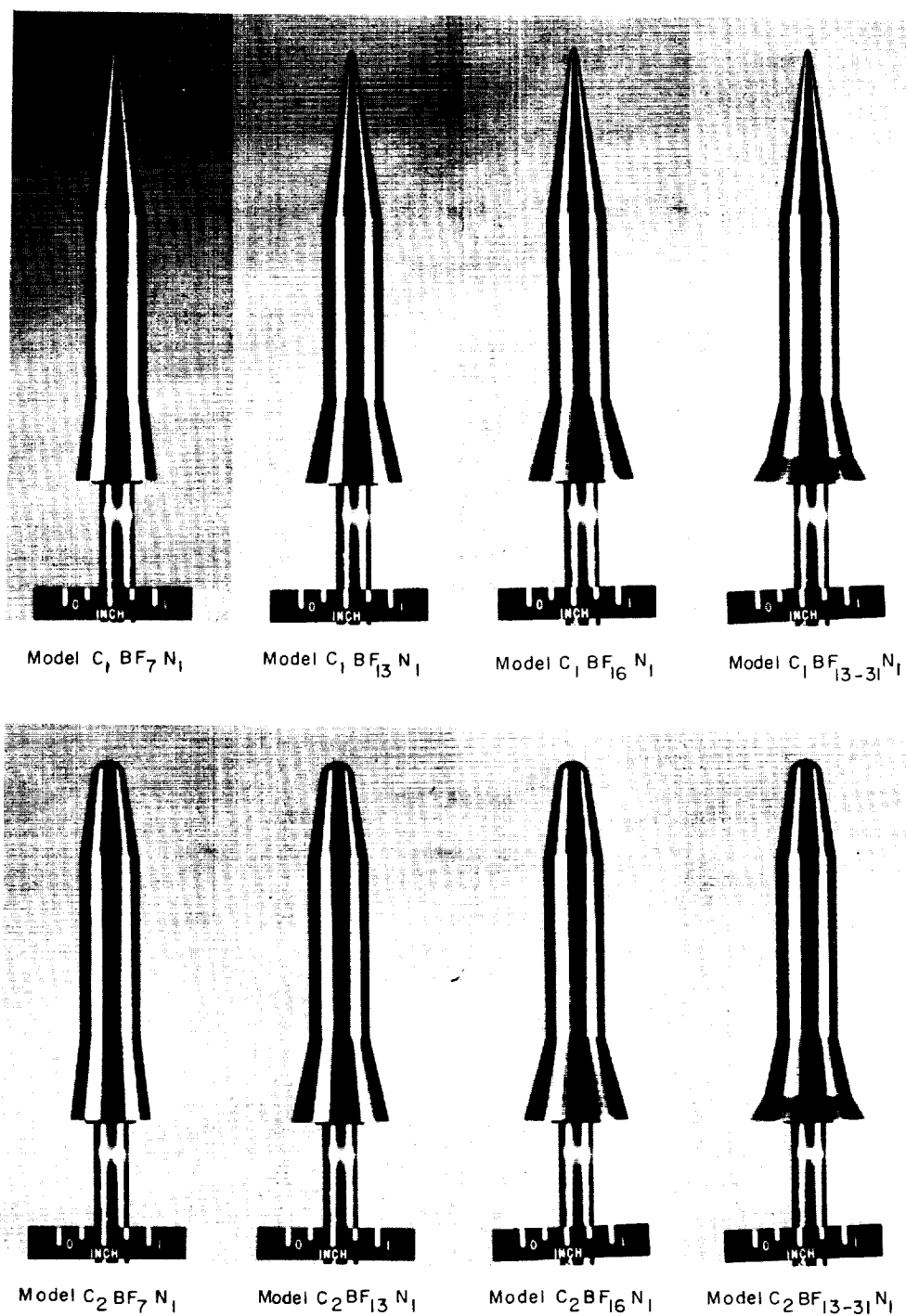


Figure 1.- Photographs of models tested.

L-62-57

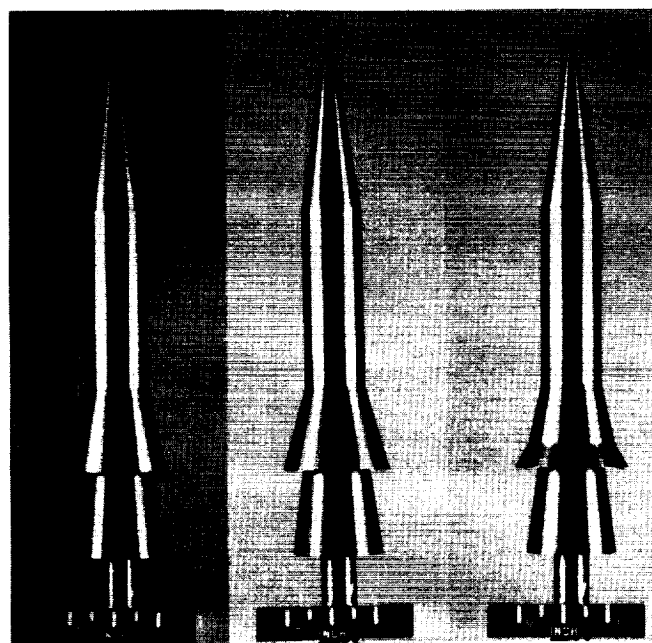
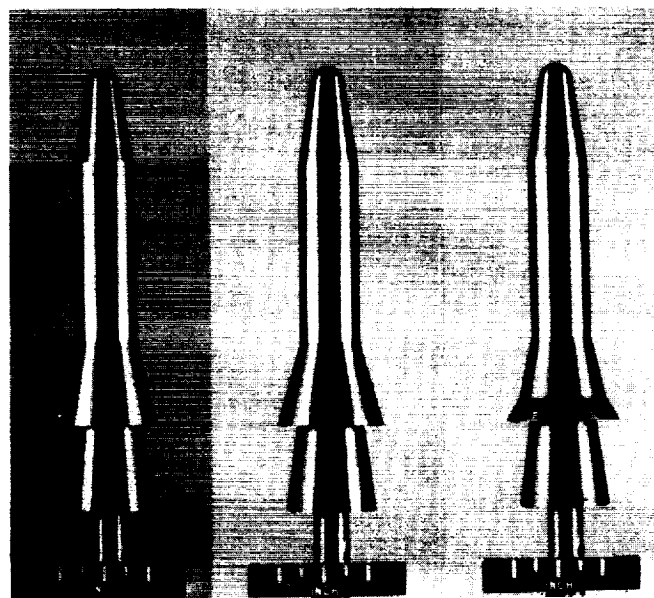
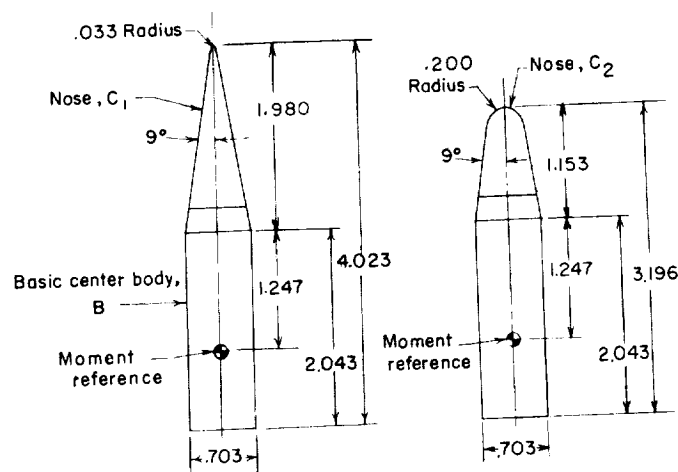
Model C₁ BF₁₃ N₂Model C₁ BF₁₆ N₂Model C₁ BF₁₃₋₃₁ N₂Model C₂ BF₁₃ N₂Model C₂ BF₁₆ N₂Model C₂ BF₁₃₋₃₁ N₂

Figure 1.- Concluded. L-62-58



(a) Model nose cones and basic center body.

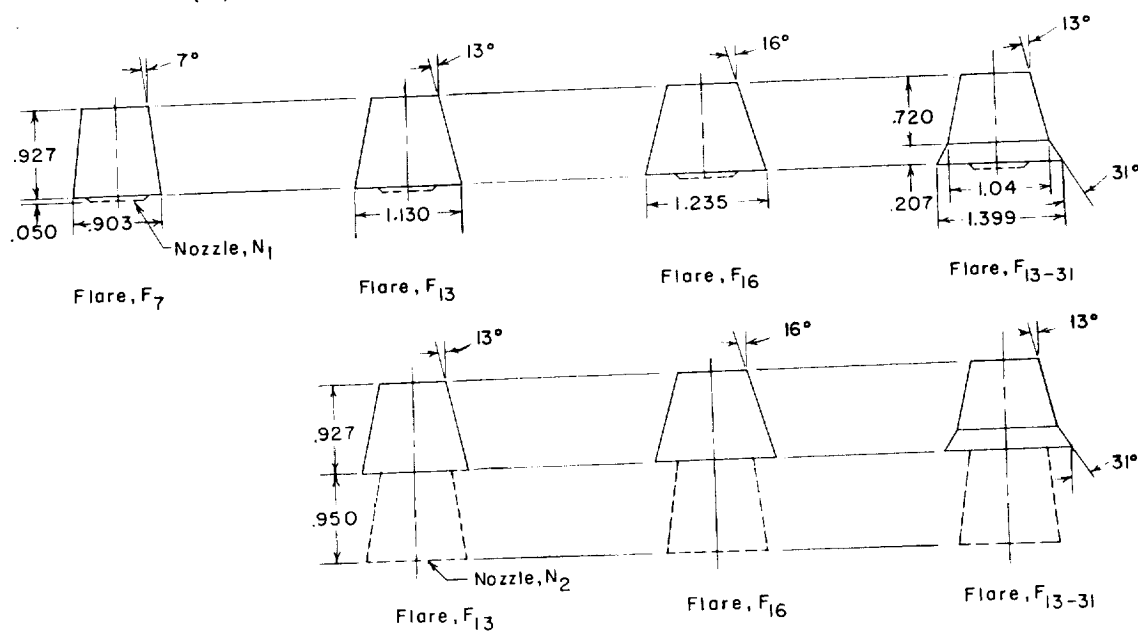
(b) Model flares with nozzle N_1 and N_2 outlined.

Figure 2.- Detailed component dimensions and designation of models tested. All dimensions are in inches.

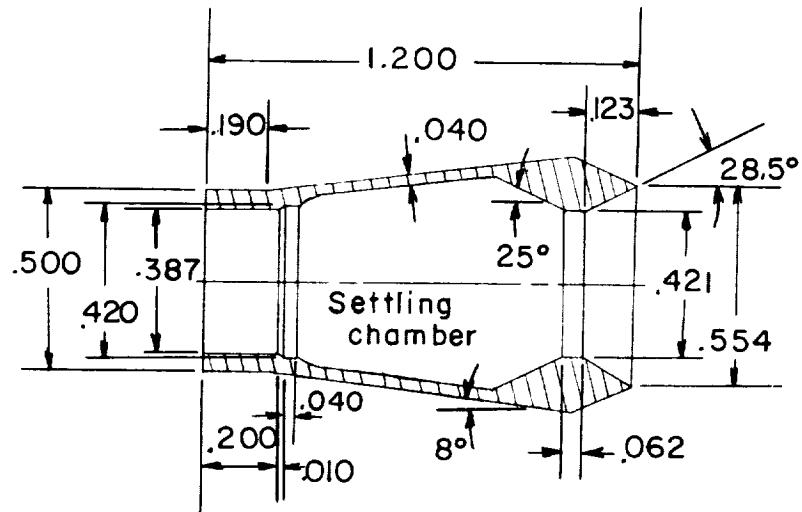
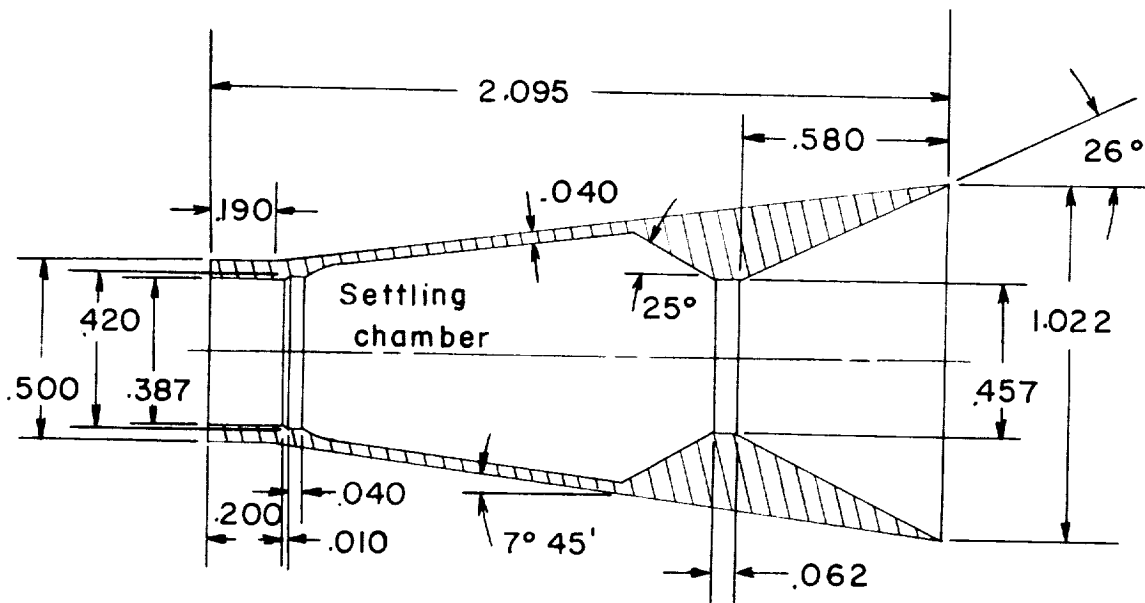
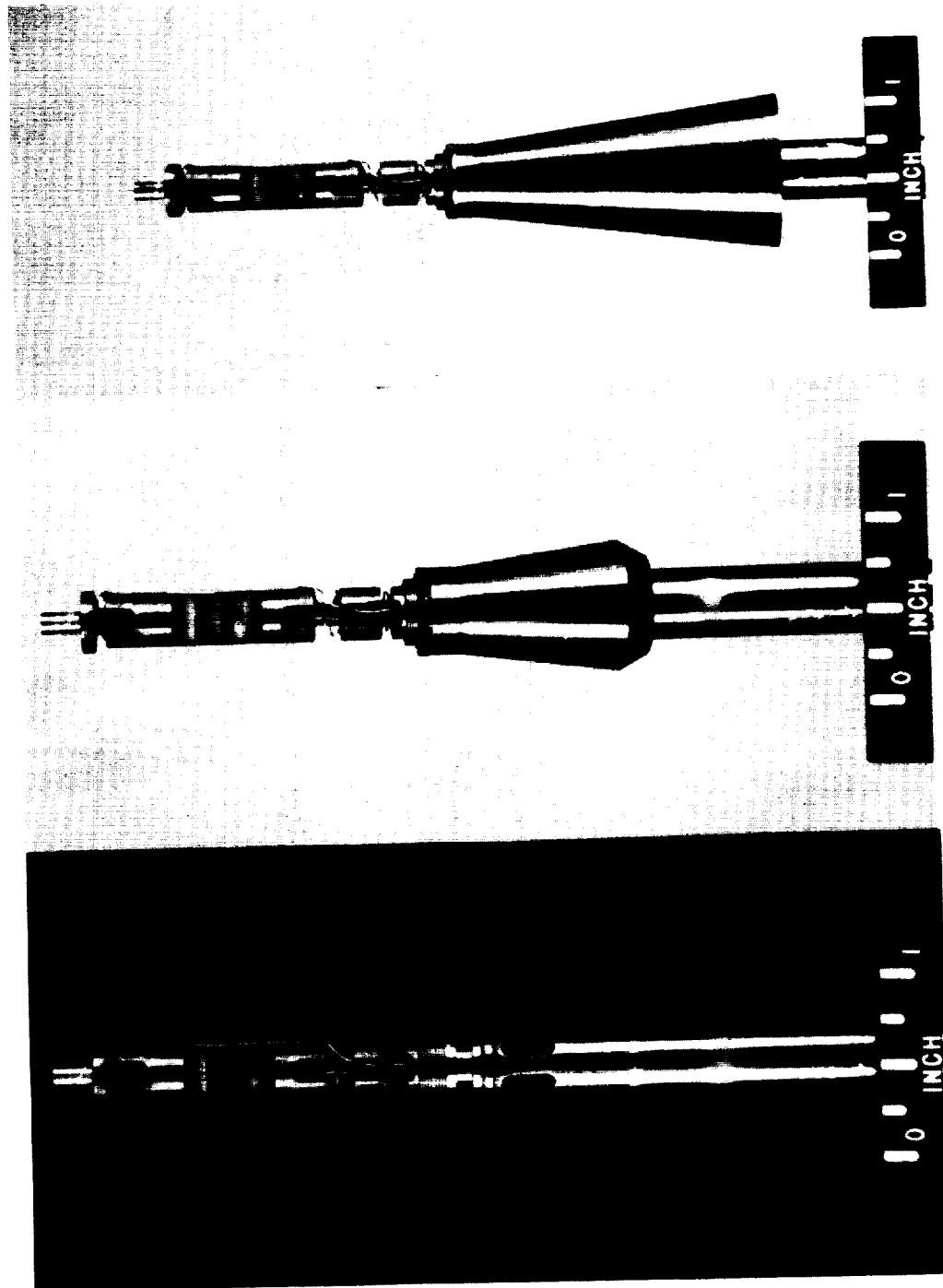
(a) Nozzle N₁.(b) Nozzle N₂.

Figure 3.- Details of nozzles tested. All dimensions are in inches.



(a) Sting and balance.

(b) Sting, balance, and
simulating nozzle N_1 .

(c) Sting, balance, and
simulating nozzle N_2 .

Figure 4.- Photographs of sting, strain-gage balance, and simulating nozzles. I-62-59

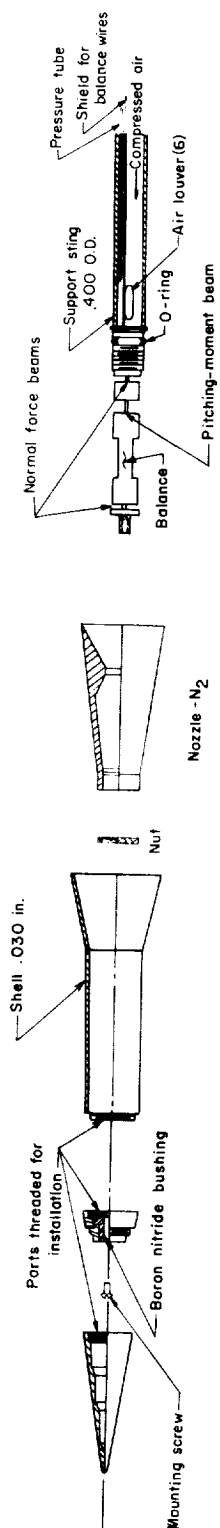


Figure 5.- Typical exploded view of models tested.

L-2039

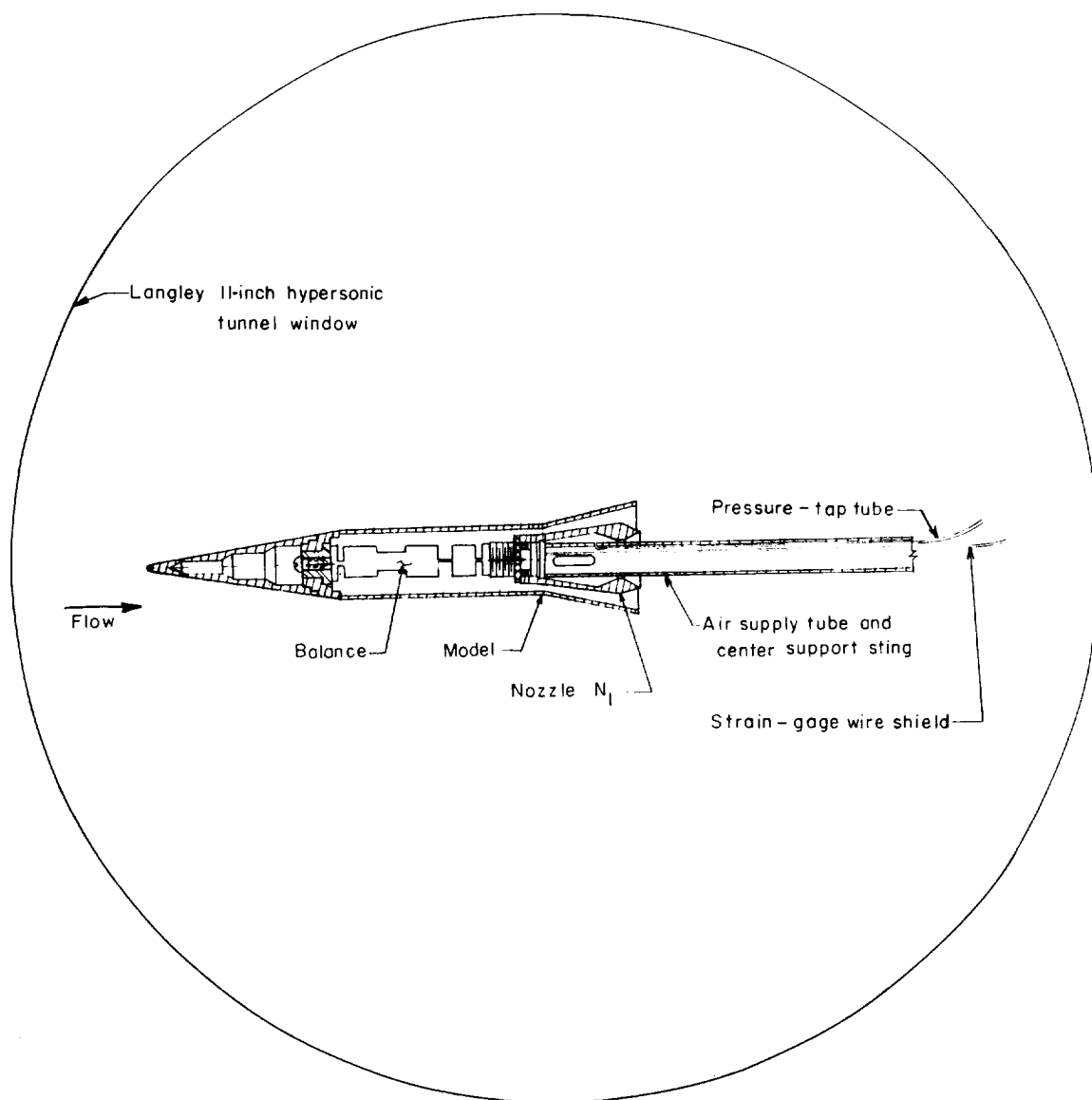


Figure 6.- Sketch showing cutaway assembly of model parts installed in the Langley 11-inch hypersonic tunnel.

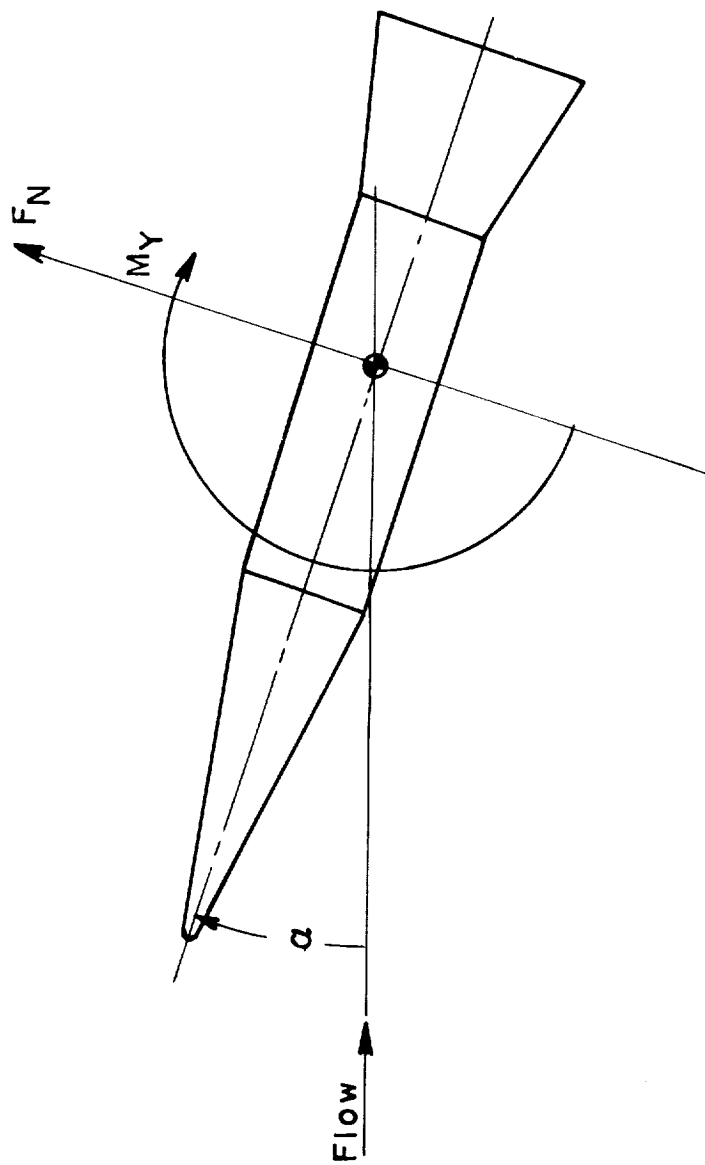


Figure 7.- Body-axis system. (Arrows indicate positive direction.)

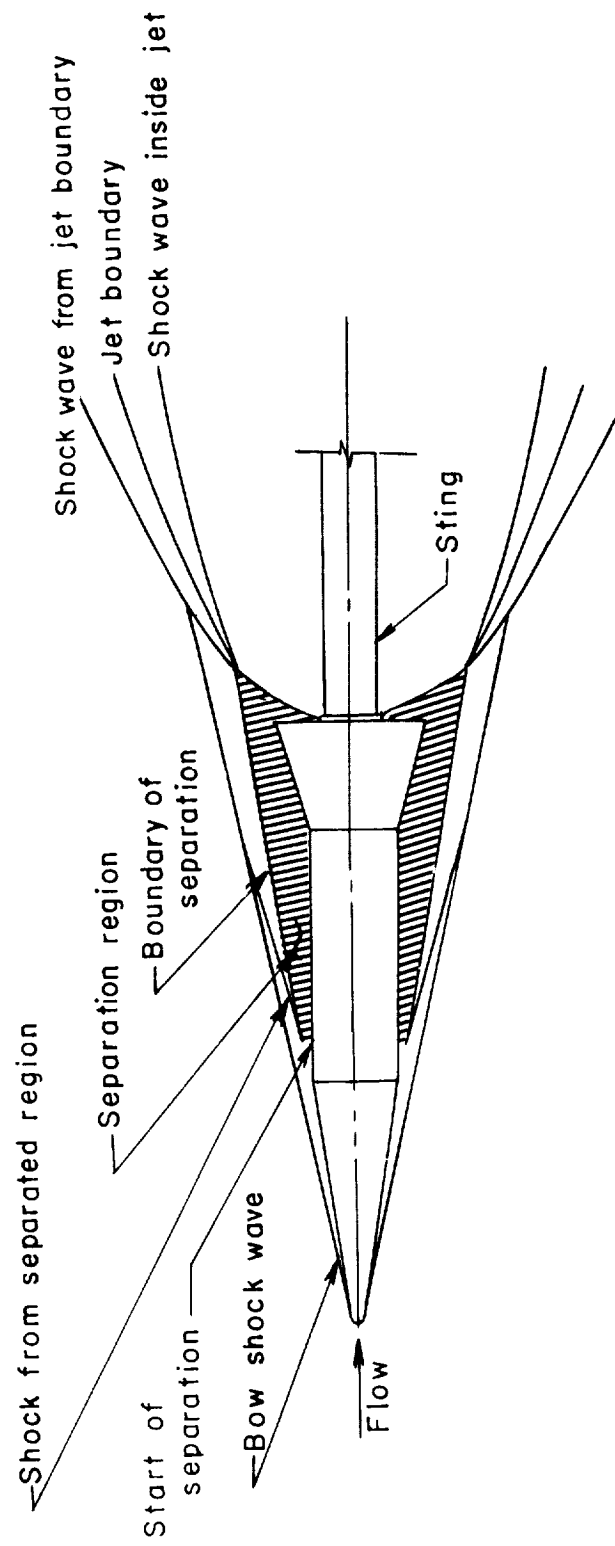
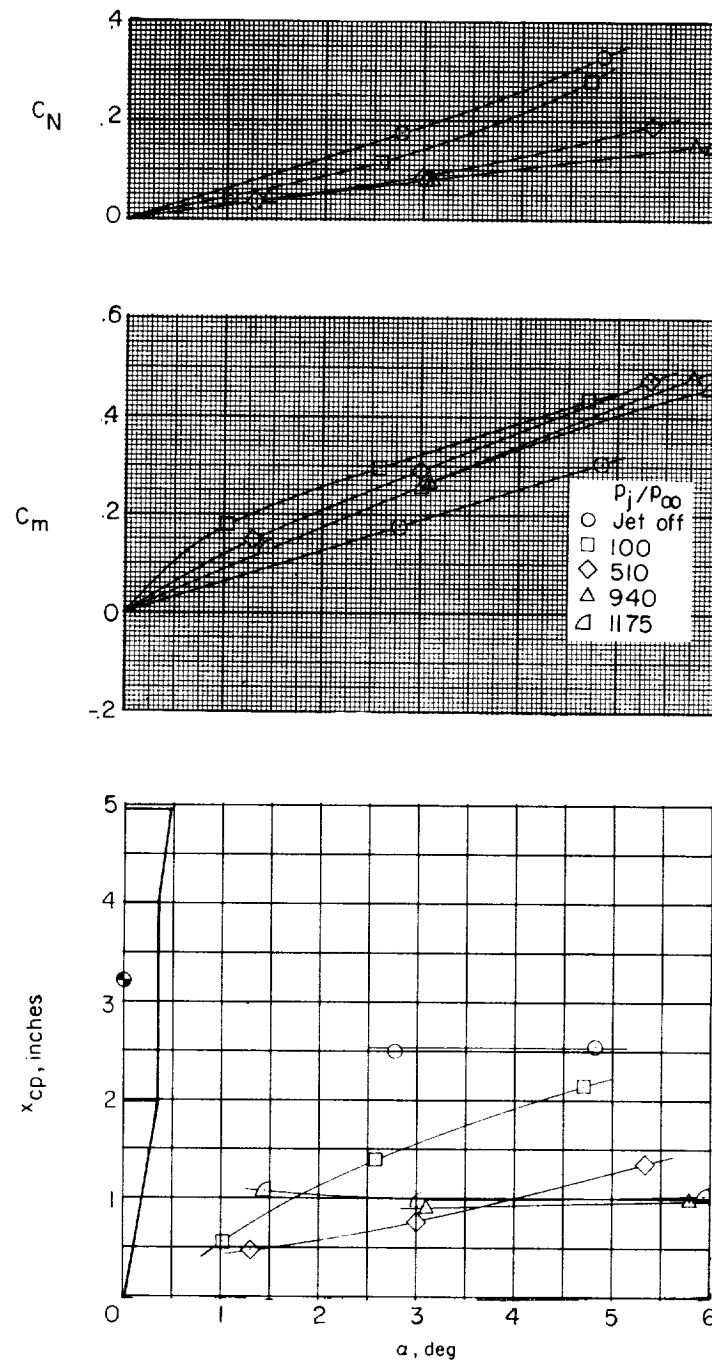


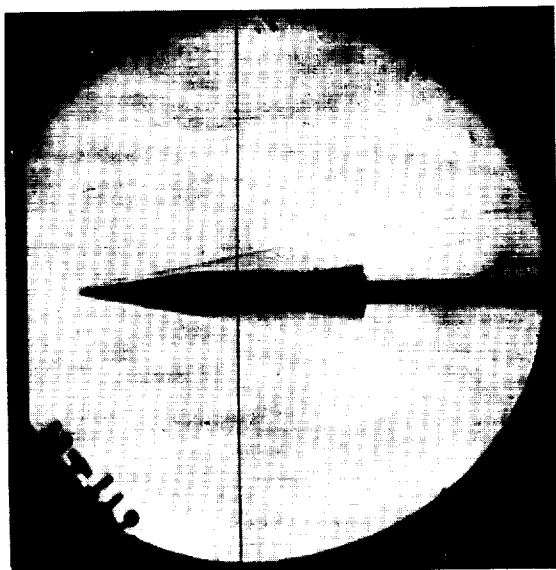
Figure 8.- Nomenclature of the flow field about model $C_{1BF16N1}$ at $\alpha = 0^\circ$.



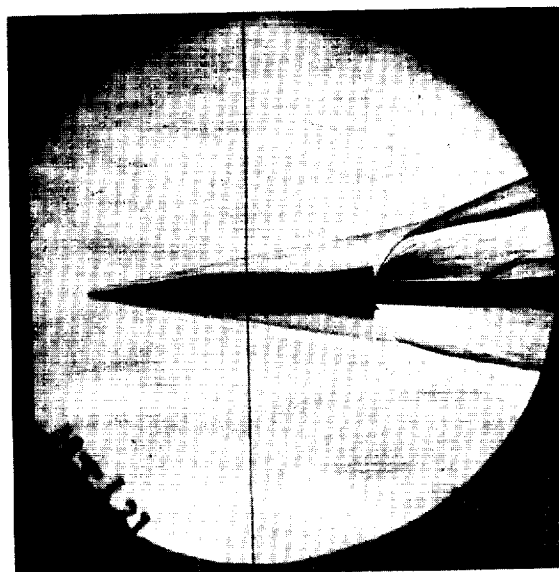
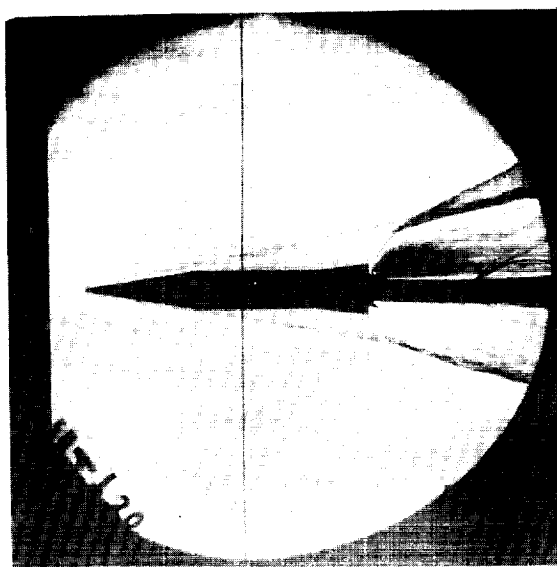
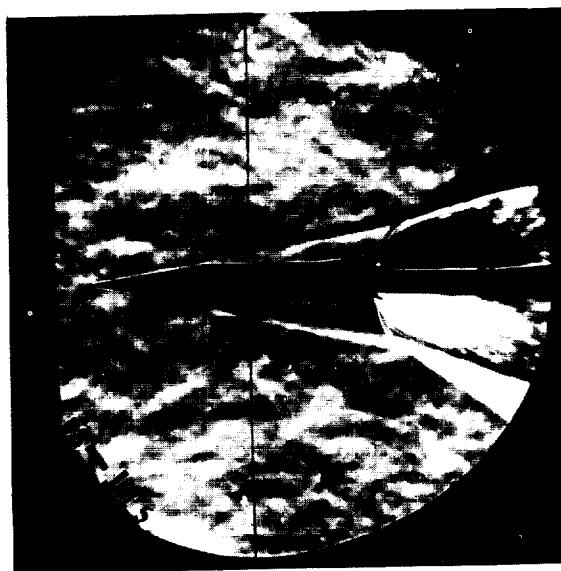
(a) C_N , C_m , and x_{cp} .

Figure 9.- The variation of C_N , C_m , and x_{cp} with angle of attack and pressure ratio for model $C_1BF_7N_1$ including schlieren photographs.

I-2039

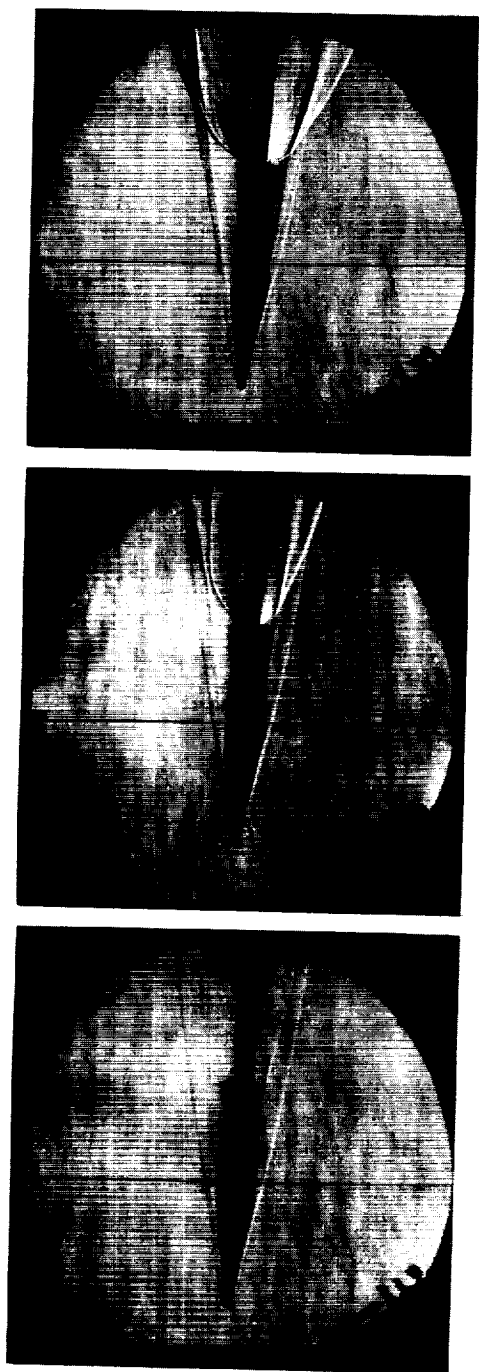


Jet off

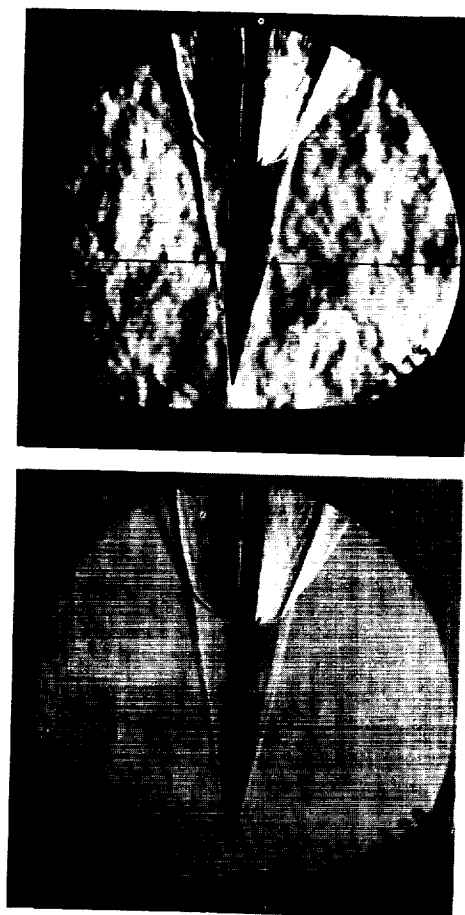
 $P_j/P_\infty = 510$  $P_j/P_\infty = 940$  $P_j/P_\infty = 1175$

(b) Schlieren photographs. $\alpha_m = 0^\circ$.

Figure 9.- Continued. L-62-60

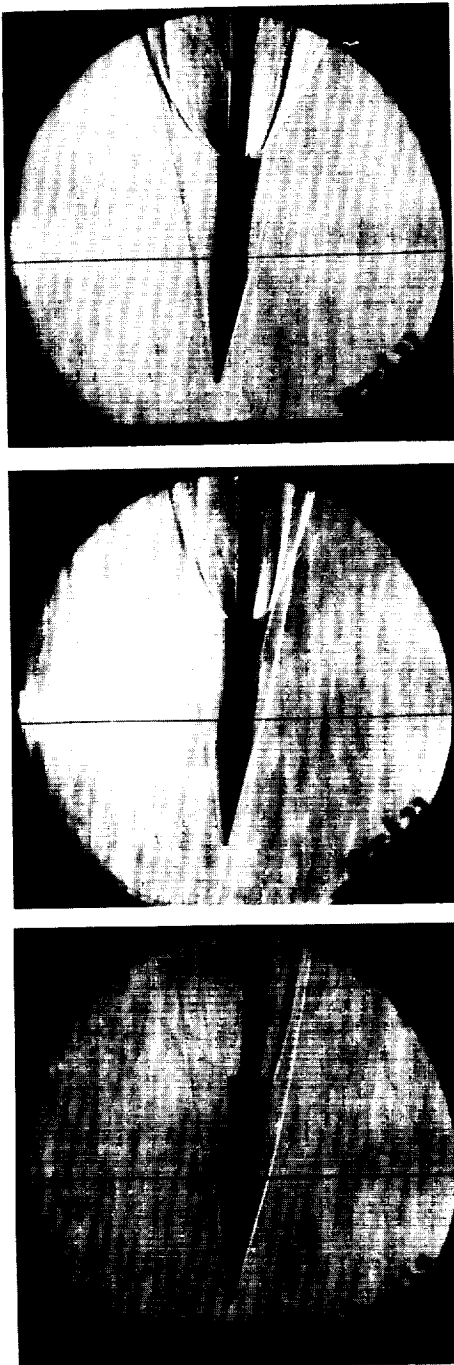

 $P_j/P_\infty = 510$
 $P_j/P_\infty = 100$

Jet off


 $P_j/P_\infty = 940$
 $P_j/P_\infty = 1175$

(c) Schlieren photographs. $\alpha_m = 3.00^\circ$.

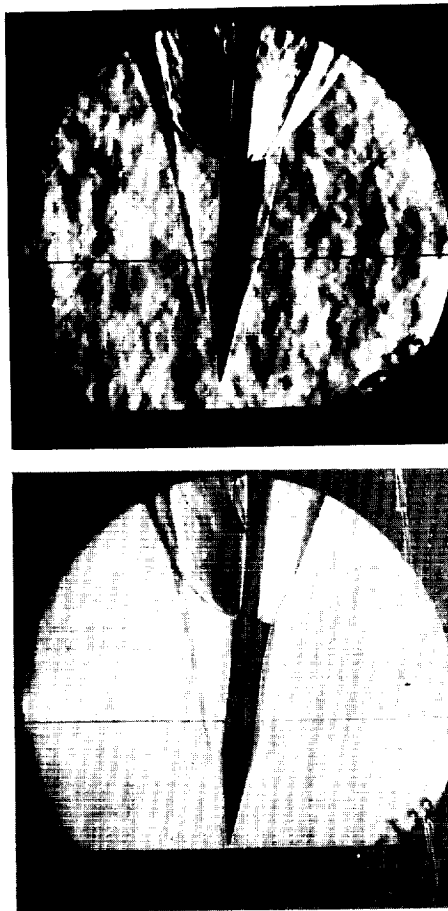
Figure 9.- Continued. L-62-61



Jet off

$P_j/P_\infty = 100$

$P_j/P_\infty = 510$

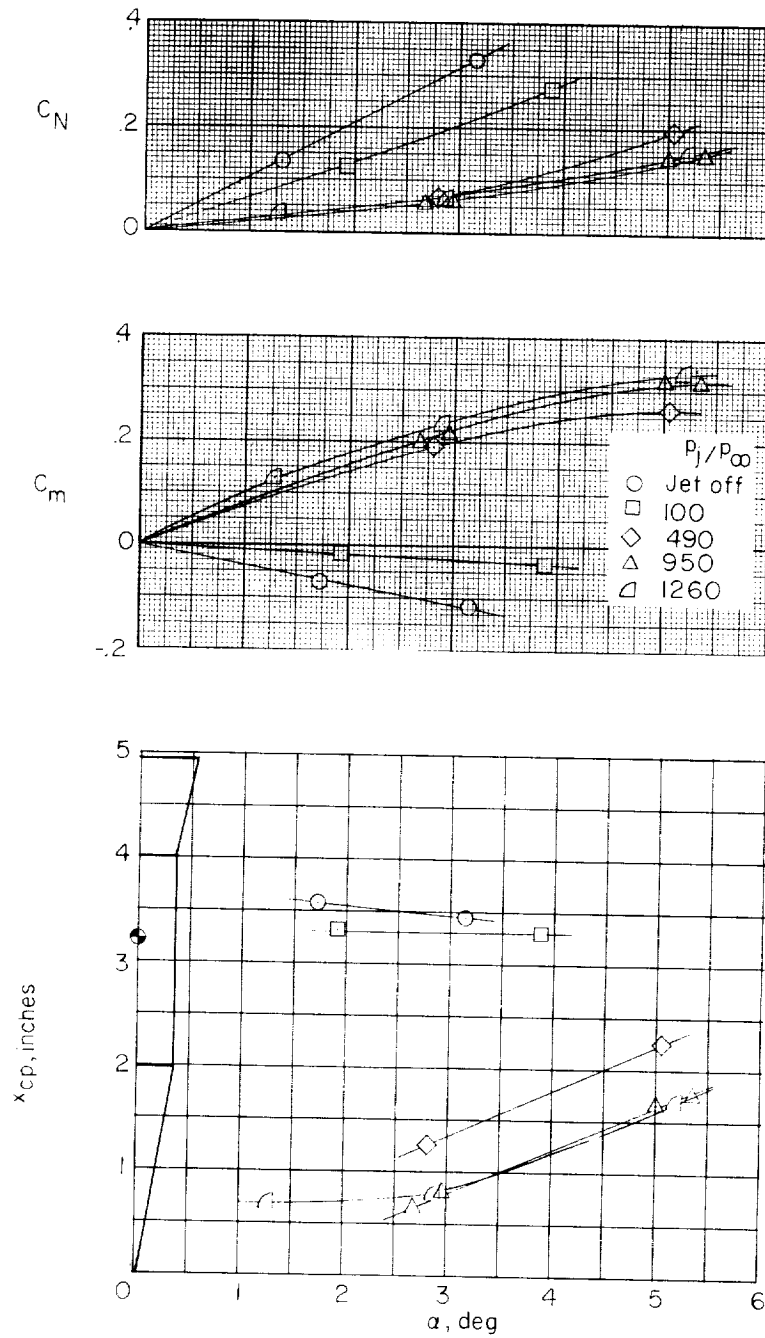


$P_j/P_\infty = 940$

$P_j/P_\infty = 1175$

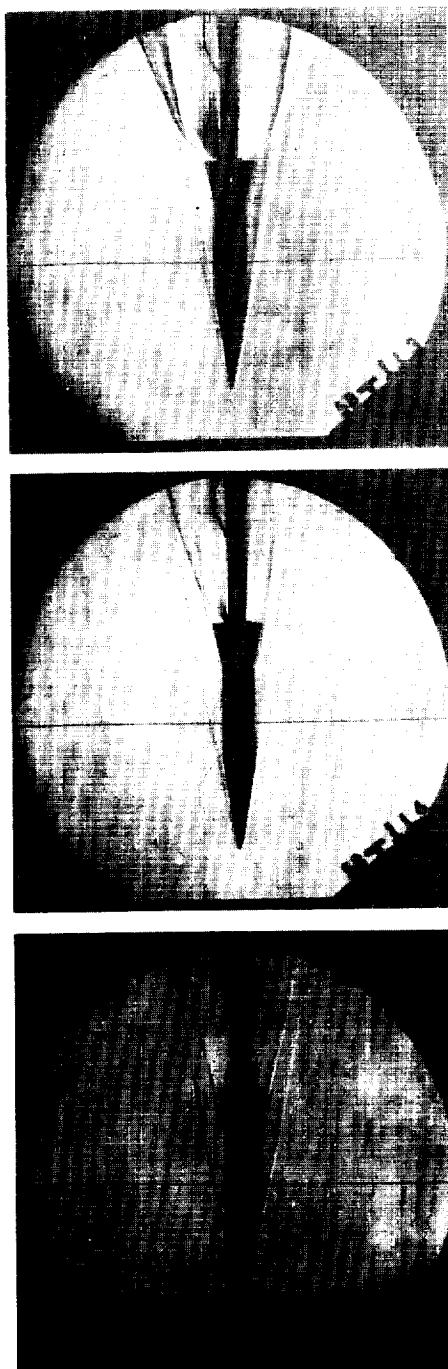
(d) Schlieren photographs. $\alpha_m = 6.00^\circ$.

Figure 9.- Concluded. L-62-62



(a) C_N , C_m , and x_{cp} .

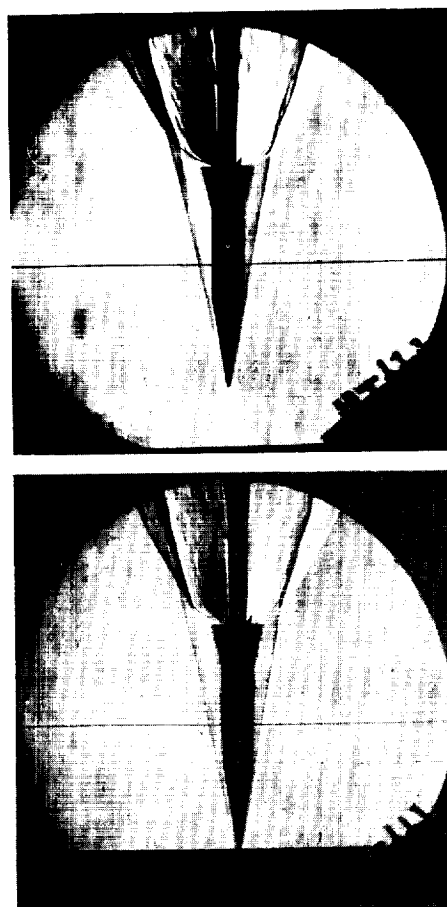
Figure 10.- The variation of C_N , C_m , and x_{cp} with angle of attack and pressure ratio for model $C_1BF_{13}N_1$ including schlieren photographs.



$p_j/p_\infty = 490$

$p_j/p_\infty = 100$

Jet off

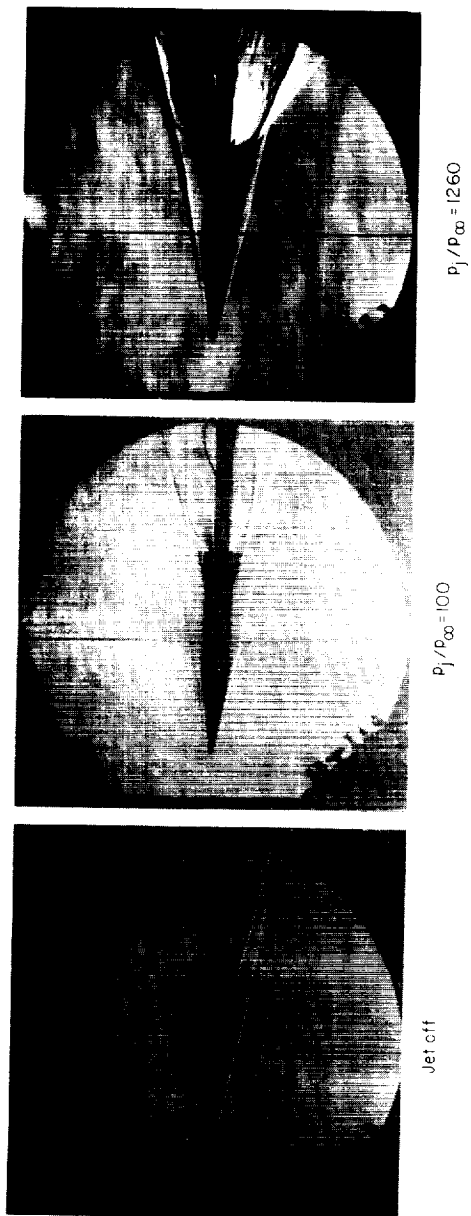


$p_j/p_\infty = 1260$

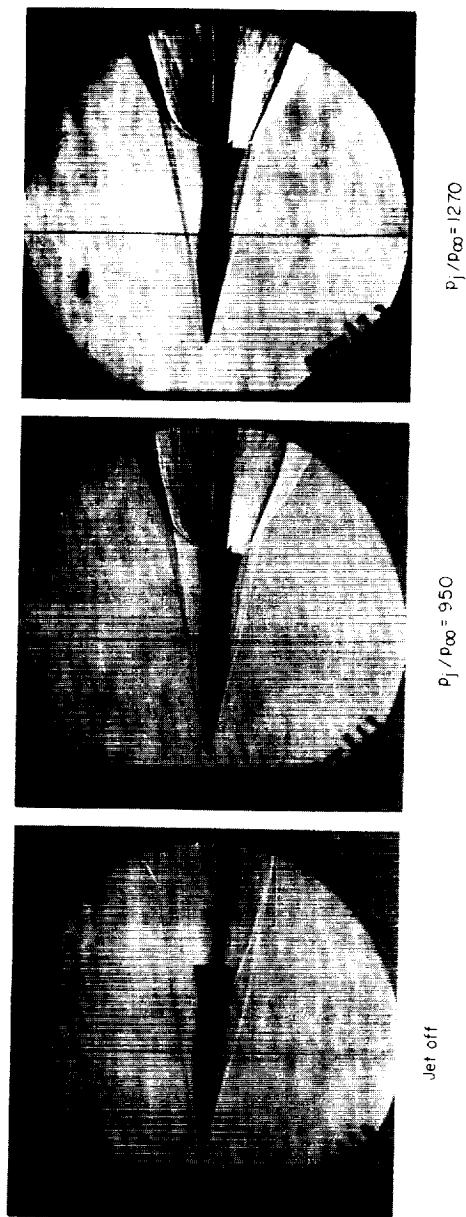
$p_j/p_\infty = 950$

(b) Schlieren photographs. $\alpha_m = 0^\circ$.

Figure 10.- Continued. L-62-63



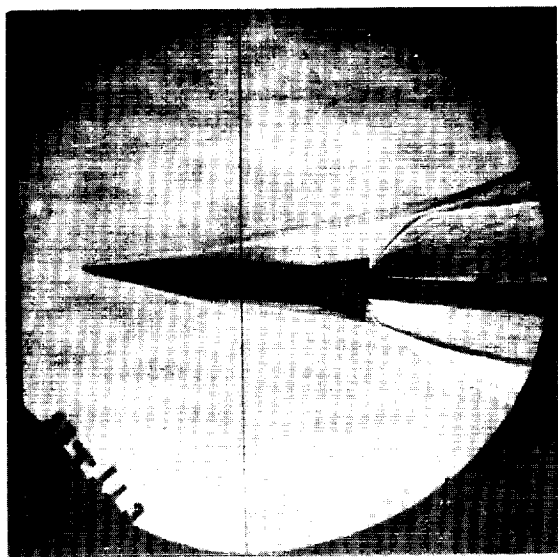
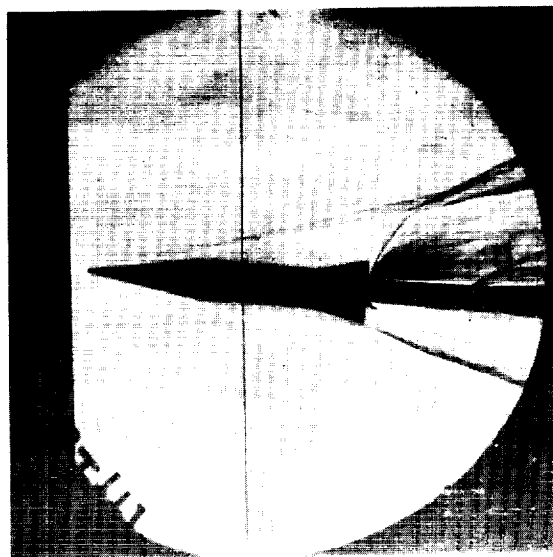
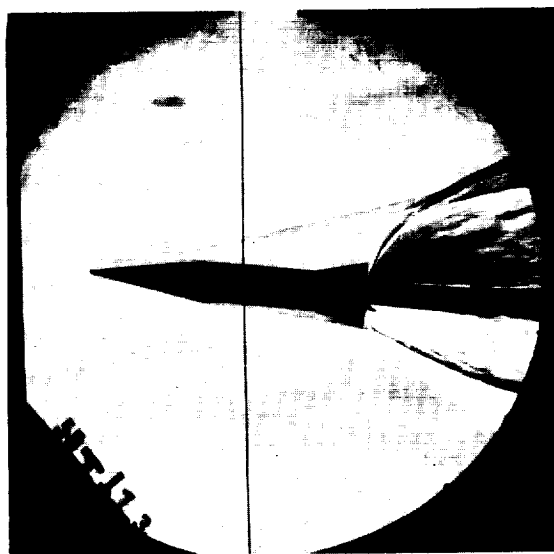
(c) Schlieren photographs. $\alpha_m = 1.75^\circ$.



(d) Schlieren photographs. $\alpha_m = 3.00^\circ$.

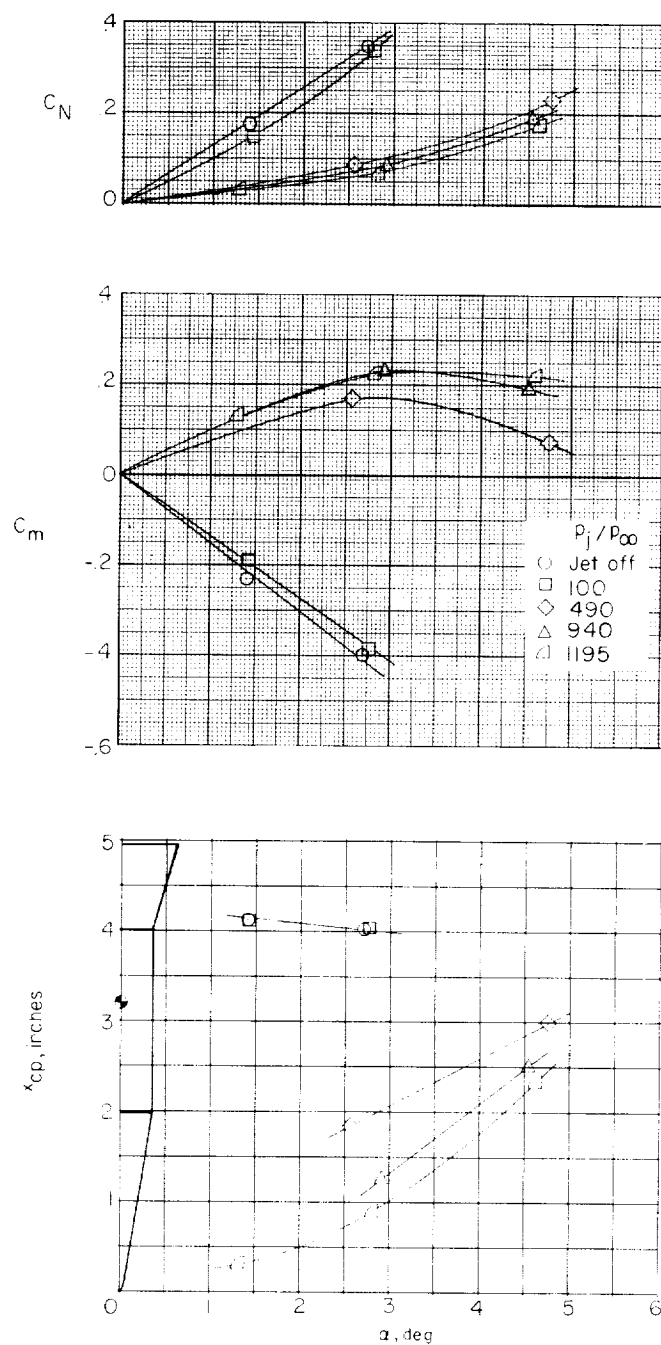
Figure 10.- Continued. L-62-64

L-2039


 $p_j / p_\infty = 490$

 $p_j / p_\infty = 950$

 $p_j / p_\infty = 1270$

(e) Schlieren photographs. $\alpha_m = 5.25^\circ$.

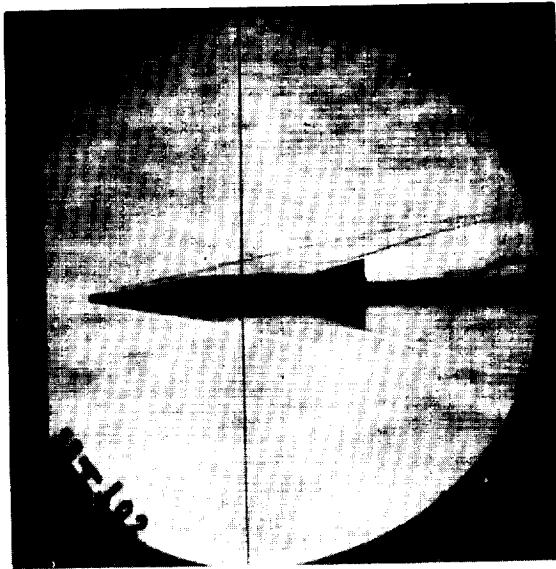
Figure 10.- Concluded. L-62-65



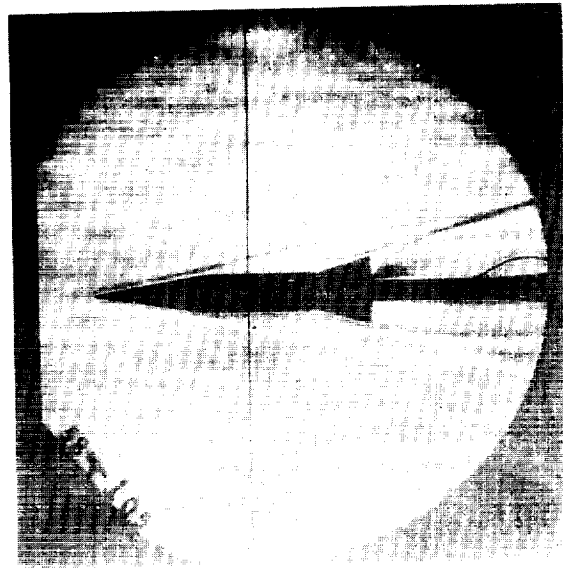
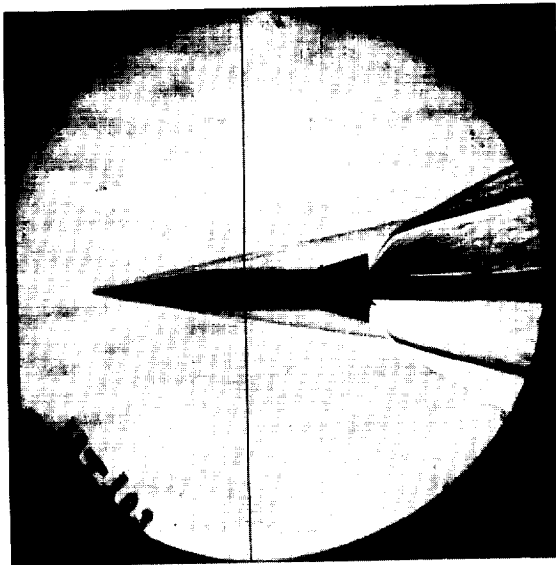
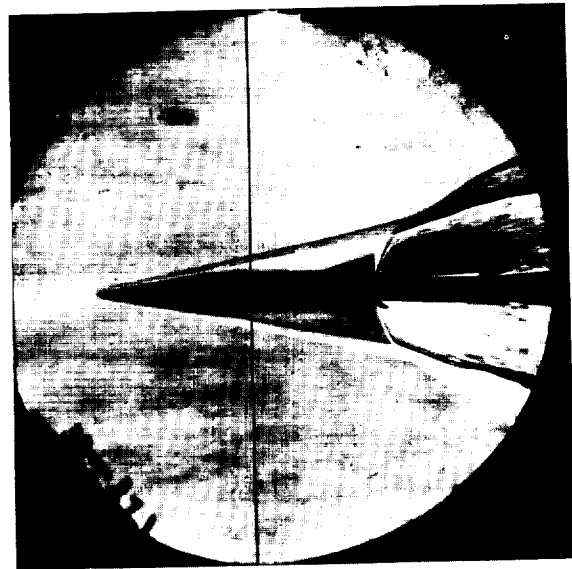
(a) C_N , C_m , and x_{cp} .

Figure 11.- The variation of C_N , C_m , and x_{cp} with angle of attack and pressure ratio for model $C_1BF_{16}N_1$ including schlieren photographs.

L-2039

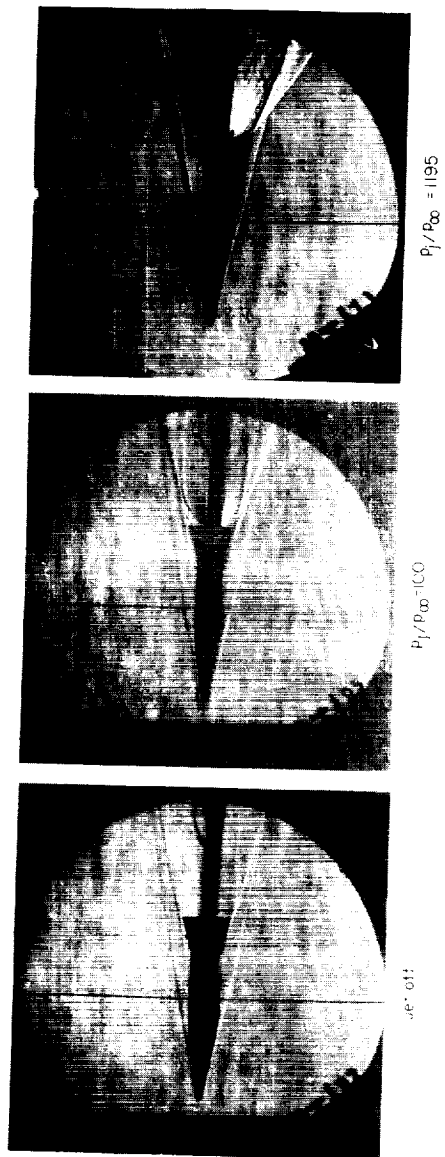


Jet off

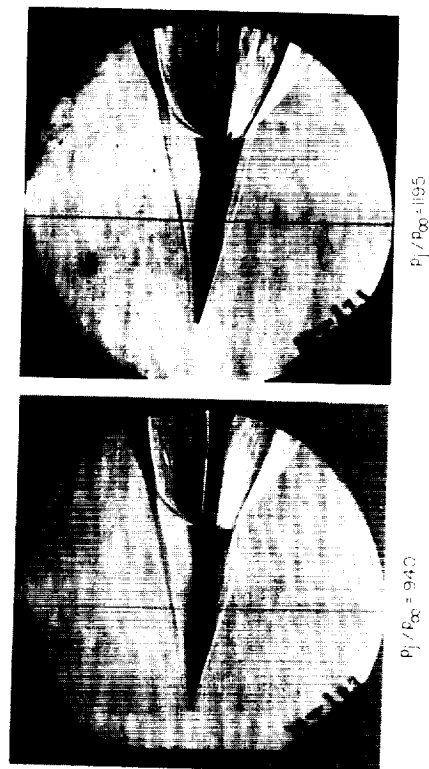
 $P_j/P_\infty = 100$  $P_j/P_\infty = 940$  $P_j/P_\infty = 1195$

(b) Schlieren photographs. $\alpha_m = 0^\circ$.

Figure 11.- Continued. L-62-66



(c) Schlieren photographs. $\alpha_m = 1.50^\circ$.



(d) Schlieren photographs. $\alpha_m = 4.50^\circ$.

Figure 11.- Concluded. L-62-67

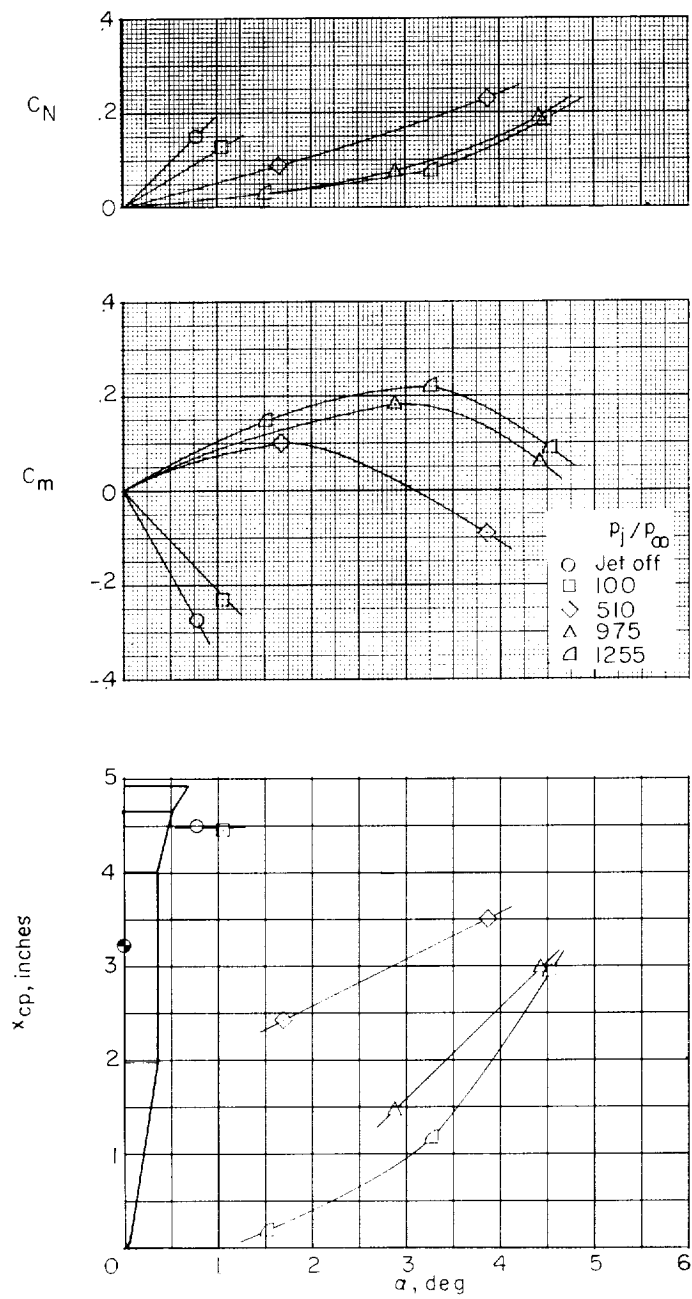
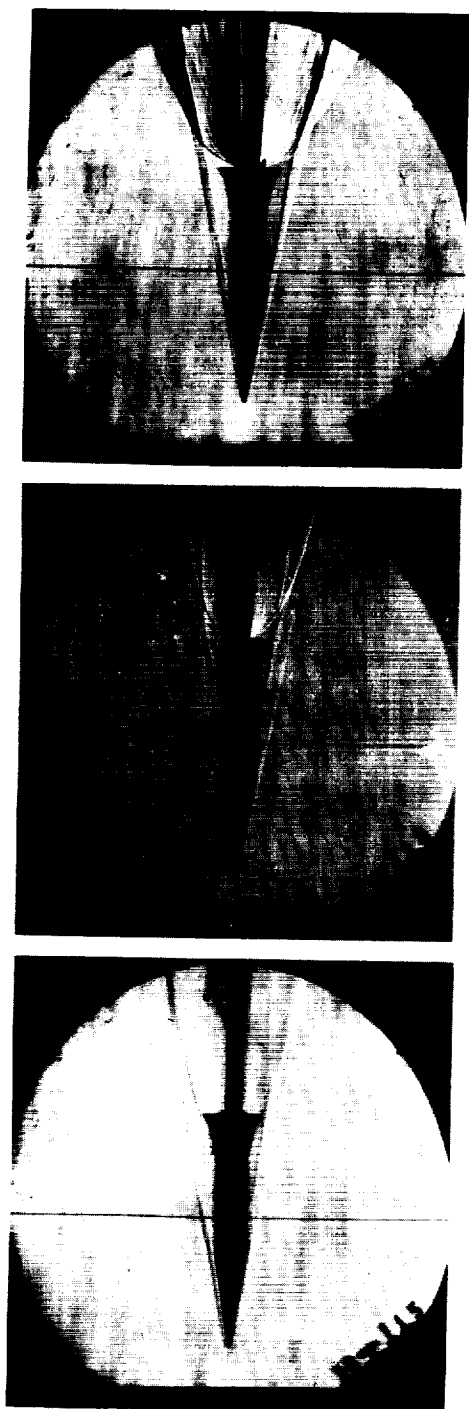
(a) C_N , C_m , and x_{cp} .

Figure 12.- The variation of C_N , C_m , and x_{cp} with angle of attack and pressure ratio for model $C_1BF_{13-31}N_1$ including schlieren photographs.



Jet off

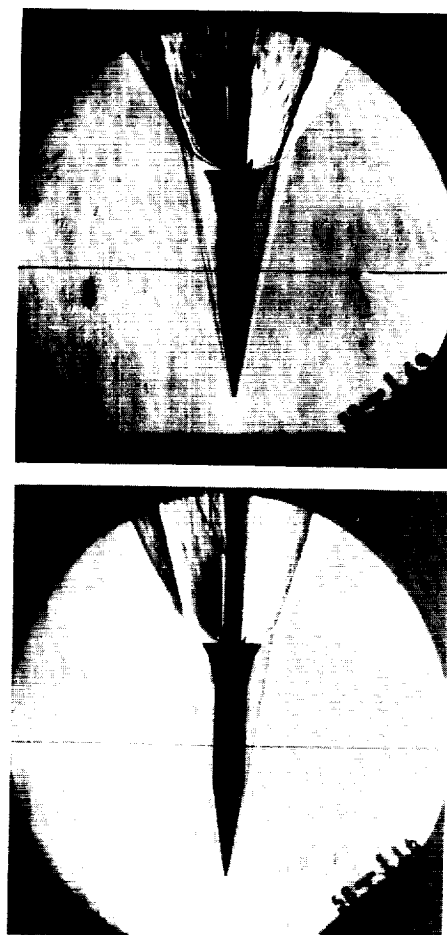
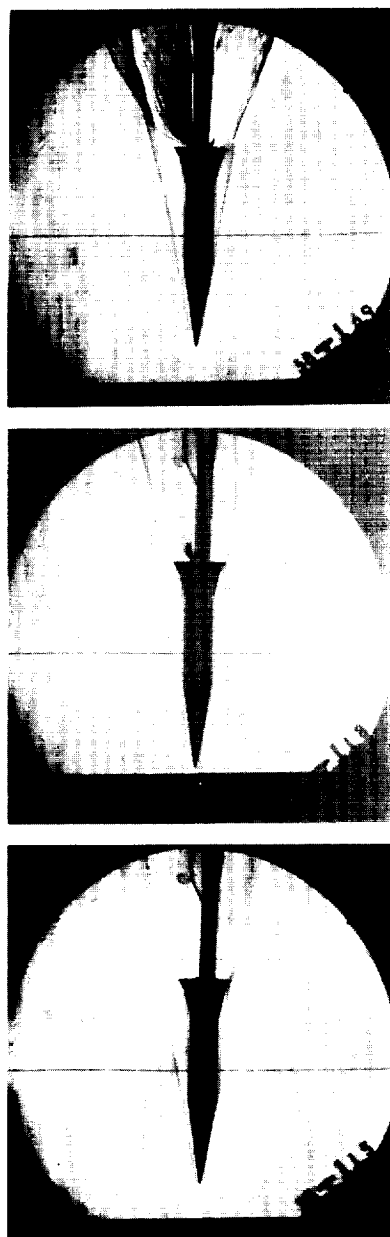
 $p_j/p_\infty = 100$ $p_j/p_\infty = 510$  $p_j/p_\infty = 975$ $p_j/p_\infty = 1255$ (b) Schlieren photographs. $\alpha_m = 0^\circ$.

Figure 12.- Continued. L-62-68

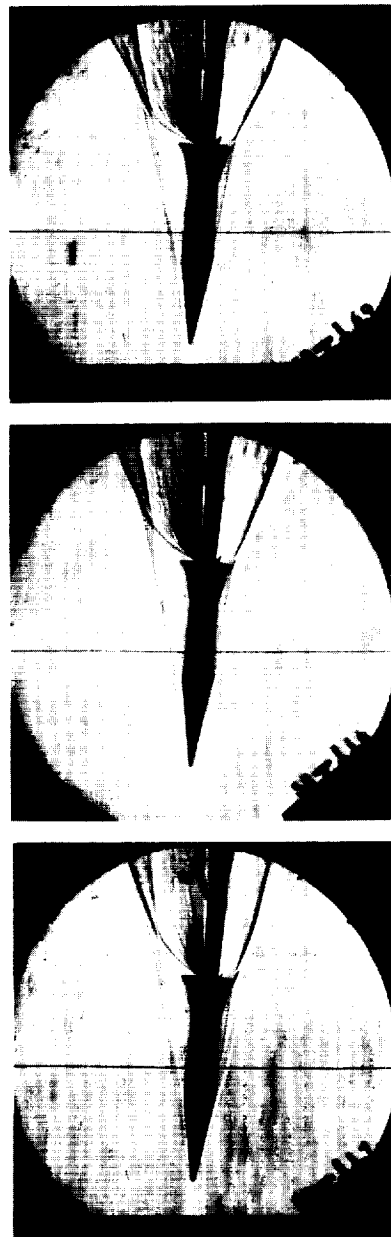


$P_1/P_0 = 1255$

$P_1/P_0 = 100$

Jet off

(c) Schlieren photographs. $\alpha_m = 1.00^\circ$.



$P_1/P_0 = 1255$

$P_1/P_0 = 975$

$P_1/P_0 = 510$

(d) Schlieren photographs. $\alpha_m = 4.00^\circ$.

Figure 12.- Concluded. L-62-69

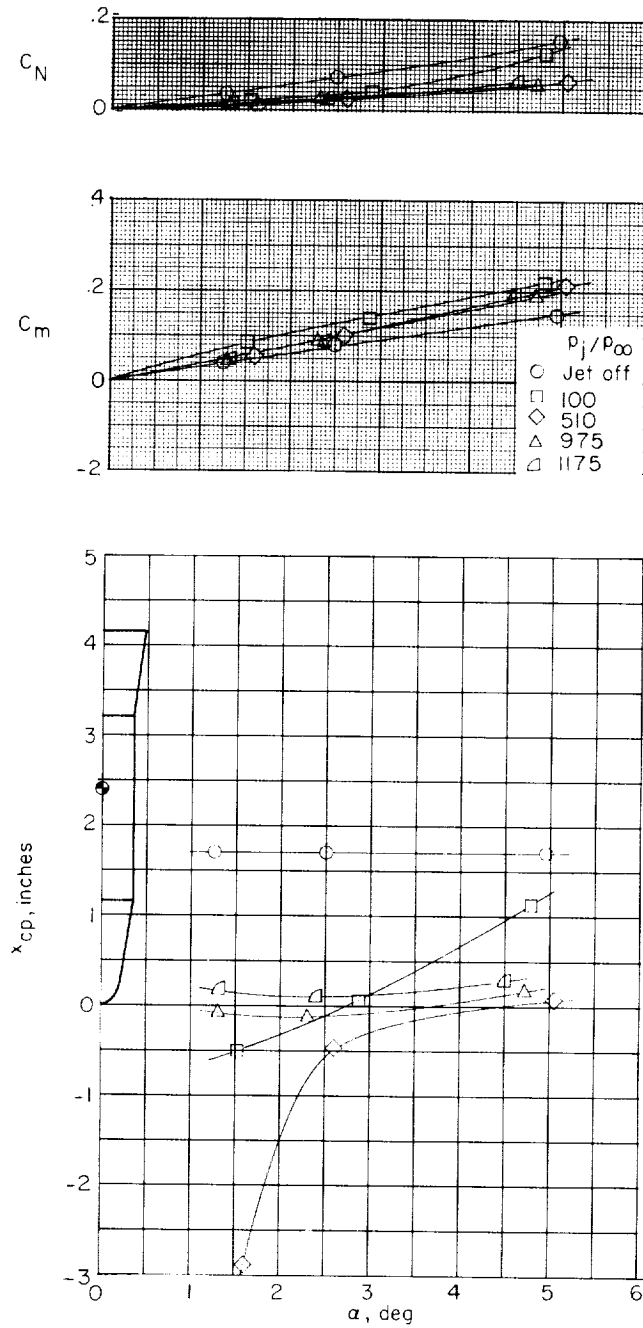
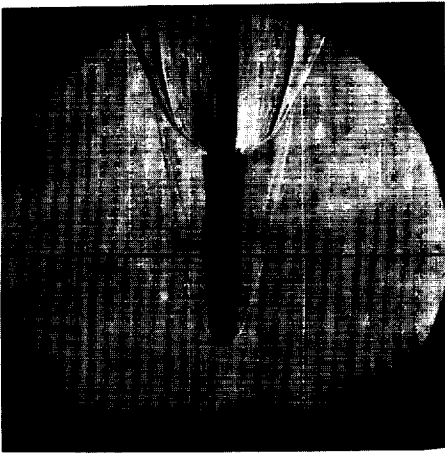
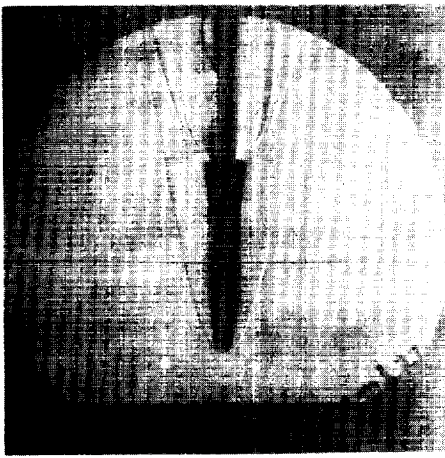
(a) C_N , C_m , and x_{cp} .

Figure 13.- The variation of C_N , C_m , and x_{cp} with angle of attack and pressure ratio for model C_{2BF7N1} including schlieren photographs.



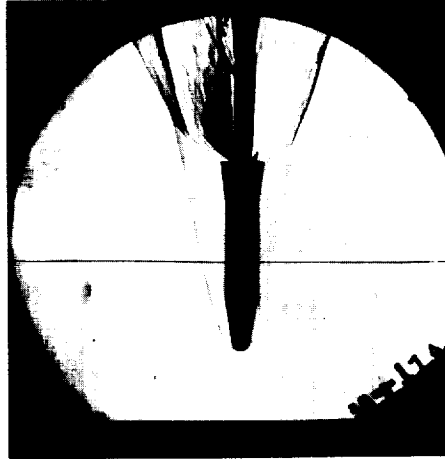
$P_j / P_\infty = 510$



$P_j / P_\infty = 100$



Jet off



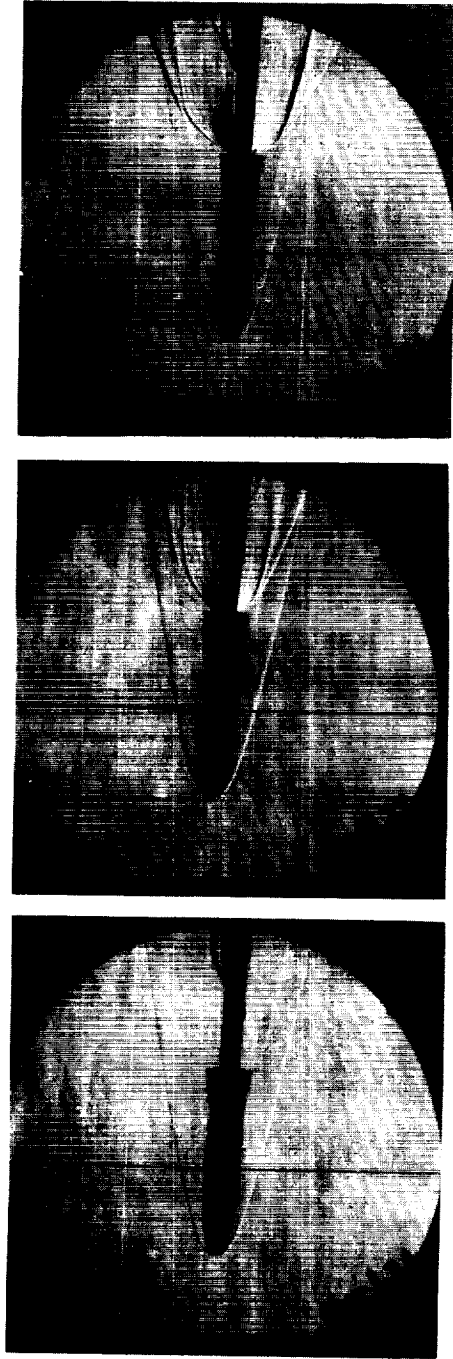
$P_j / P_\infty = 1175$



$P_j / P_\infty = 975$

(b) Schlieren photographs. $\alpha_m = 0^\circ$.

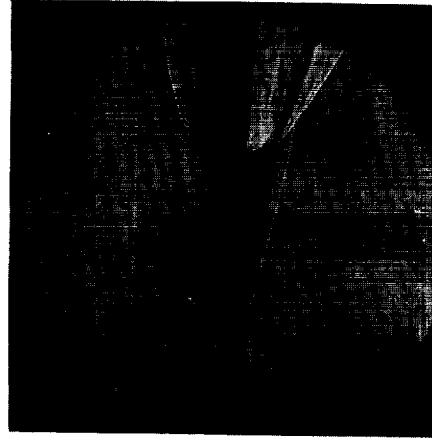
Figure 13.- Continued. L-62-70



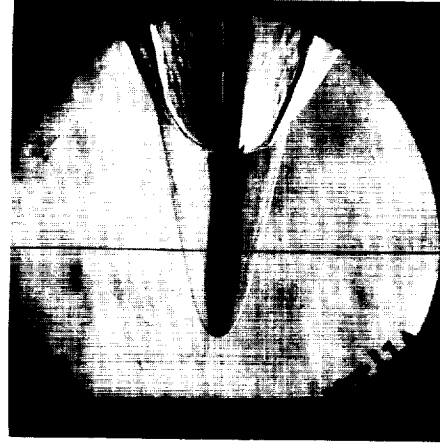
Jet off

$P_j/P_\infty = 100$

$P_j/P_\infty = 510$



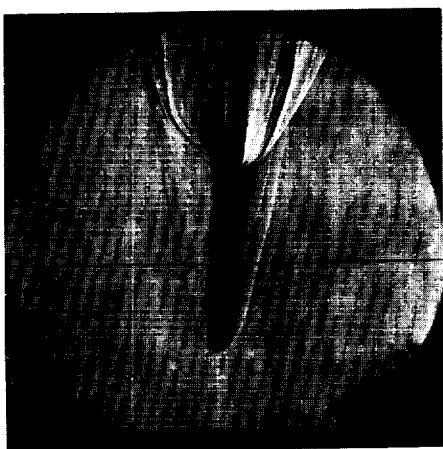
$P_j/P_\infty = 975$



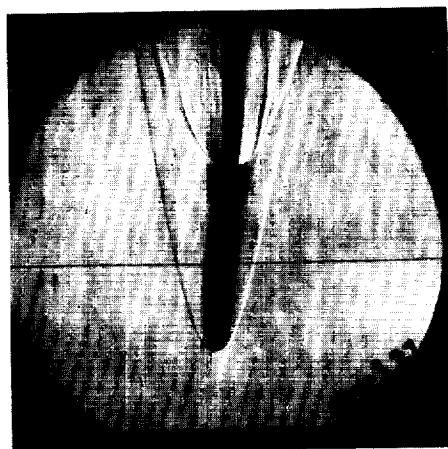
$P_j/P_\infty = 1175$

(c) Schlieren photographs. $\alpha_m = 2.50^\circ$.

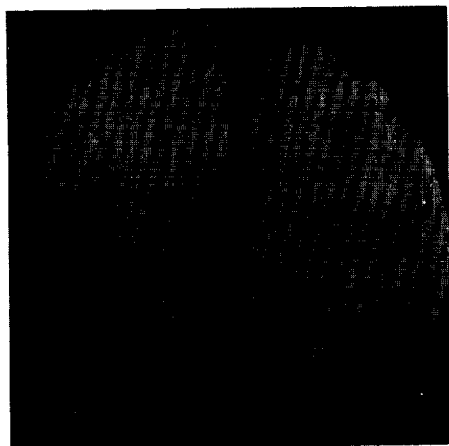
Figure 13.- Continued. L-62-71



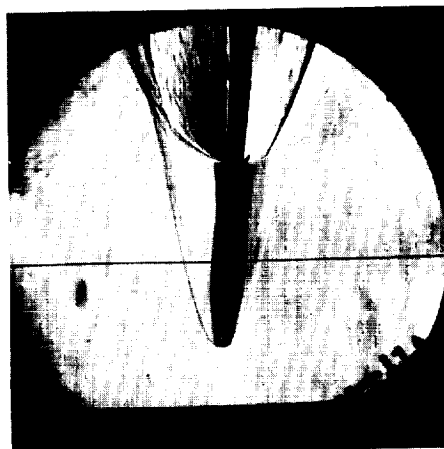
$p_j/p_\infty = 5.10$



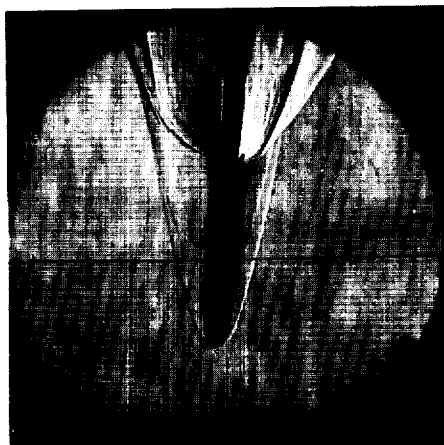
$p_j/p_\infty = 100$



Jet off



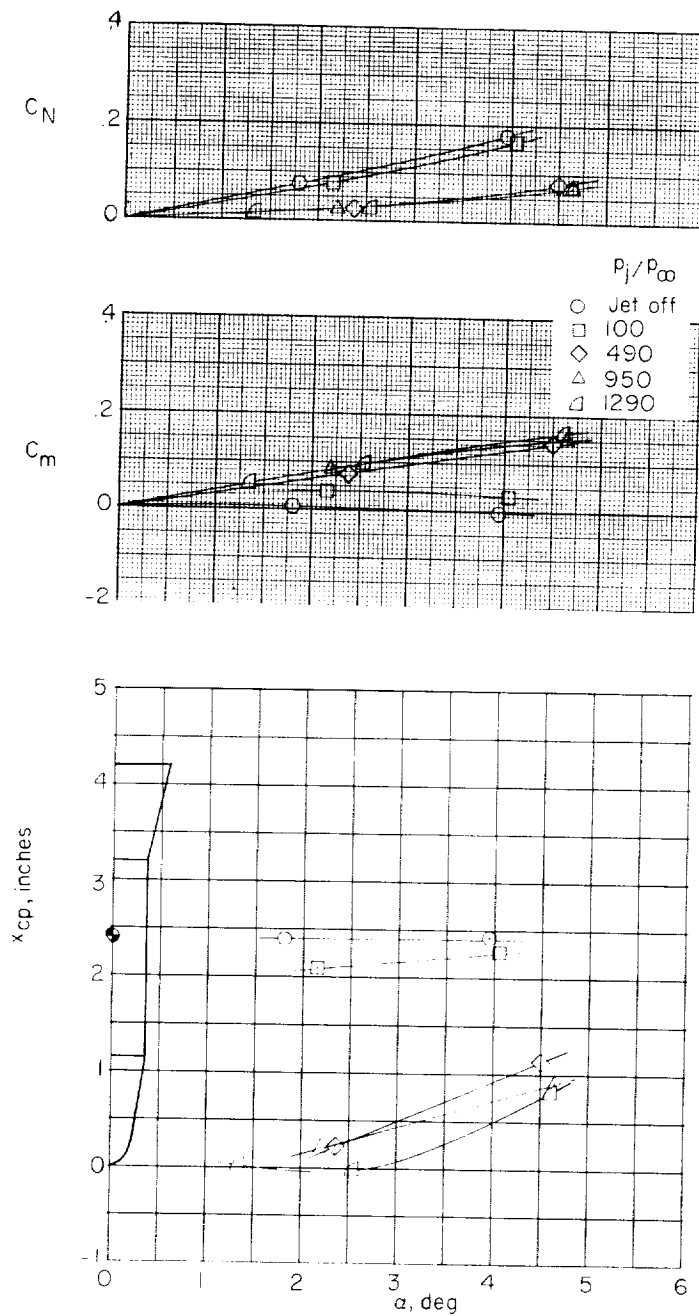
$p_j/p_\infty = 1175$



$p_j/p_\infty = 975$

(d) Schlieren photographs. $\alpha_m = 5.00^\circ$.

Figure 13.- Concluded. L-62-72



(a) C_N , C_m , and x_{cp} .

Figure 14.- The variation of C_N , C_m , and x_{cp} with angle of attack and pressure ratio for model $C_2BF_{13}N_1$ including schlieren photographs.



Jet off

$p_j/p_\infty = 100$

$p_j/p_\infty = 490$

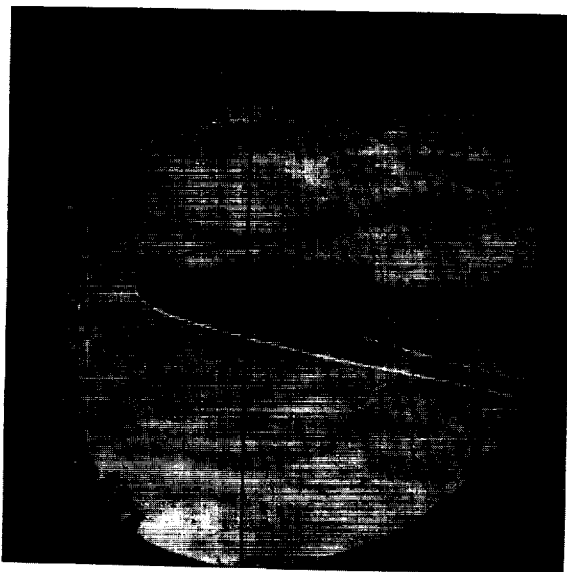


$p_j/p_\infty = 950$

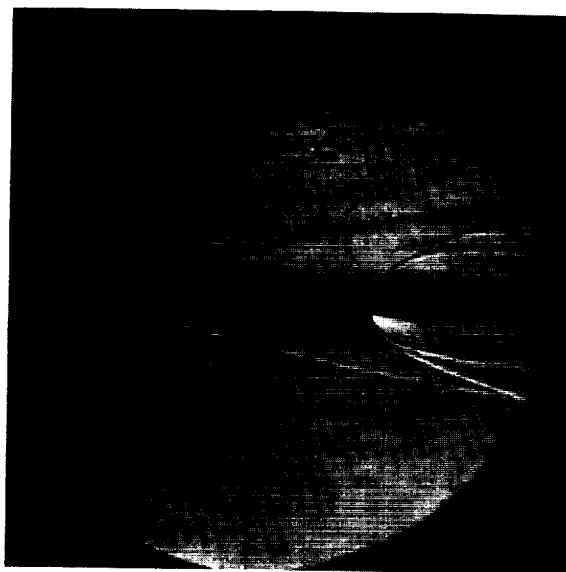
$p_j/p_\infty = 1290$

(b) Schlieren photographs. $\alpha_m = 0^\circ$.

Figure 14.- Continued. L-62-73

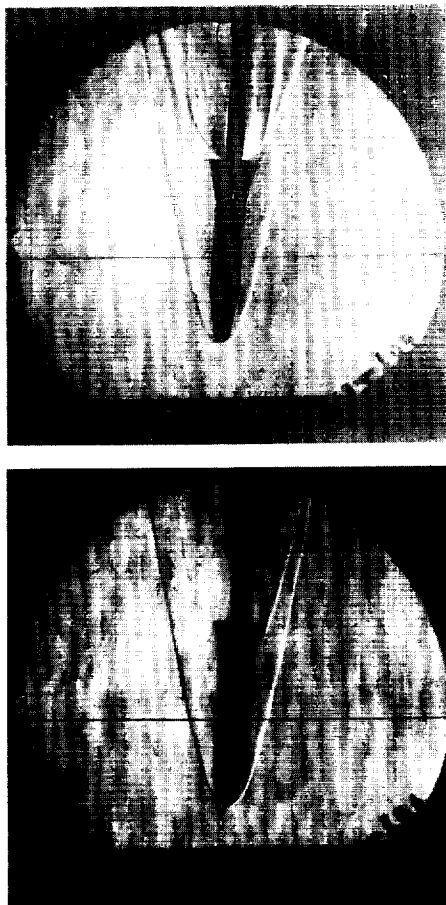


Jet off

 $P_j/P_\infty = 100$  $P_j/P_\infty = 4.90$  $P_j/P_\infty = 1290$

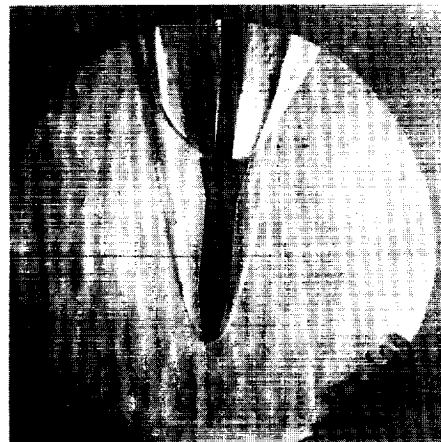
(c) Schlieren photographs. $\alpha_m = 2.00^\circ$.

Figure 14.- Continued. L-62-74

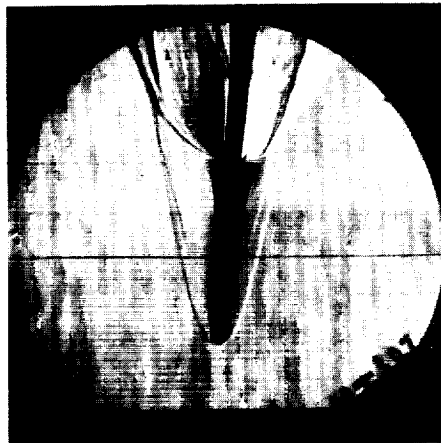


Jet off

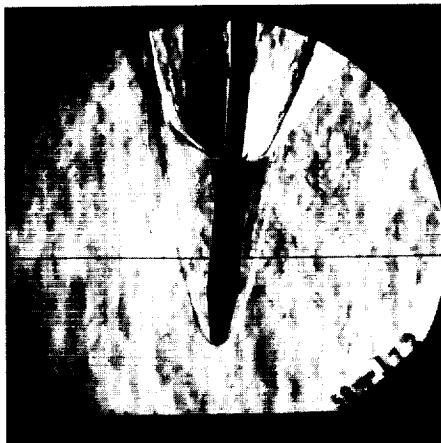
$p_j / p_\infty = 100$



$p_j / p_\infty = 490$



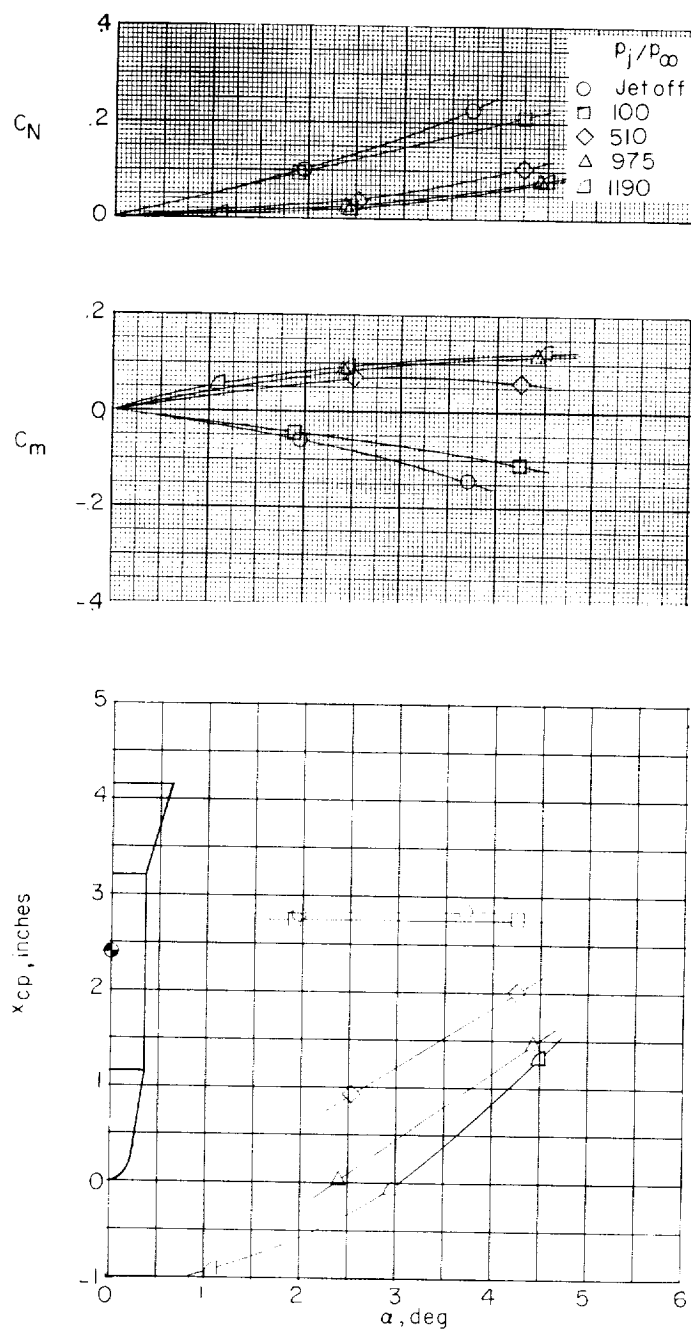
$p_j / p_\infty = 950$



$p_j / p_\infty = 1290$

(d) Schlieren photographs. $\alpha_m = 4.25^\circ$.

Figure 14.- Concluded. L-62-75



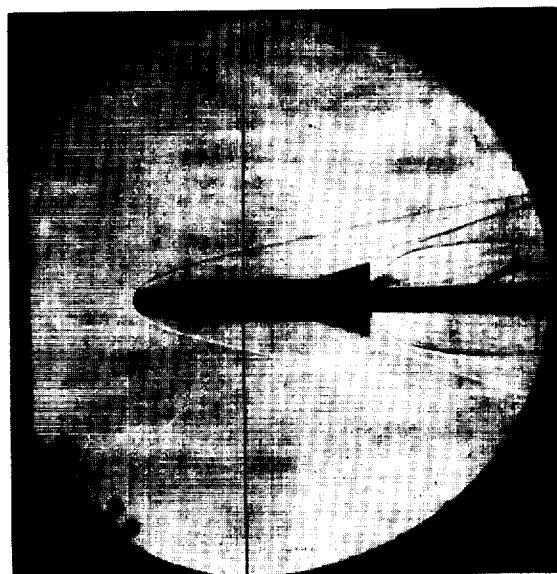
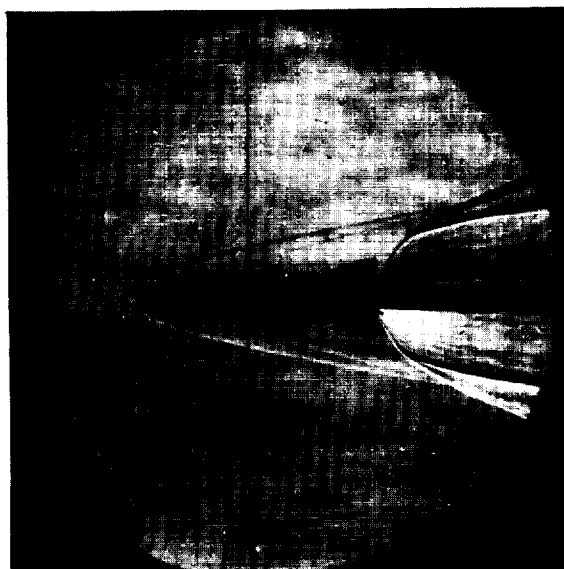
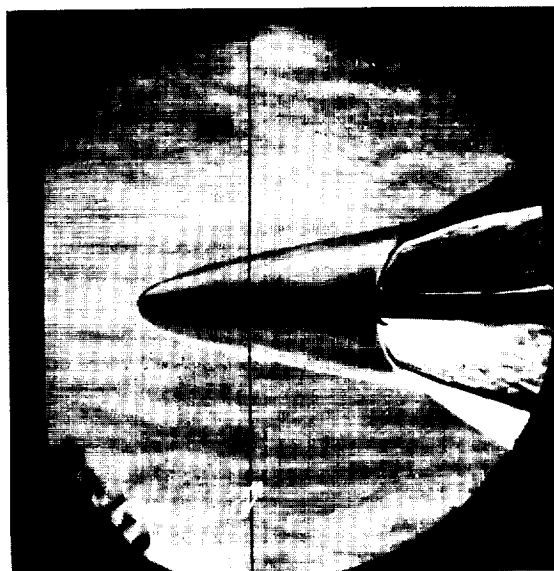
(a) C_N , C_m , and x_{cp} .

Figure 15.- The variation of C_N , C_m , and x_{cp} with angle of attack and pressure ratio for model $C_2BF_{16}N_1$ including schlieren photographs.

L-2039

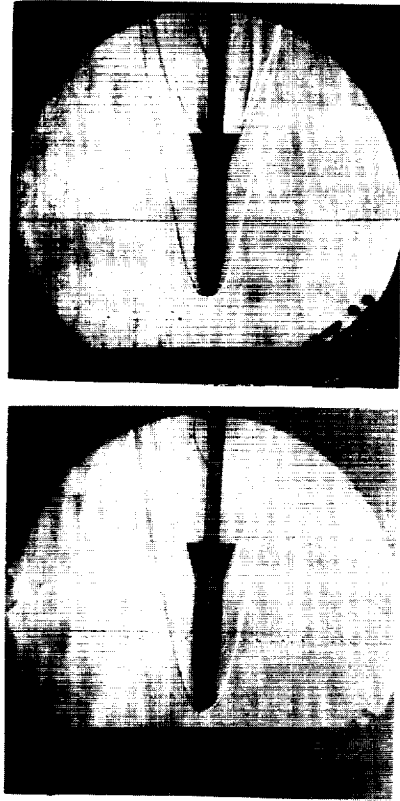


Jet off

 $p_j/p_\infty = 100$  $p_j/p_\infty = 510$  $p_j/p_\infty = 1190$

(b) Schlieren photographs. $\alpha_m = 0^\circ$.

Figure 15.- Continued. L-62-76



Jet off

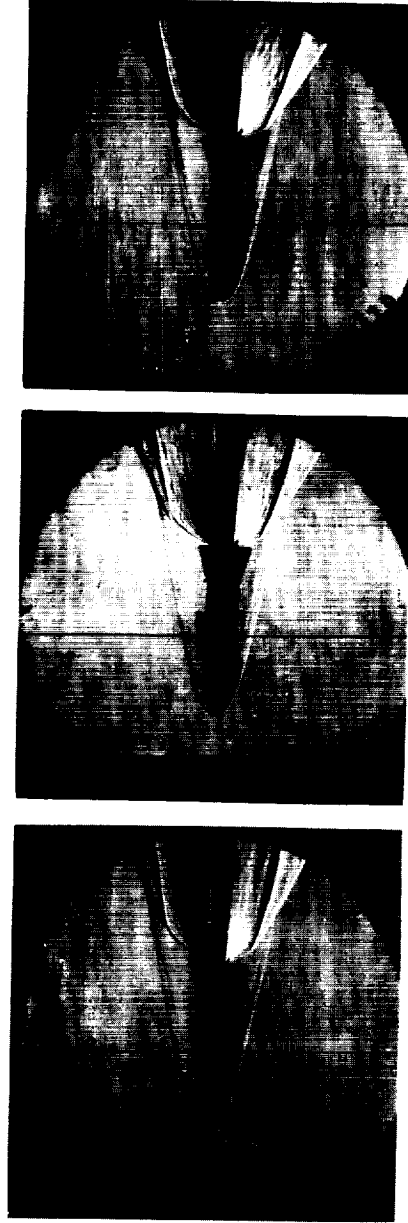
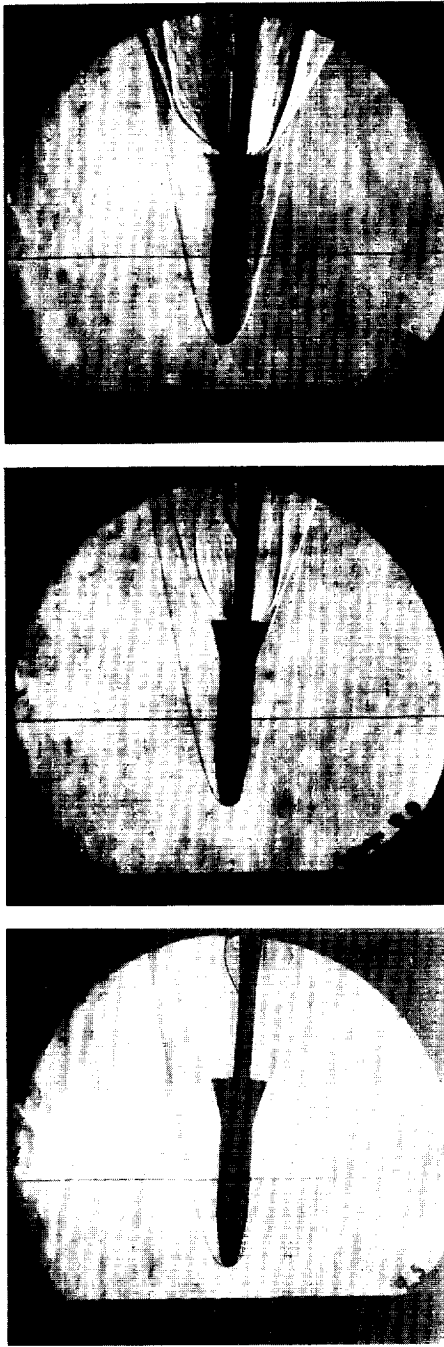
 $P_1/P_\infty = 100$ (c) Schlieren photographs. $\alpha_m = 2.00^\circ$. $P_1/P_\infty = 510$ $P_1/P_\infty = 975$ $P_1/P_\infty = 1190$ (d) Schlieren photographs. $\alpha_m = 2.75^\circ$.

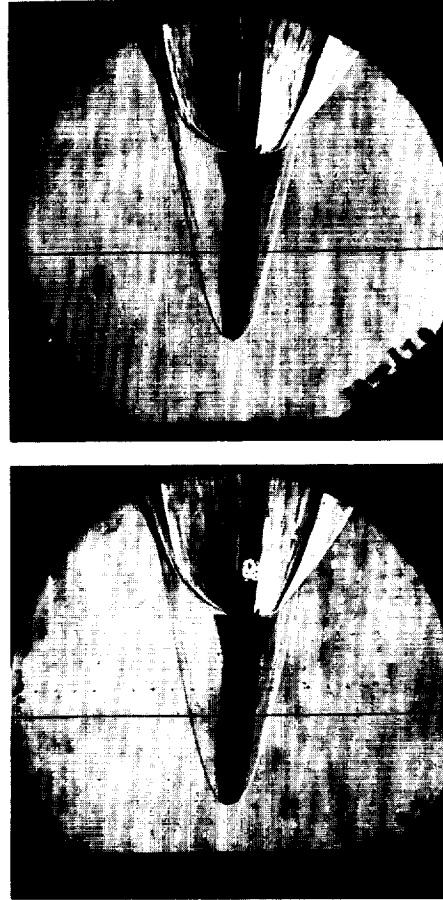
Figure 15.- Continued. L-62-77



$p_j/p_\infty = 510$

$p_j/p_\infty = 100$

Jet off



$p_j/p_\infty = 975$

$p_j/p_\infty = 1190$

(e) Schlieren photographs. $\alpha_m = 4.00^\circ$.

Figure 15.- Concluded. L-62-78

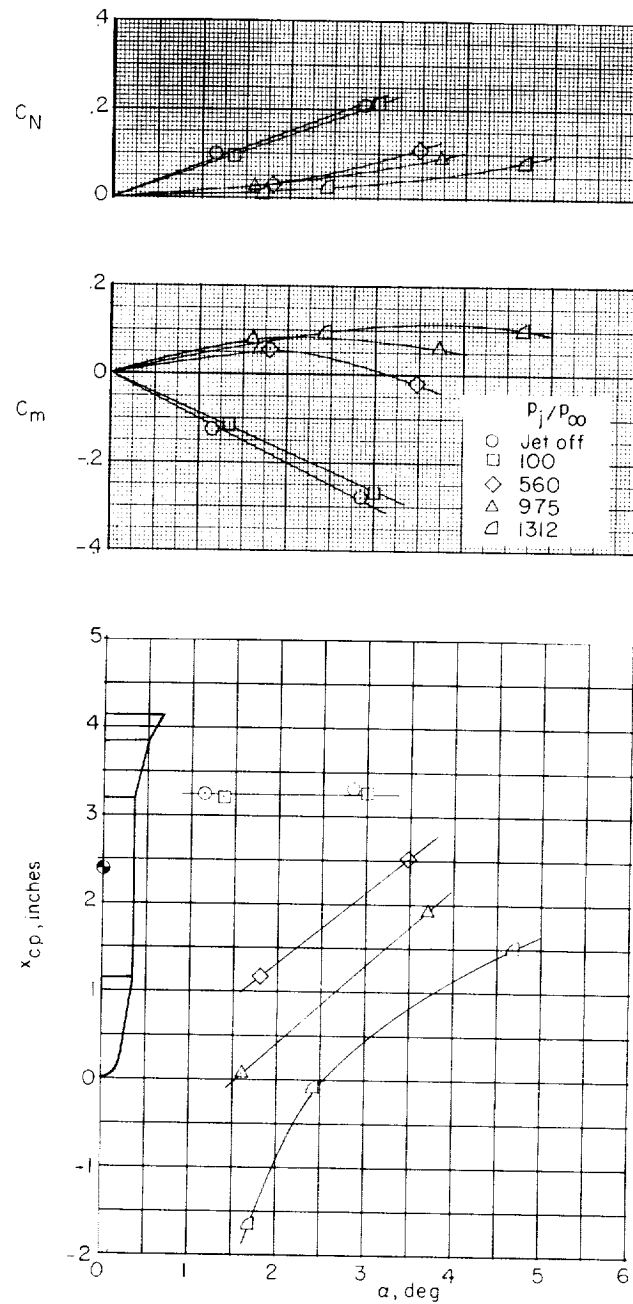
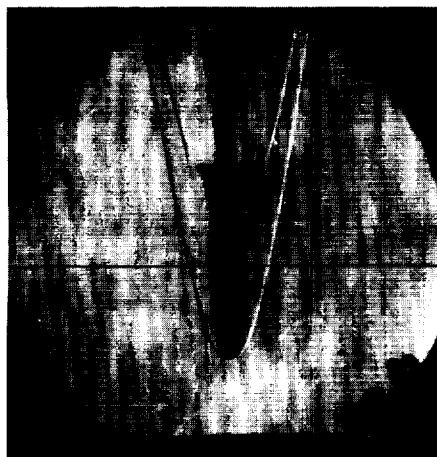
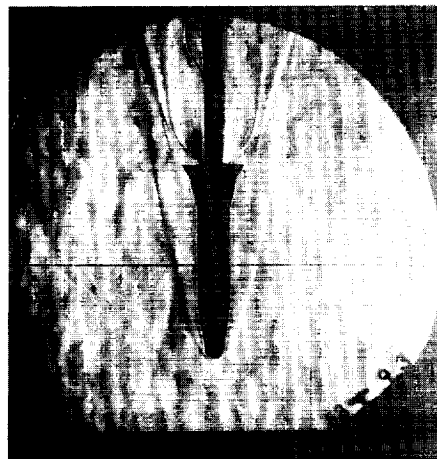
(a) C_N , C_m , and x_{cp} .

Figure 16.- The variation of C_N , C_m , and x_{cp} with angle of attack and pressure ratio for model $C_2Bf_{13-31}N_1$ including schlieren photographs.



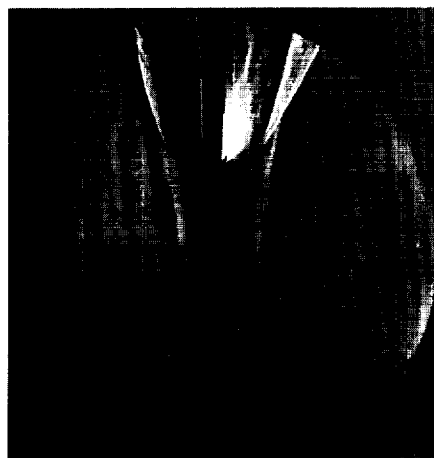
Jet off



$p_j/p_\infty = 100$



$p_j/p_\infty = 560$



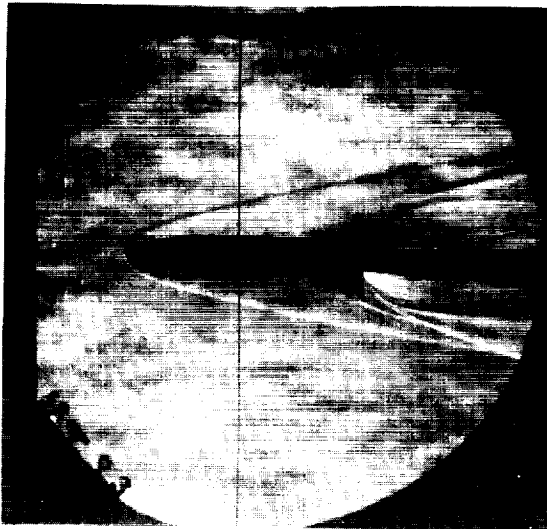
$p_j/p_\infty = 975$



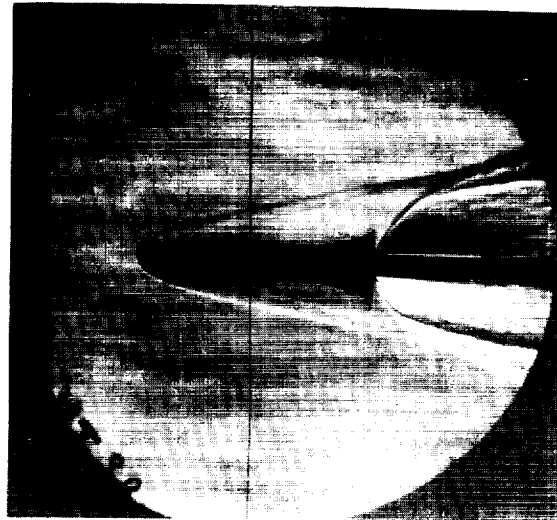
$p_j/p_\infty = 1312$

(b) Schlieren photographs. $\alpha_m = 0^\circ$.

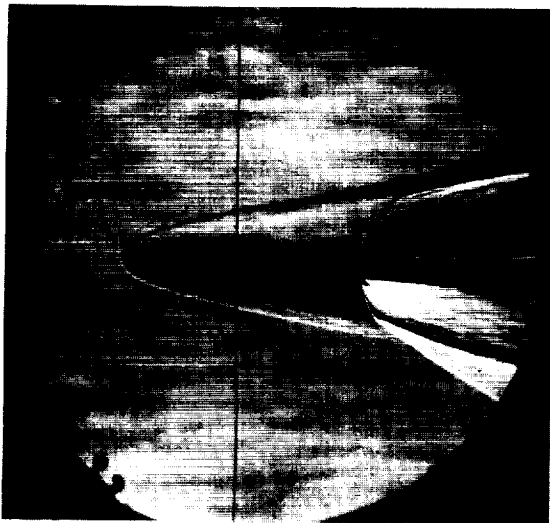
Figure 16.- Continued. L-62-79



$P_j/P_\infty = 100$



$P_j/P_\infty = 560$



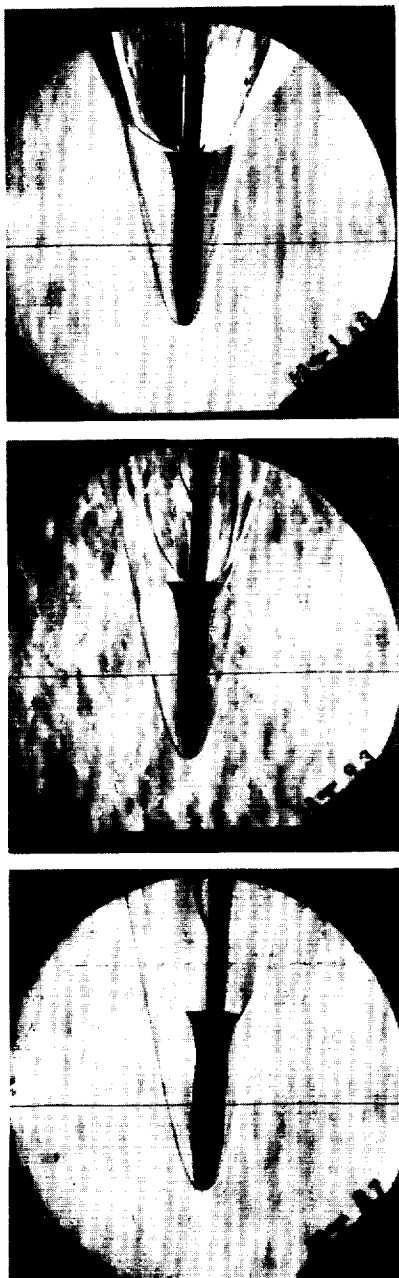
$P_j/P_\infty = 975$



$P_j/P_\infty = 1312$

(c) Schlieren photographs. $\alpha_m = 1.50^\circ$.

Figure 16.- Continued. L-62-80



$p_j/p_\infty = 1312$

$p_j/p_\infty = 100$

Jet off

(a) Schlieren photographs. $\alpha_m = 2.50^\circ$.



$p_j/p_\infty = 560$

$p_j/p_\infty = 975$

(e) Schlieren photographs. $\alpha_m = 3.50^\circ$.

Figure 16.- Concluded. L-62-81

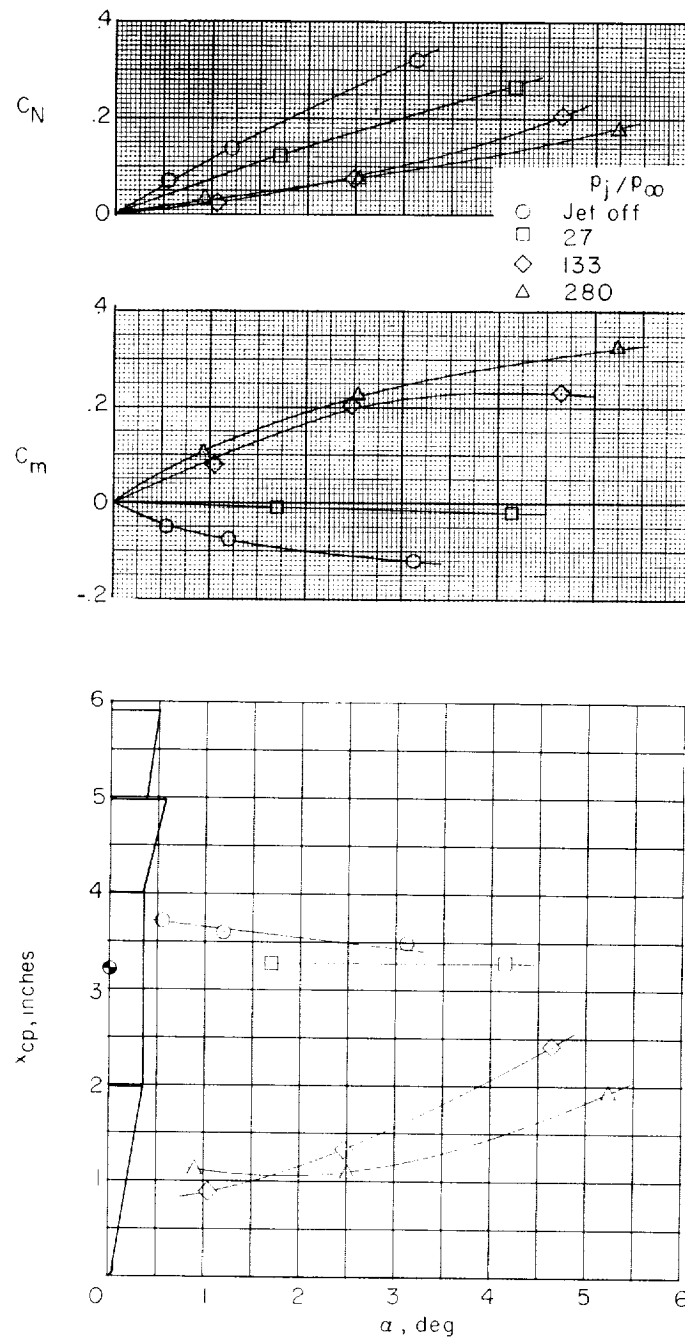
(a) C_N , C_m , and x_{cp} .

Figure 17.- The variation of C_N , C_m , and x_{cp} with angle of attack and pressure ratio for model $C_1BF_{13}N_2$ including schlieren photographs.

L-2039



Jet off

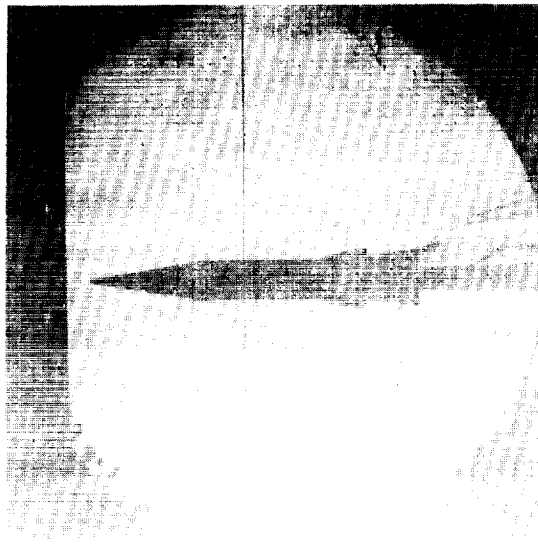
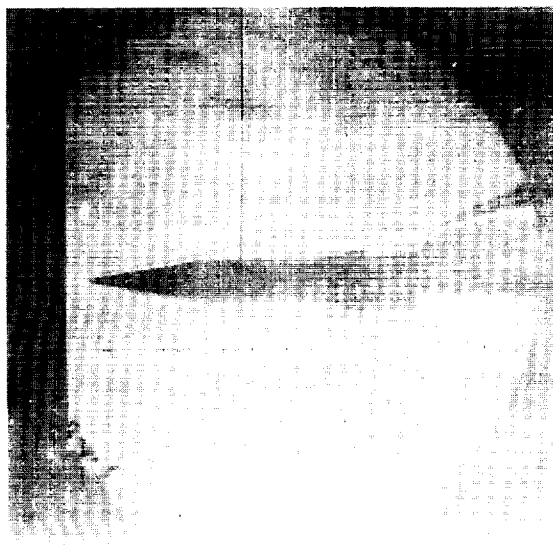
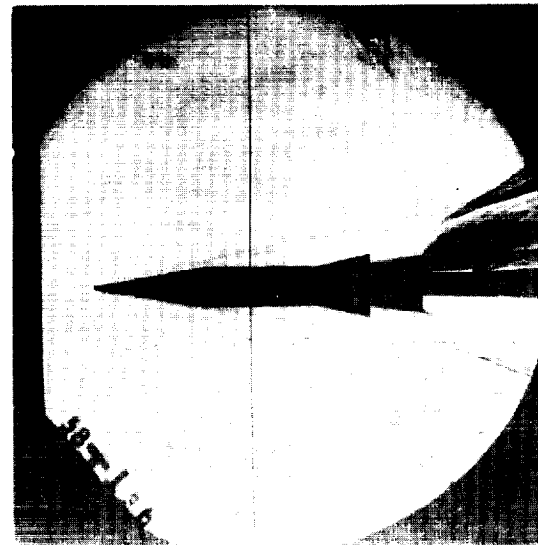
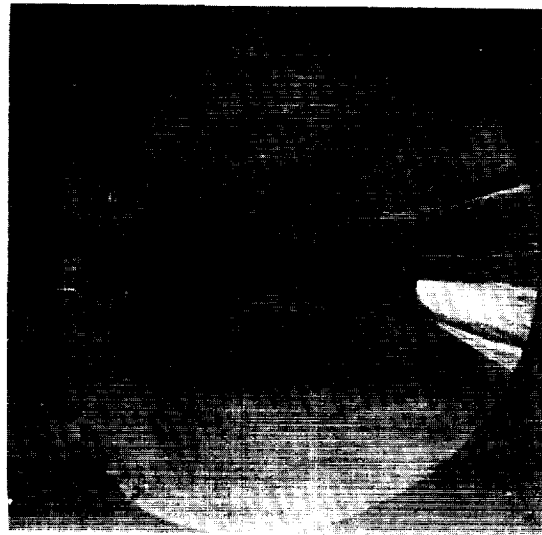
 $P_j/P_\infty = 27$  $P_j/P_\infty = 133$  $P_j/P_\infty = 266$ (b) Schlieren photographs. $\alpha_m = 0^\circ$.

Figure 17.- Continued. L-62-82



Jet off

 $p_j/p_{\infty} = 2.7$  $p_j/p_{\infty} = 13.3$

(c) Schlieren photographs. $\alpha_m = 1.50^\circ$.

Figure 17.- Concluded. L-62-83

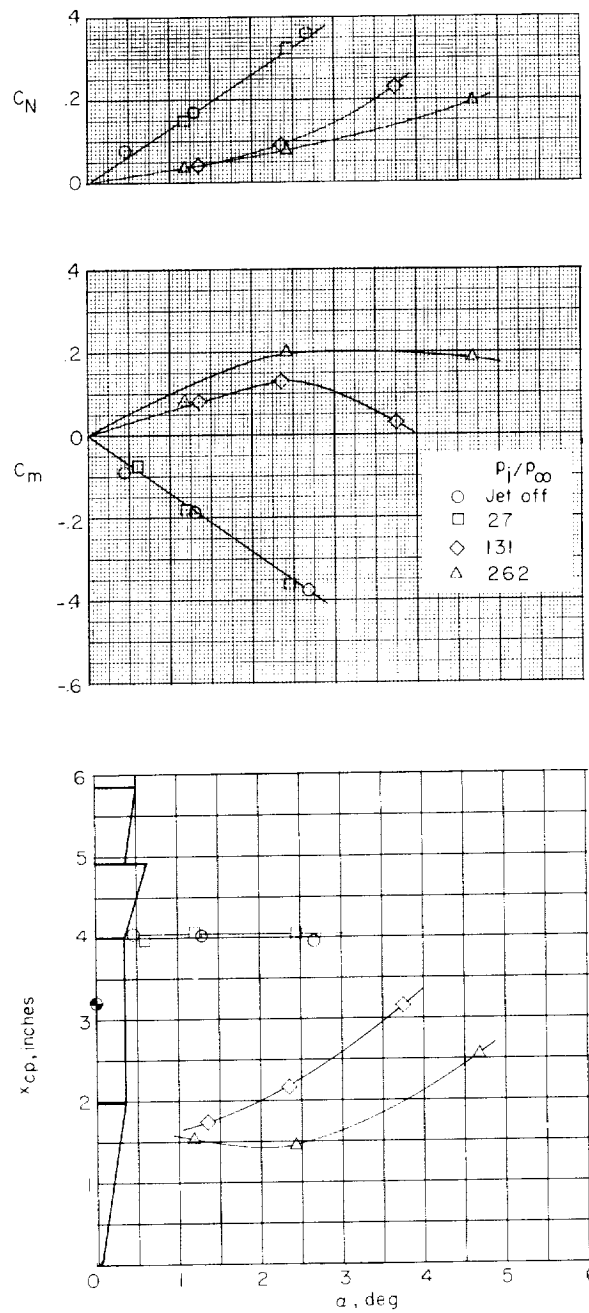
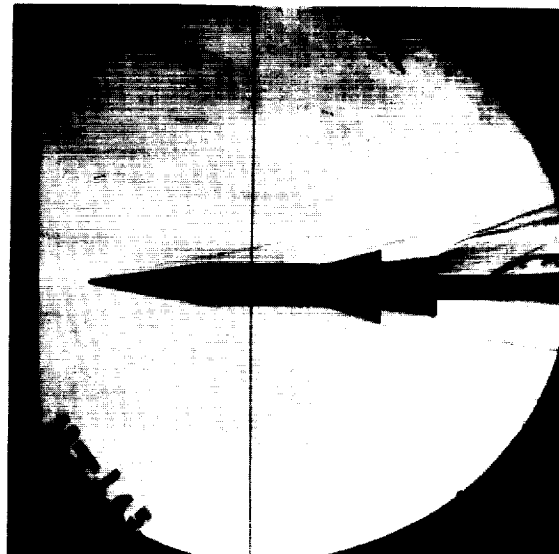
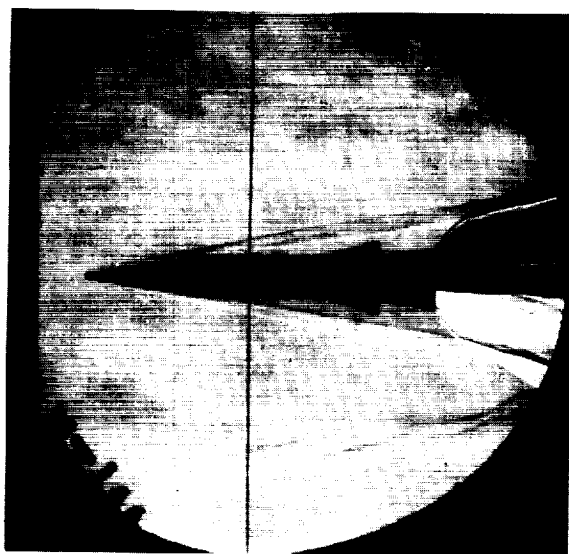
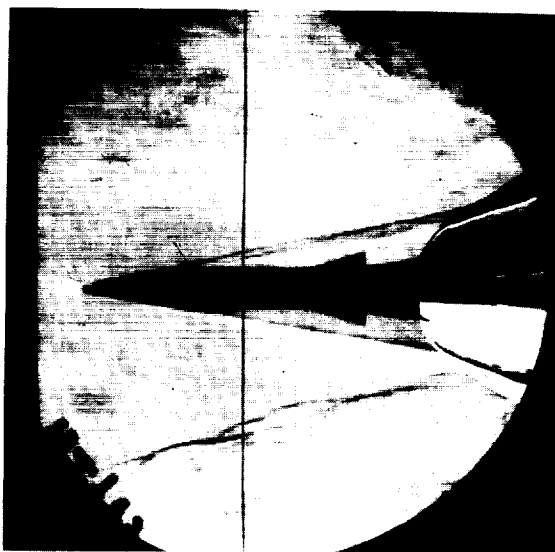
(a) C_N , C_m , and x_{cp} .

Figure 18.- The variation of C_N , C_m , and x_{cp} with angle of attack and pressure ratio for model $C_1BF_{16}N_2$ including schlieren photographs.



Jet off

 $P_j/P_{\infty} = 27$  $P_j/P_{\infty} = 131$  $P_j/P_{\infty} = 262$

(b) Schlieren photographs. $\alpha_m = 0^\circ$.

Figure 18.- Continued. L-62-84

L-2039



Jet off

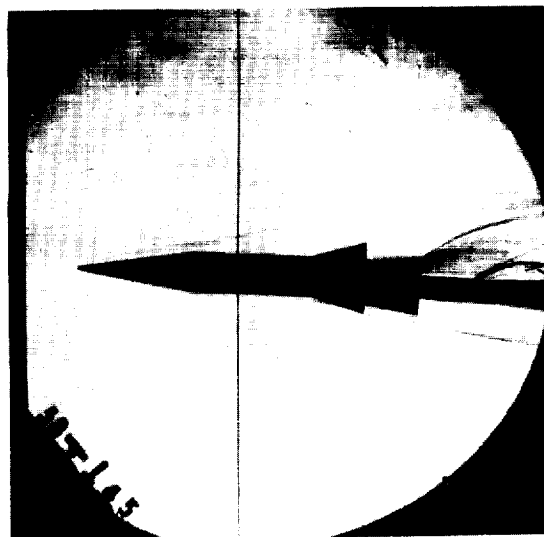
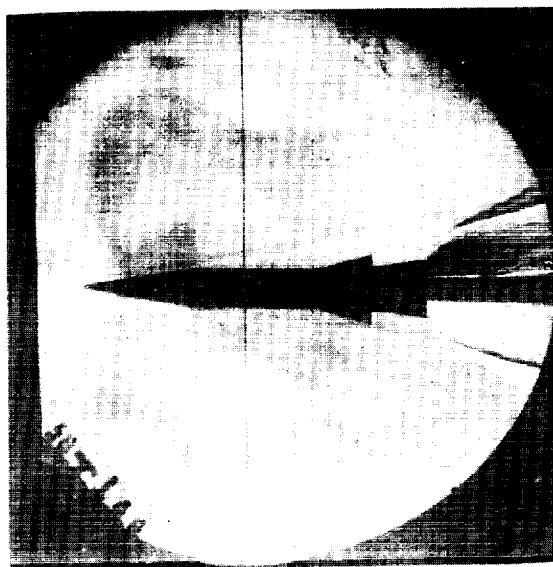
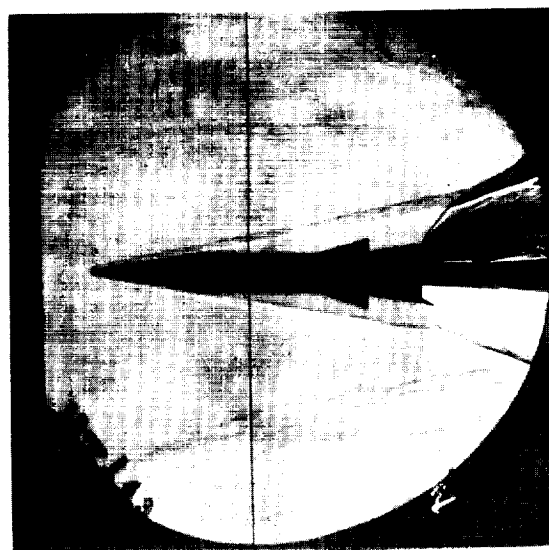
 $P_j/P_\infty = 27$  $P_j/P_\infty = 131$  $P_j/P_\infty = 262$ (c) Schlieren photographs. $\alpha_m = 2.00^\circ$.

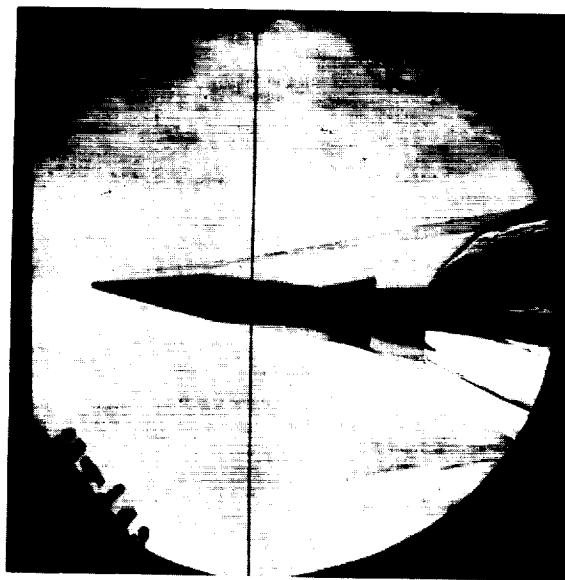
Figure 18.- Continued.

L-62-85



$$p_j / p_\infty = 131$$

(d) Schlieren photograph. $\alpha_m = 3.75^\circ$.



$$p_j / p_\infty = 262$$

(e) Schlieren photograph. $\alpha_m = 4.75^\circ$.

Figure 18.- Concluded. L-62-86

L-2039

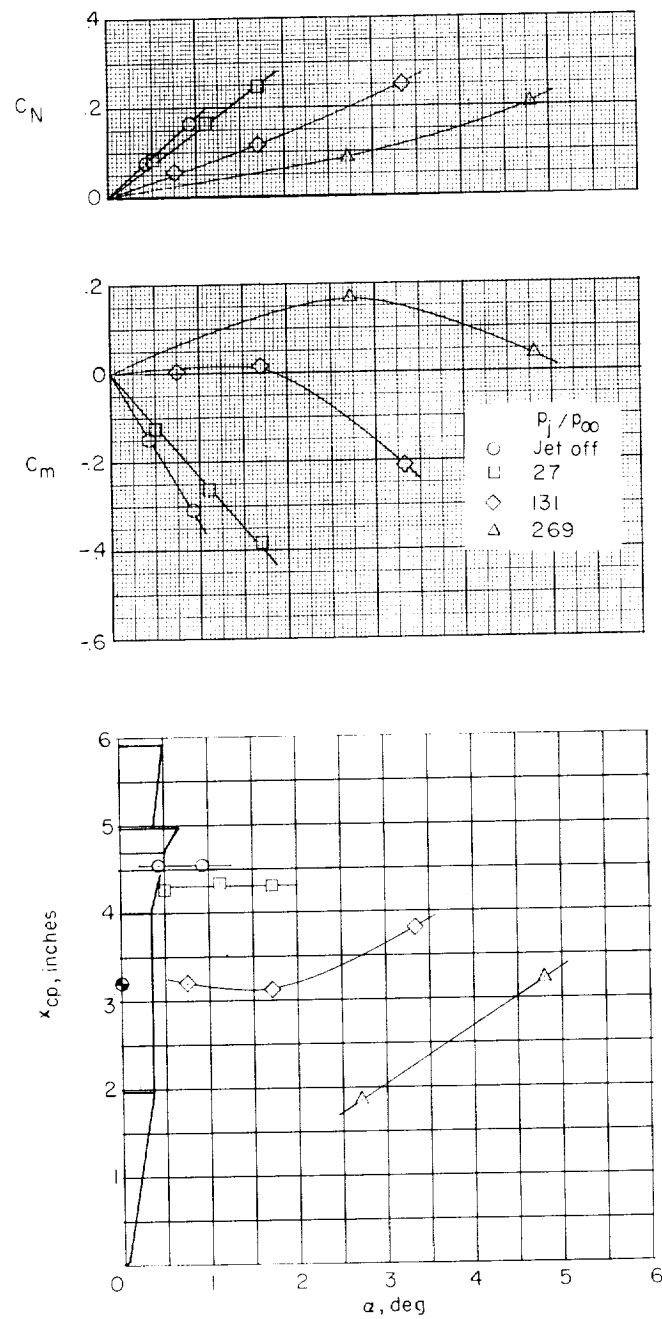
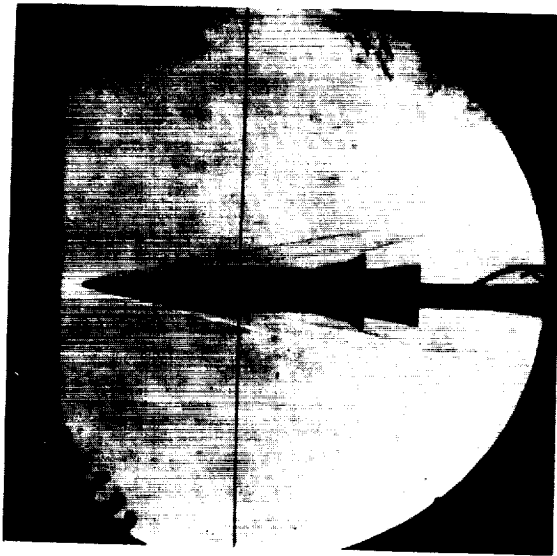
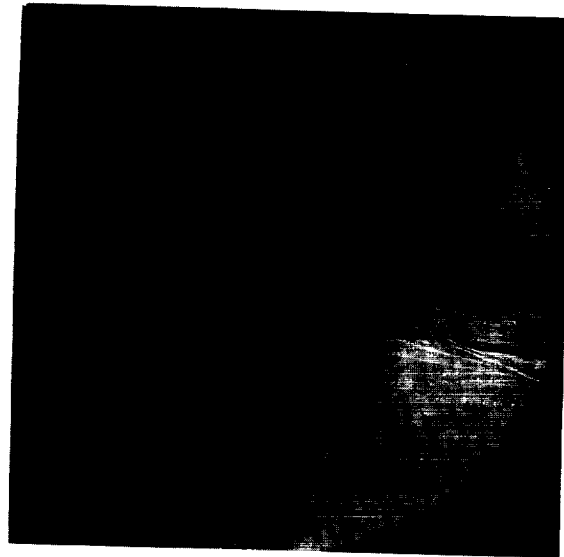
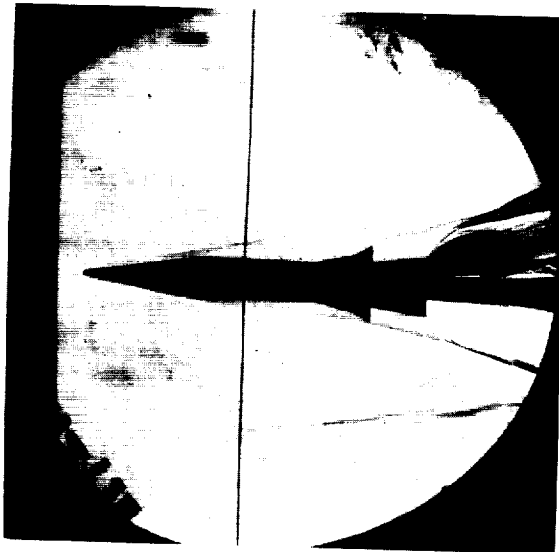
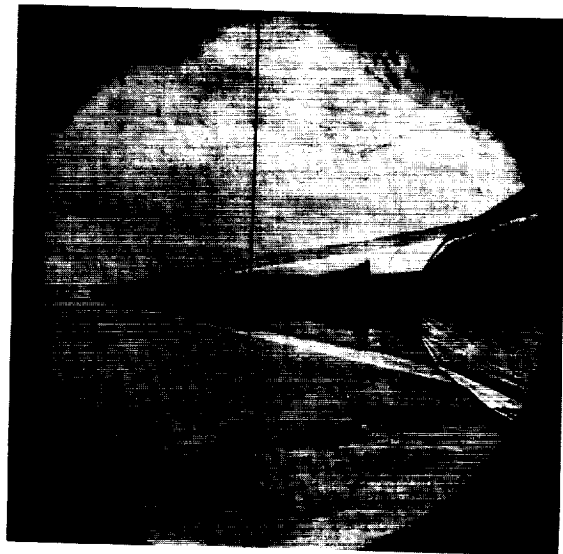
(a) C_N , C_m , and x_{cp} .

Figure 19.- The variation of C_N , C_m , and x_{cp} with angle of attack and pressure ratio for model $C_{1BF13-31N2}$ including schlieren photographs.



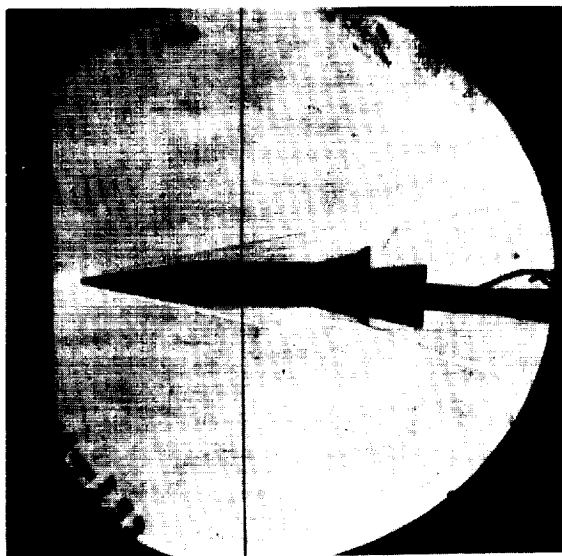
Jet off

 $p_j/p_\infty = 27$  $p_j/p_\infty = 131$  $p_j/p_\infty = 269$

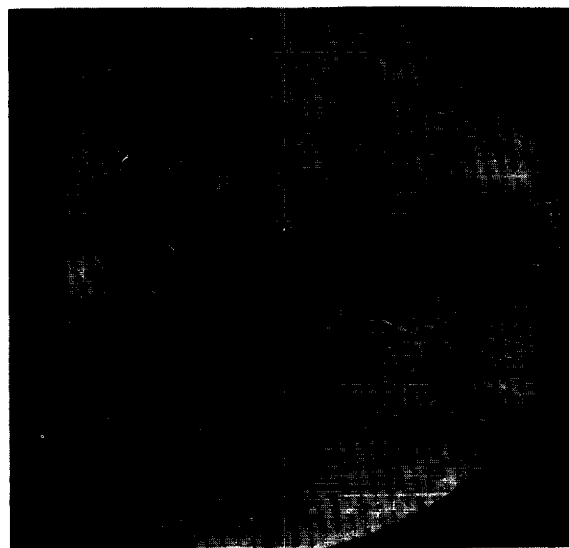
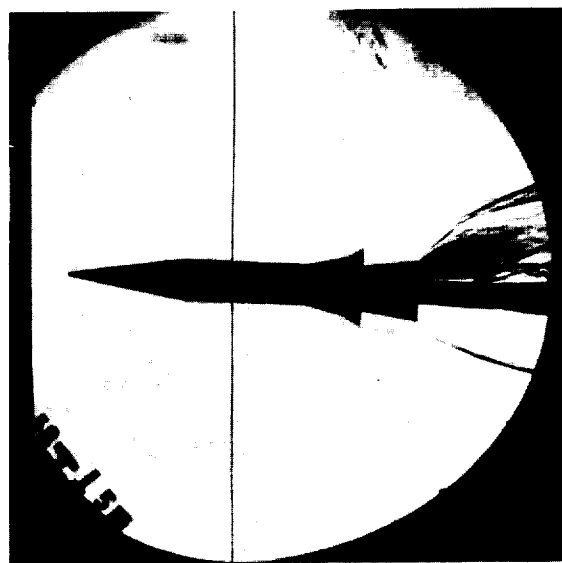
(b) Schlieren photographs. $\alpha_m = 0^\circ$

Figure 19.- Continued. L-62-87

L-2039

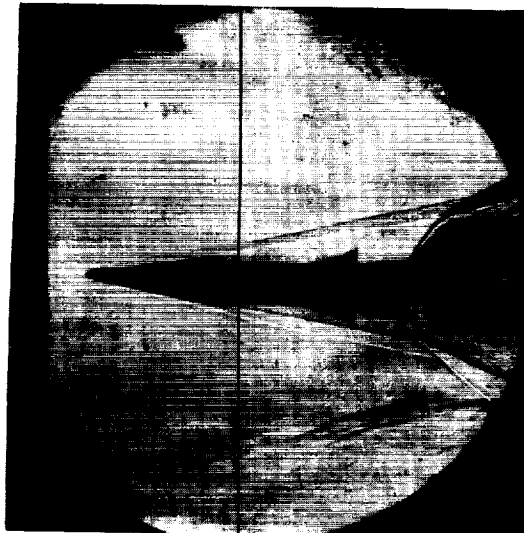


Jet off

 $p_j/p_\infty = 27$  $p_j/p_\infty = 131$

(c) Schlieren photographs. $\alpha_m = 1.00^\circ$.

Figure 19.- Continued. L-62-88



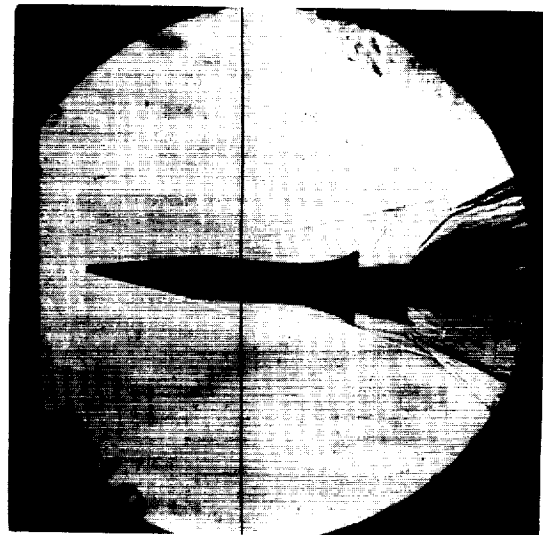
$$p_j/p_\infty = 269$$

(d) Schlieren photograph. $\alpha_m = 2.20^\circ$.



$$p_j/p_\infty = 131$$

(e) Schlieren photograph.
 $\alpha_m = 3.50^\circ$.



$$p_j/p_\infty = 269$$

(f) Schlieren photograph.
 $\alpha_m = 4.80^\circ$.

L-2039

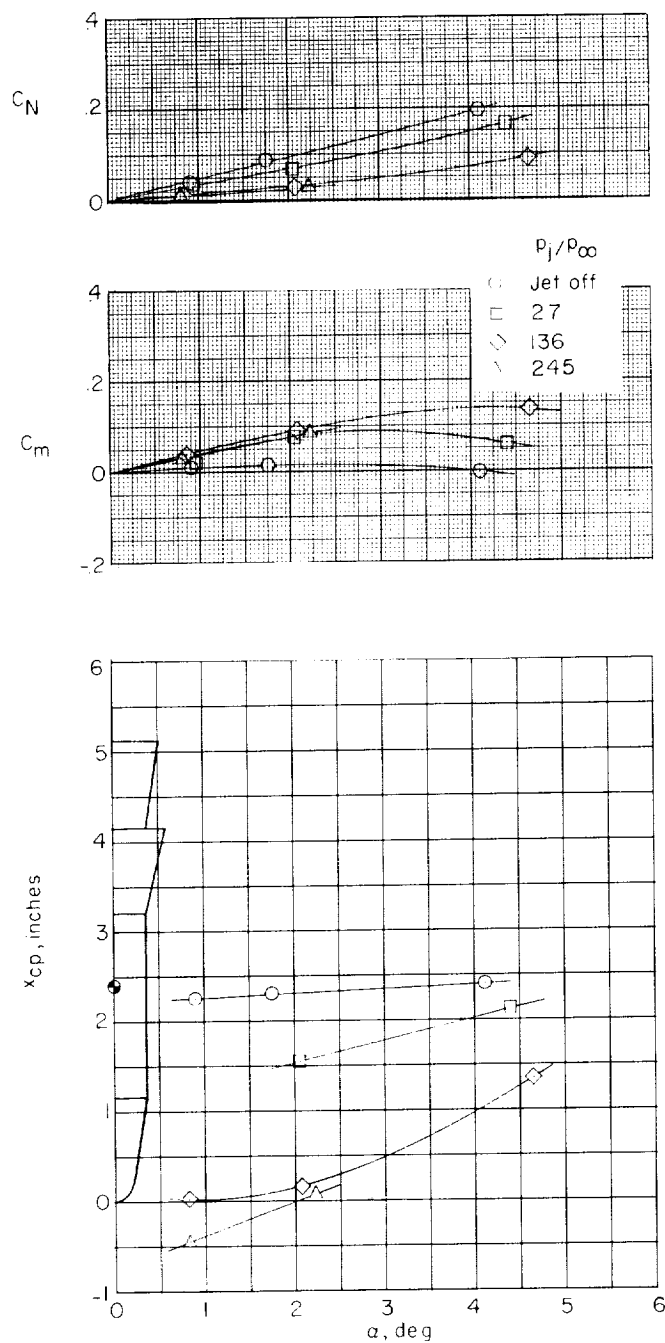
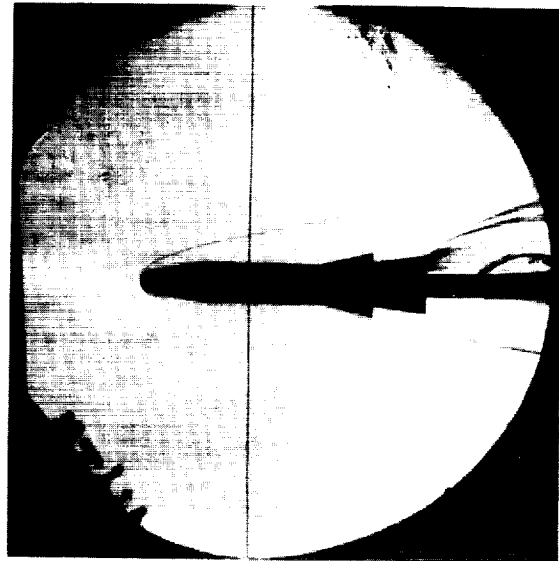
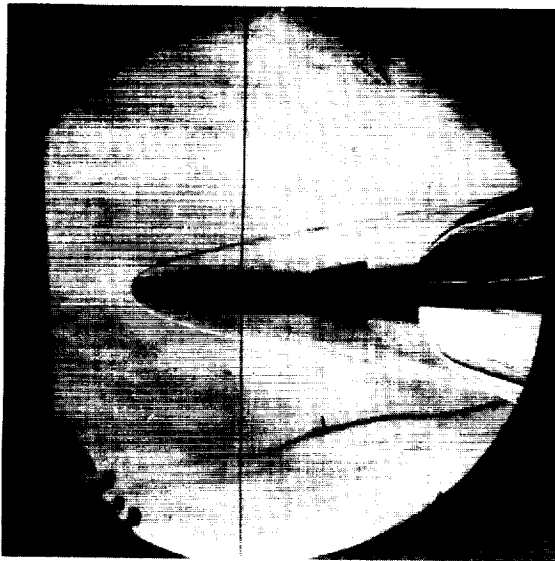
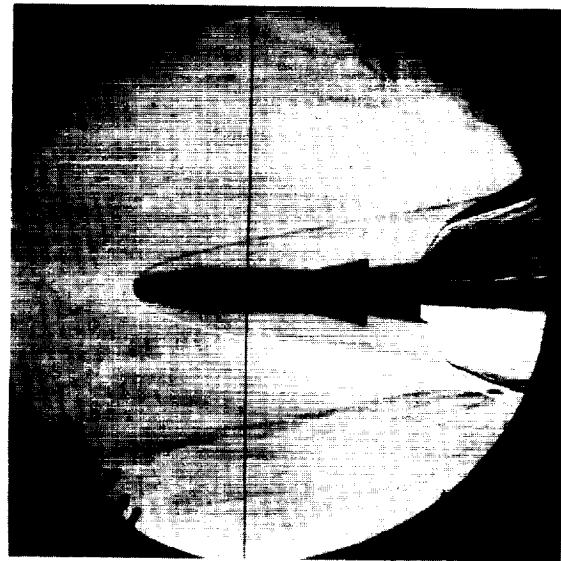
(a) C_N , C_m , and x_{cp} .

Figure 20.- The variation of C_N , C_m , and x_{cp} with angle of attack and pressure ratio for model $C_2BF_{13}N_2$ including schlieren photographs.



Jet off

 $p_j/p_\infty = 27$  $p_j/p_\infty = 136$  $p_j/p_\infty = 245$

(b) Schlieren photographs. $\alpha_m = 0^\circ$.

Figure 20.- Continued. L-62-90

L-2039



Jet off

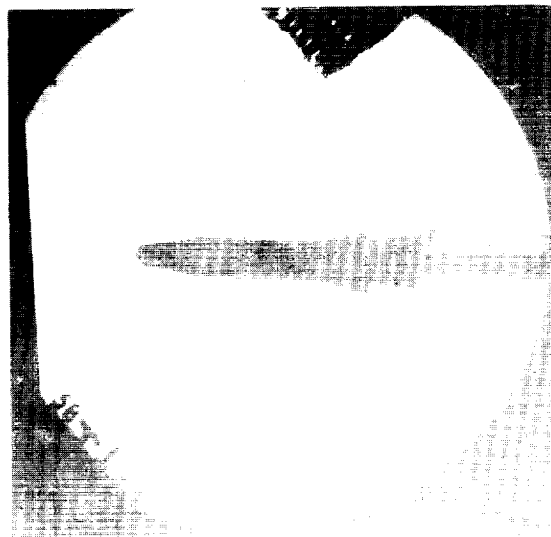
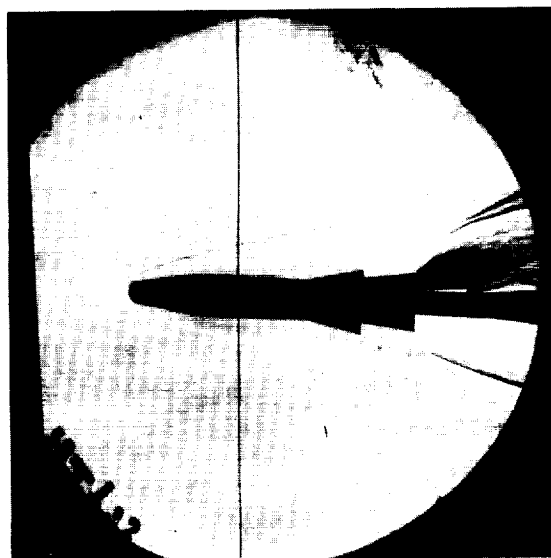
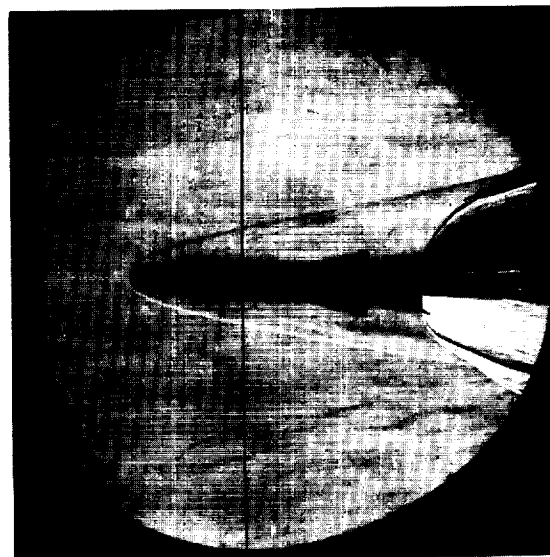
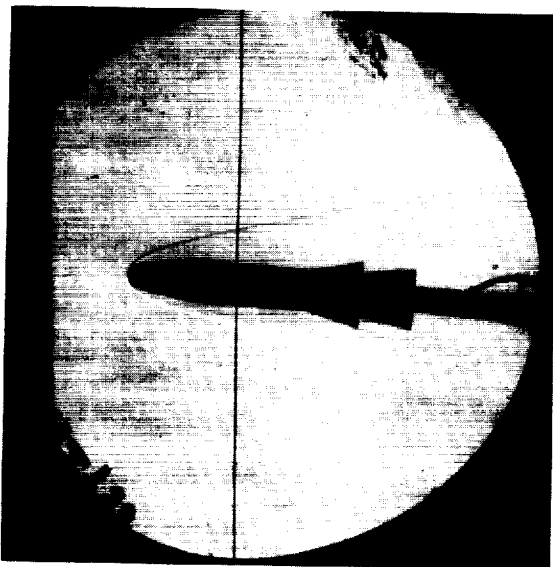
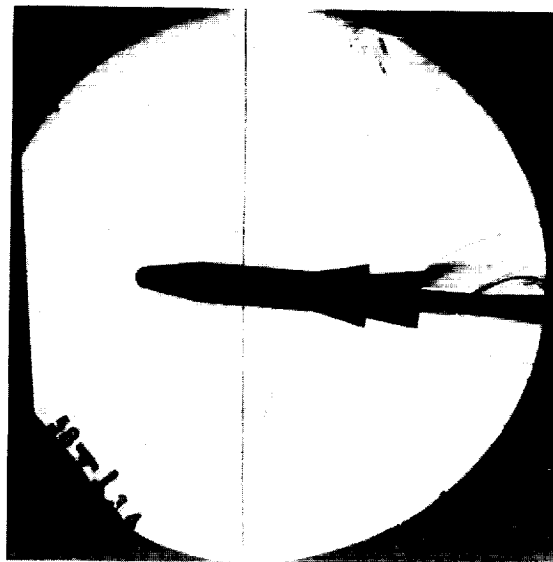
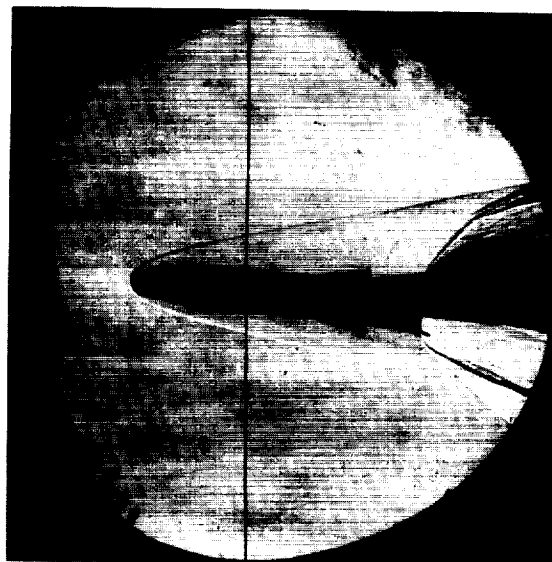
 $p_j/p_\infty = 27$  $p_j/p_\infty = 136$  $p_j/p_\infty = 245$ (c) Schlieren photographs. $\alpha_m = 2.00^\circ$.

Figure 20.- Continued.

L-62-91



Jet off

 $P_j/P_\infty = 27$  $P_j/P_\infty = 136$  $P_j/P_\infty = 245$

(d) Schlieren photographs. $\alpha_m = 4.25^\circ$.

Figure 20.- Concluded. L-62-92

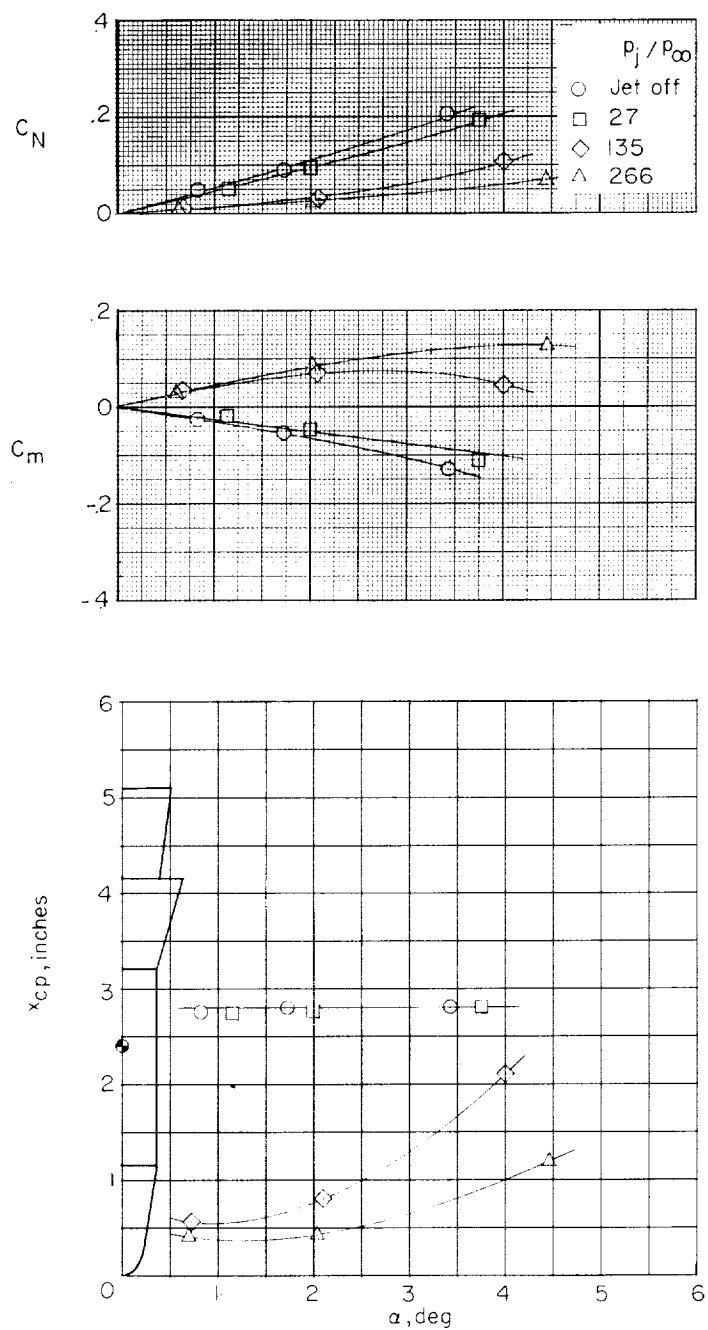
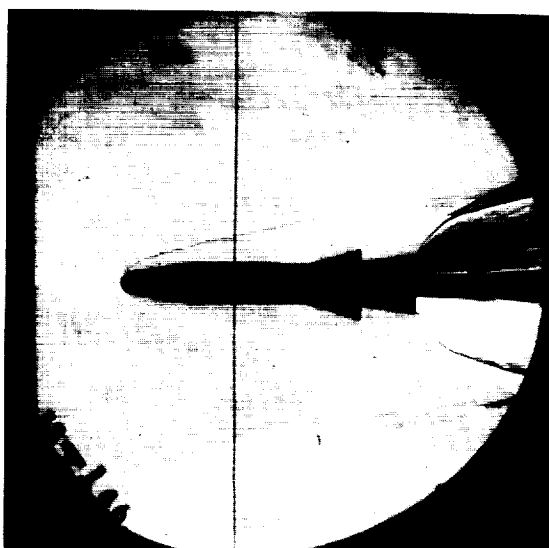
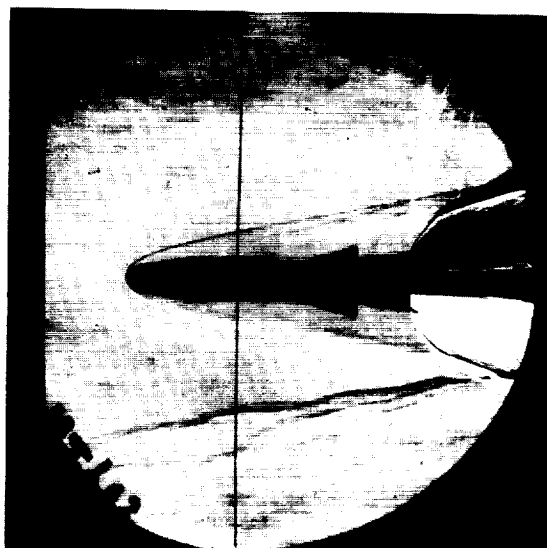
(a) C_N , C_m , and x_{cp} .

Figure 21.- The variation of C_N , C_m , and x_{cp} with angle of attack and pressure ratio for model $C_2BF_{16}N_2$ including schlieren photographs.



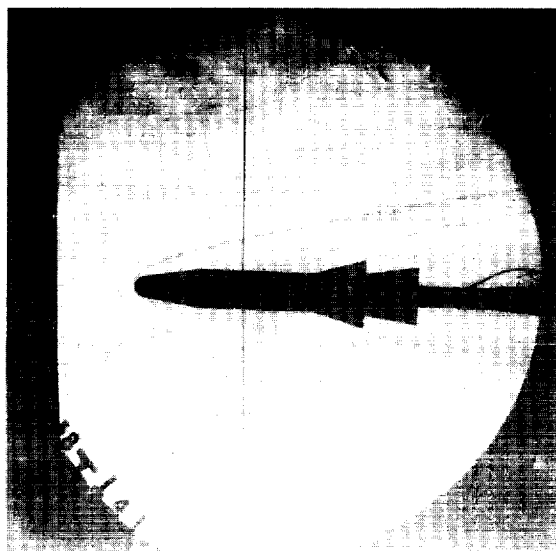
Jet off

 $P_j/P_\infty = 27$  $P_j/P_\infty = 133$  $P_j/P_\infty = 266$

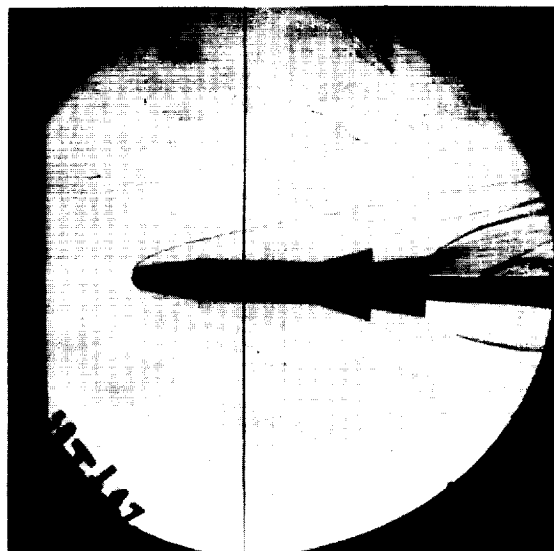
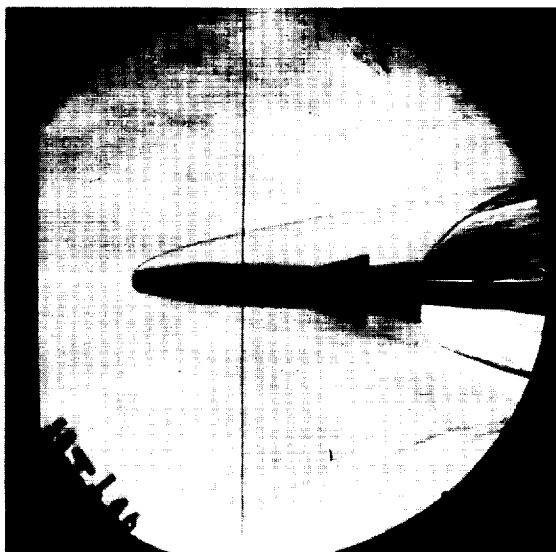
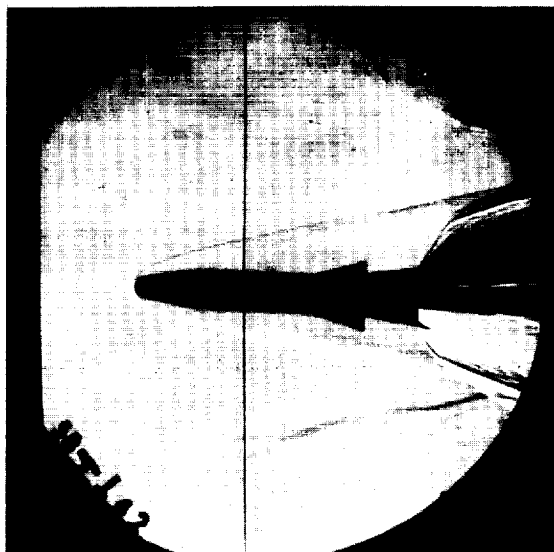
(b) Schlieren photographs. $\alpha_m = 0^\circ$.

Figure 21.- Continued. L-62-93

L-2039



Jet off

 $P_j/P_\infty = 27$  $P_j/P_\infty = 133$  $P_j/P_\infty = 266$

(c) Schlieren photographs. $\alpha_m = 2.00^\circ$.

Figure 21.- Continued. L-62-94



Jet off

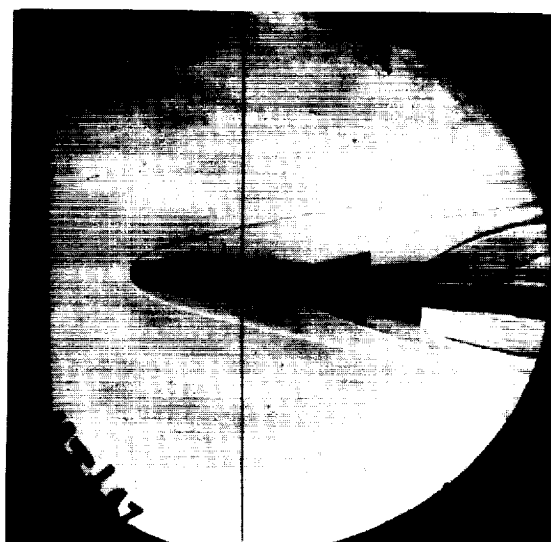
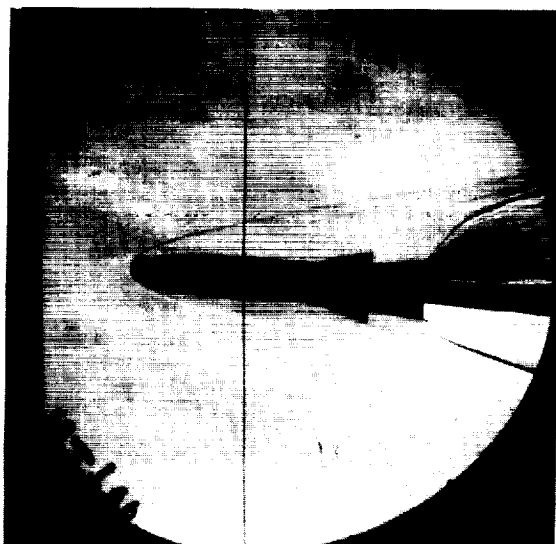
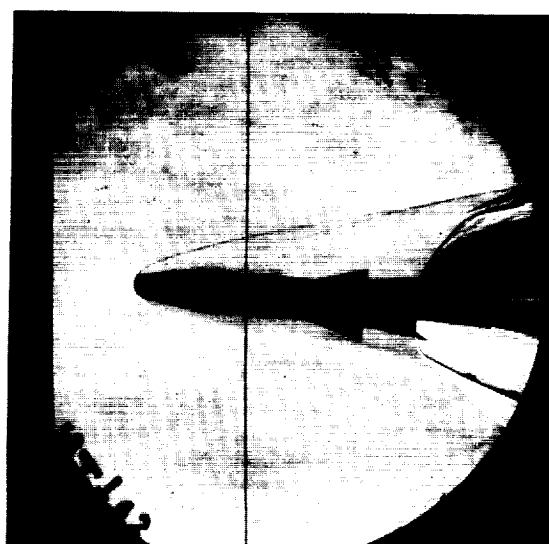
 $p_j/p_\infty = 27$ (d) Schlieren photographs. $\alpha_m = 3.50^\circ$. $p_j/p_\infty = 133$  $p_j/p_\infty = 266$ (e) Schlieren photographs. $\alpha_m = 4.25^\circ$.

Figure 21.- Concluded.

L-62-95

L-2039

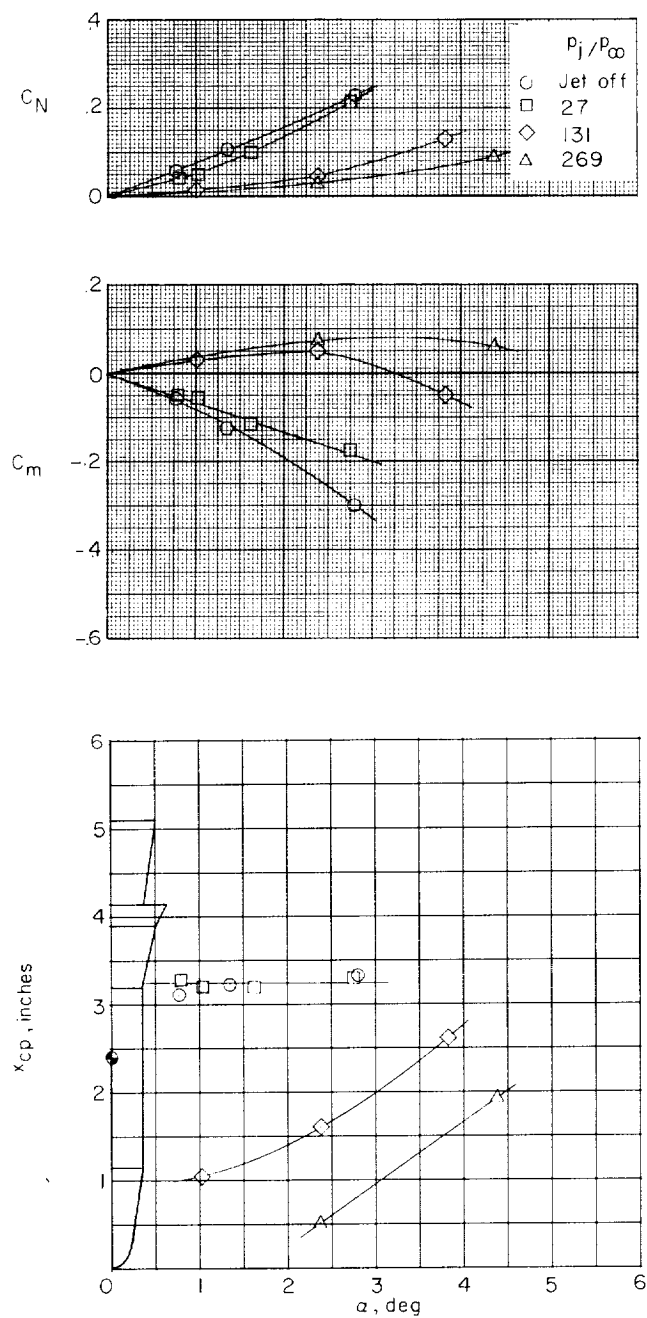
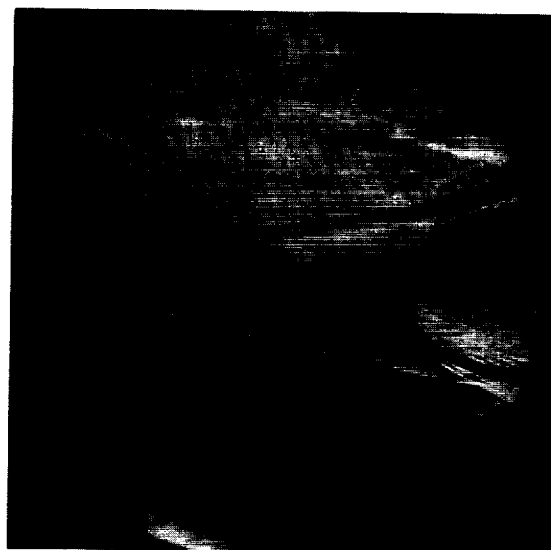
(a) C_N , C_m , and x_{cp} .

Figure 22.- The variation of C_N , C_m , and x_{cp} with angle of attack and pressure ratio for model $C_2BF_{13-31}N_2$ including schlieren photographs.



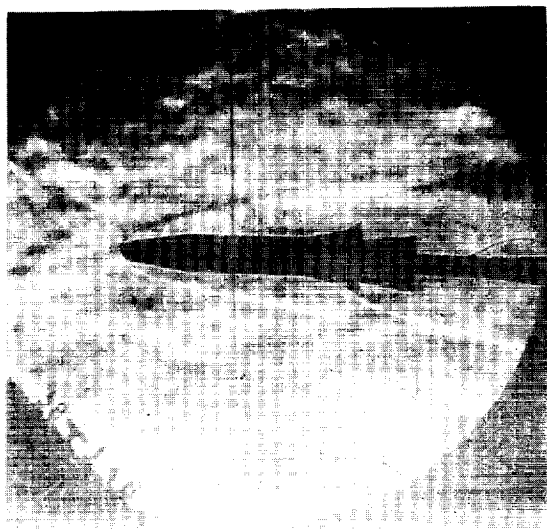
Jet off

 $P_j/P_\infty = 27$  $P_j/P_\infty = 135$  $P_j/P_\infty = 269$

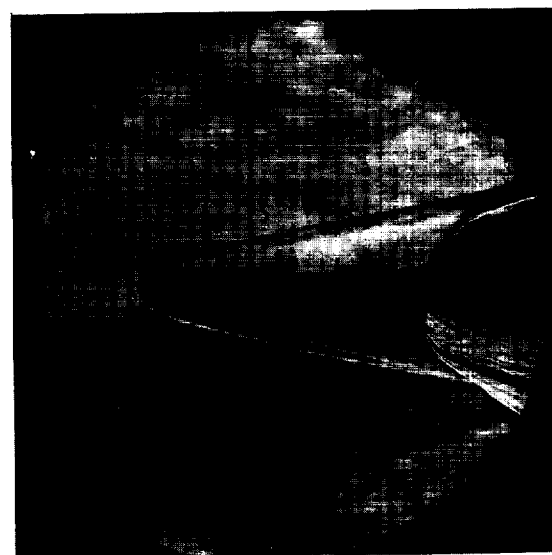
(b) Schlieren photographs. $\alpha_m = 0^\circ$.

Figure 22.- Continued. L-62-96

L-2039



Jet off

 $P_j/P_\infty = 27$  $P_j/P_\infty = 135$  $P_j/P_\infty = 269$

(c) Schlieren photographs. $\alpha_m = 2.50^\circ$.

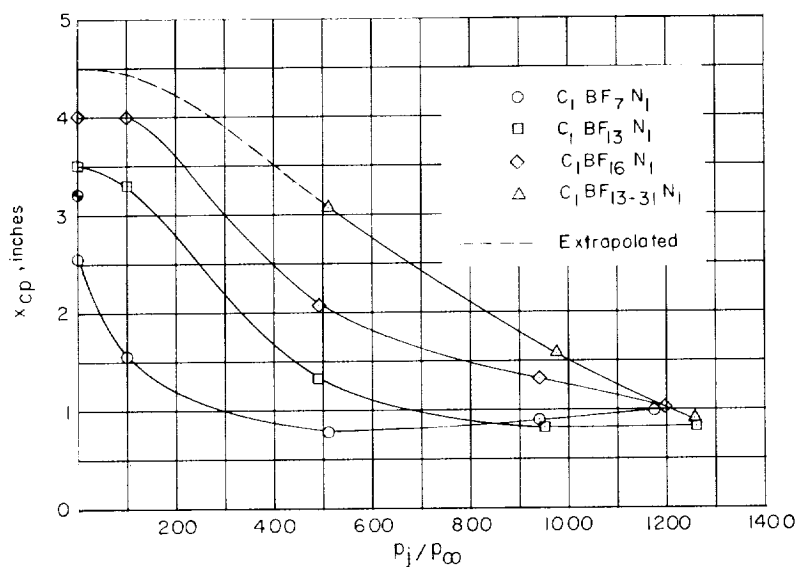
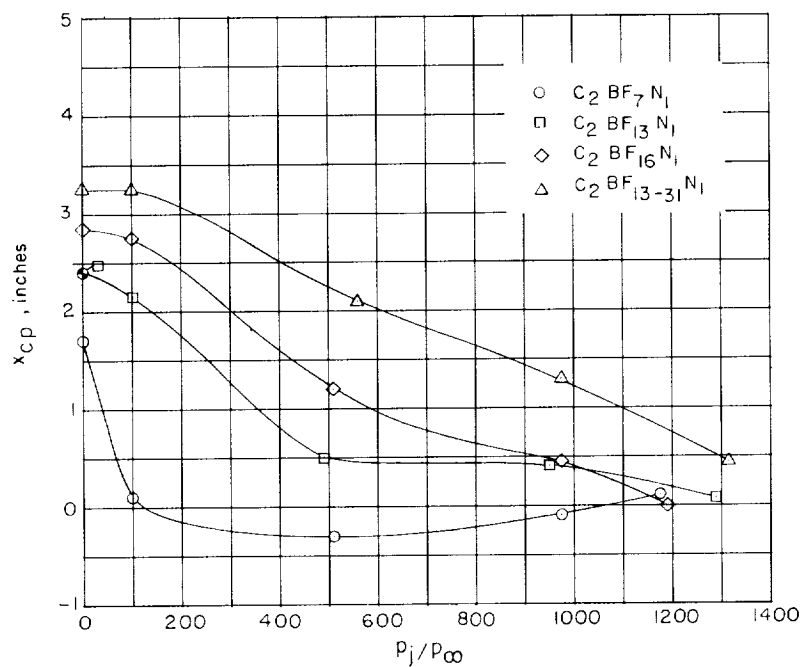
Figure 22.- Continued.

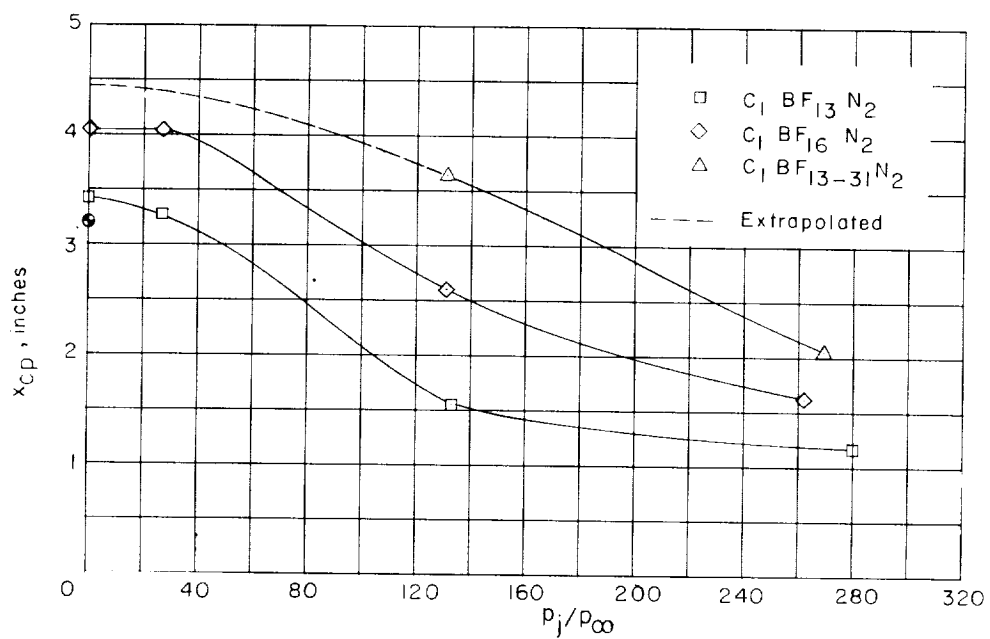
L-62-97

 $p_j/p_\infty = 135$  $p_j/p_\infty = 269$

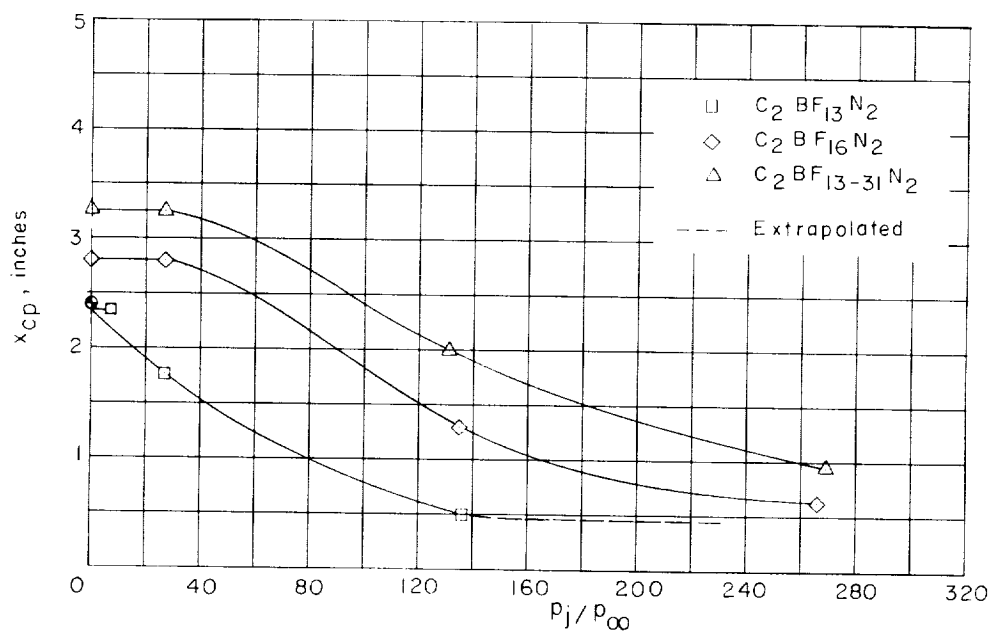
(d) Schlieren photographs. $\alpha_m = 4.00^\circ$.

Figure 22.- Concluded. L-62-98

(a) $r/R = 0.094$; nozzle N_1 .(b) $r/R = 0.569$; nozzle N_1 .Figure 23.- Effect of flare geometry on the variation of x_{cp} with jet-pressure ratio at $\alpha = 3^\circ$.



(c) $r/R = 0.094$; nozzle N_2 .



(d) $r/R = 0.569$; nozzle N_2 .

Figure 23.- Concluded.

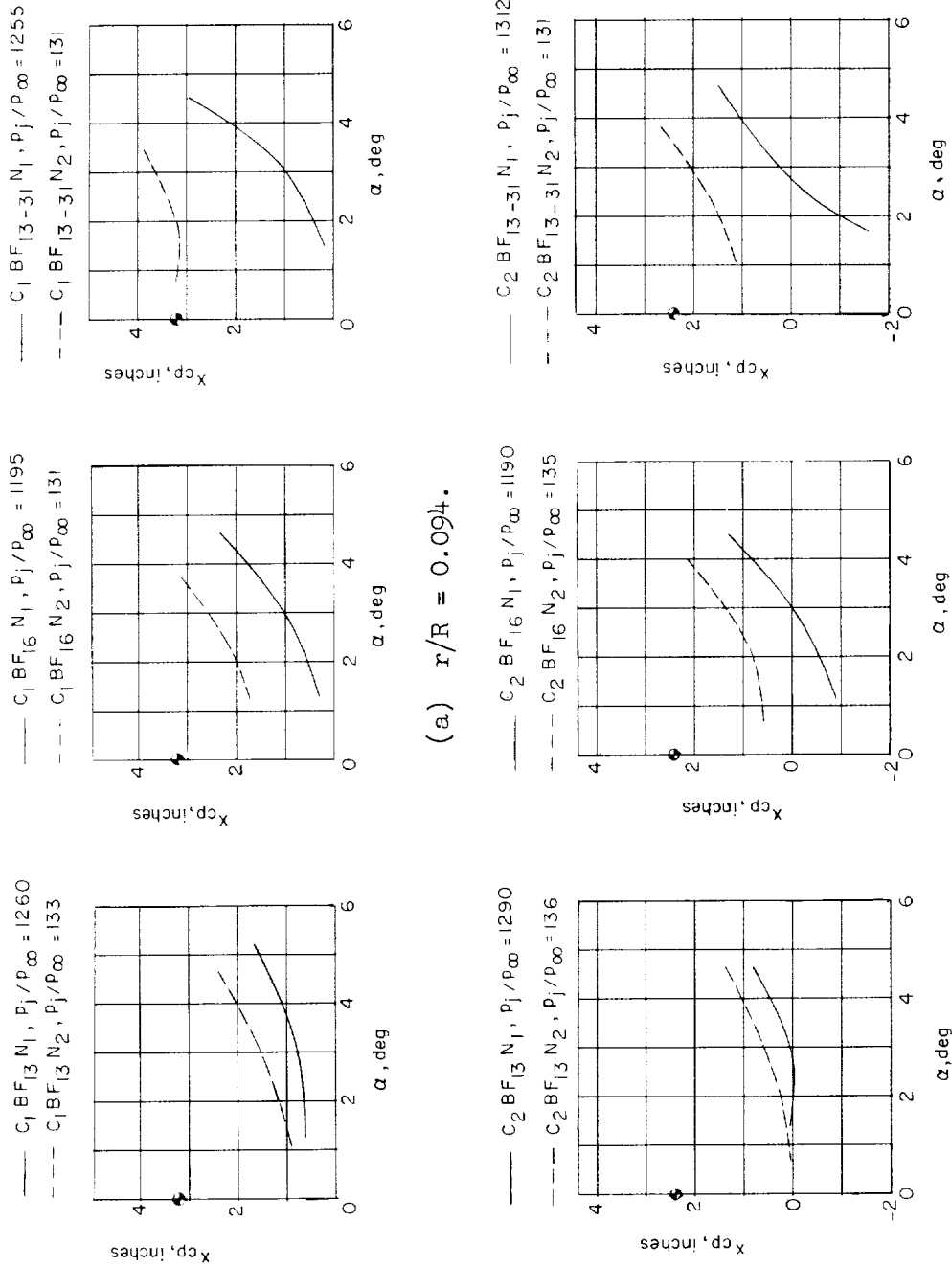


Figure 24.- Effect of jet nozzle geometry and exit location on the center-of-pressure location at a given altitude and chamber pressure. Nose tip of $x_{cp} = 0$.

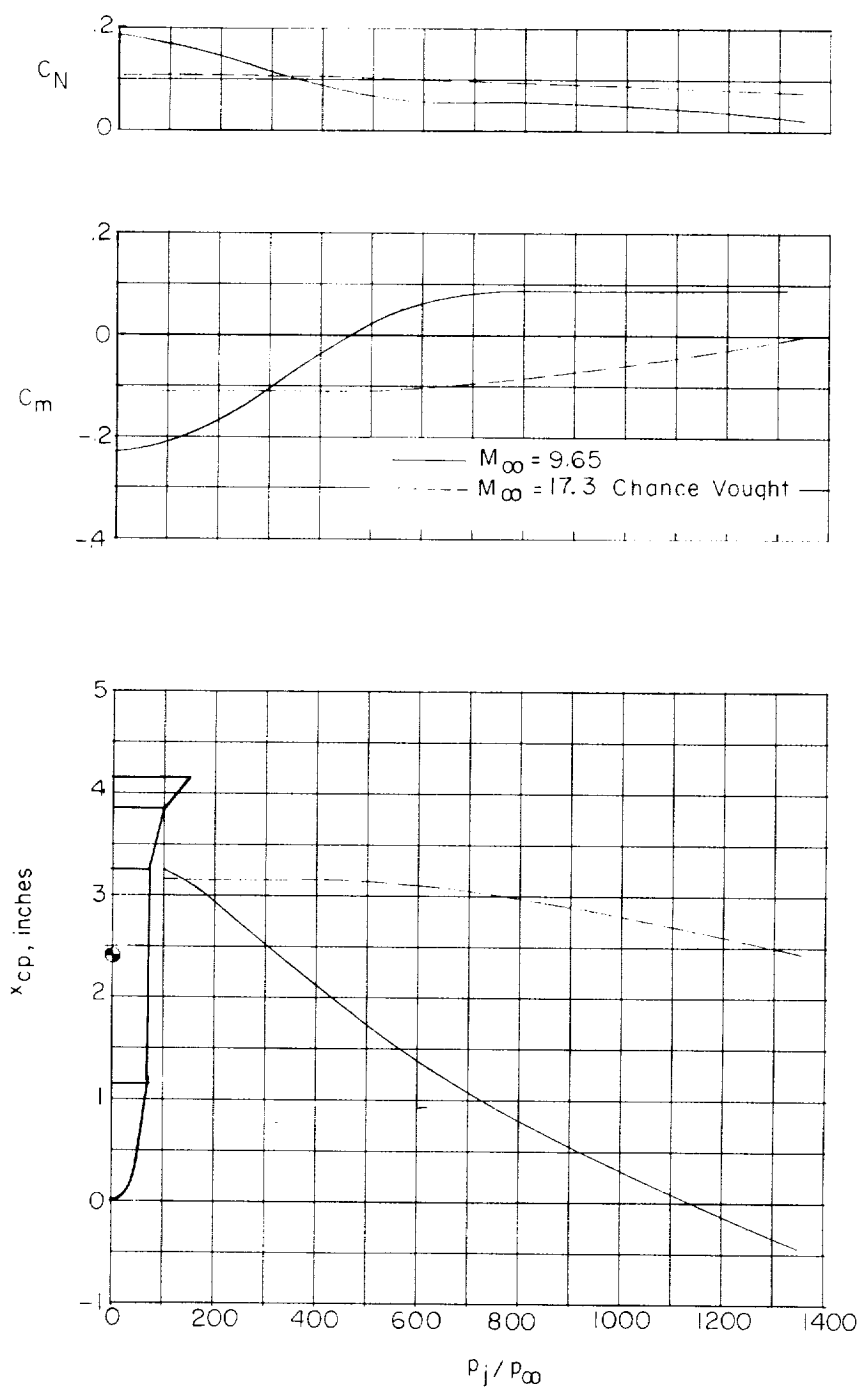


Figure 25.- Effect of free-stream Mach number on the variation of C_N , C_m , and x_{cp} with jet-pressure ratio for model $C_{2BF13-31N1}$ at $\alpha = 2.4^\circ$.

$C_1 \text{BF}_{13-31} \text{N}_1$ $C_2 \text{BF}_{13-31} \text{N}_1$ p_j/p_∞

$$\frac{r}{R} = .094$$

$$\frac{r}{R} = .569$$

---○---

---○--- Jet off

---□---

---□--- 100

---△---

---△--- 975

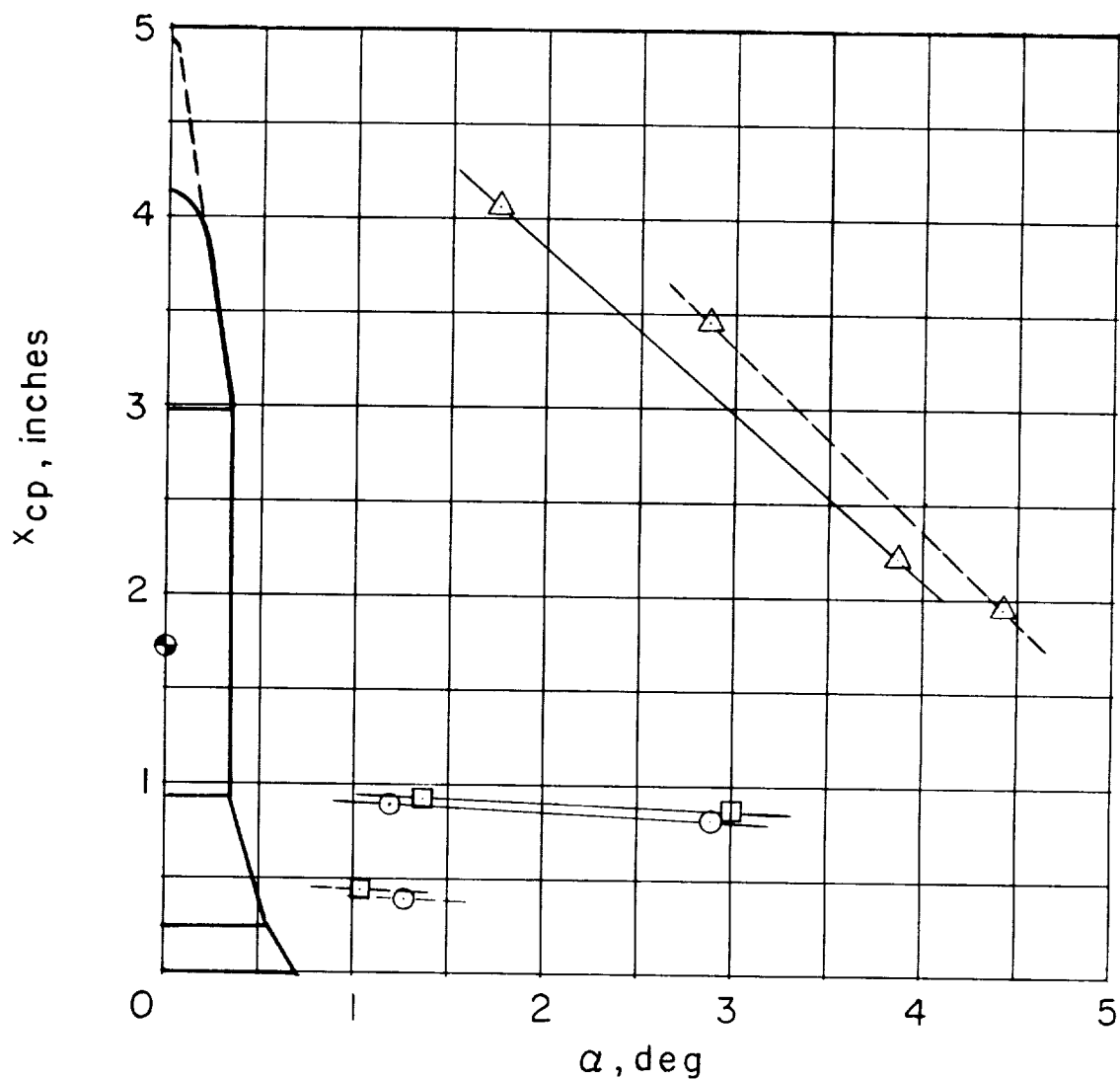


Figure 26.- Typical comparison of the effect of nose bluntness on center-of-pressure location for various pressure ratios.

